UNIVERSITY OF SOUTHAMPTON
FACULTY OF ENGINEERING, SCIENCE AND MATHEMATICS
Optoelectronics Research Centre

Passive and active Bragg gratings for optical networks

by
Zhaowei Zhang

Thesis submitted for the degree of Doctor of Philosophy
January 2007

UNIVERSITY OF SOUTHAMPTON

ABSTRACT

FACULTY OF ENGINEERING, SCIENCE AND MATHEMATICS

OPTOELECTRONICS RESEARCH CENTRE

Doctor of Philosophy

PASSIVE AND ACTIVE BRAGG GRATINGS FOR OPTICAL NETWORKS

by Zhaowei Zhang

This thesis investigates fibre Bragg grating (FBG) devices. Specifically, it consists of the developments and applications of two groups of devices: the optical phase en/decoders and the tunable fibre Bragg gratings based on an S-bending technique.

Three types of FBGs based optical phase en/decoders, including conventional discrete-phase en/decoders, new reconfigurable-phase en/decoders, continuous-phase en/decoders, and their applications in optical code division multiple access (OCDMA) systems are studied in this thesis. A reconfigurable-phase en/decoder is composed of a uniform FBG and a series of equidistant tungsten wires in contact with it. The spatial phases along the FBG are configured by controlling the electrical currents through the tungsten wires. Its reconfiguration time is demonstrated to be less than two seconds. In order to obtain the full information about a reconfigurable-phase en/decoder, the pulse response method is introduced to accurately characterize the thermally induced dc refractive index variation in an FBG. In addition, a new continuous-phase en/decoder is developed. It has a spatial phase profile matching the reconfigurable-phase device accurately, and therefore, it has the inherent advantage to operate together with reconfigurable-phase devices in a reconfigurable OCDMA system.

The advantage of an S-bending tuning FBG is that its central wavelength is invariant as the linear strain gradient along the FBG is altered. Two new devices are developed by embedding a pair of FBGs in a single uniform beam for S-bending. One is the tunable dispersion compensator with a wide tuning range, and the other is a tunable pure dispersion slope compensator. The application of an S-bending tuning FBG in controlling the output pulse width of a soliton fibre laser is also experimentally demonstrated.

Contents

List of Figures

List of Tables

Declaration of Authorship

I, Zhaowei Zhang,
declare that the thesis entitled "Passive and active Bragg gratings for optical networks" and the work presented in the thesis are both my own, and have been generated by me as the result of my own original research. I confirm that:

- this work was done wholly or mainly while in candidature for a research degree at this University;

- where any part of this thesis has previously been submitted for a degree or any other qualification at this University or any other institution, this has been clearly stated;

- where I have consulted the published work of others, this is always clearly attributed;

- where I have quoted from the work of others, the source is always given. With the exception of such quotations, this thesis is entirely my own work;

- I have acknowledged all main sources of help;

- where the thesis is based on work done by myself jointly with others, I have made clear exactly what was done by others and what I have contributed myself;

- I have published as part of Ph.D. work some of the research material contained within this thesis as journal and conference papers (see List of Publications).

Signed: ……..
Date:…….

Author's Contributions

Most of the experimental work was carried out in collaboration with other colleagues in the ORC, although the author has played the key role for the work reported in this thesis.

For all the experiments using the frequency-resolved optical-gating (FROG) technique, the FROG setup and pulse retrieval algorithm were provided by Dr. Michaël A. F. Roelens, the measurements were performed by Mr. Chun Tian and the author together, and the pulse retrieval was performed by Mr. Chun Tian and Dr. Michaël A. F. Roelens.

For all the experiments on OCDMA systems, the setups were prepared by Mr. Chun Tian, and the experiments were performed by Mr. Chun Tian and the author together.

The soliton laser used in Section.7.6 was provided by Dr. John Clowes from Fianium Ltd.

All the fibre Bragg gratings used in the experiments were fabricated by Dr. Morten Ibsen.

Acknowledgements

I would like to thank my supervisor, Dr Morten Ibsen, for accepting me as his PhD student and his excellent guidance throughout the three years. His advice, support, and encouragement have always been invaluable for my study. I would also express my gratitude to Prof. David. J. Richardson for his generous support and many critical suggestions. I would like to thank my colleagues Mr. Chun Tian, Dr. Mohd R. Mokhtar, Dr. Michaël A. F. Roelens, Dr. Periklis Petropoulos, Miss Nyuk Yoong Voo, Mr. Albert Canagasabey, and Mr. Ian Wong for the helpful discussions and collaborations. I would also acknowledge the assistance from Mr. Simon Butler and Mr. Timothy McIntyre. A special thank goes to Dr. Eleanor Tarbox for her support during my PhD and her help during the writing of this thesis. Finally, I would like to thank my wife, who is always accompanying me during my PhD study, my parents and sisters for their care, encouragement, endless love and support.

Nomenclature

A, B	Amplitude of forward/backward propagating mode
c	Light speed in the vacuum
E	Young's modulus
F	Force
k	Propagation constant in the vacuum
M	Moment
n_{eff}	Effective modal index
q	Complex coupling coefficient of the grating
r	Reflection coefficient of the grating
t	Transmission coefficient of the grating
u, v	Envelope of the forward/backward propagating mode
α	Coefficient of thermal expansion
β	Mode propagation constant
β_1	Group delay parameter
β_2	Group delay dispersion parameter
β_3	Third order dispersion (TOD) parameter
γ	Effective propagation constant
σ	'DC' coupling constant, or stress
δ	Frequency detuning parameter
Δn_{ac}	"AC" index perturbation
Δn_{dc}	"DC" index perturbation
Δt	Chip duration
ΔT	Temperature change
$\Delta\lambda_B$	Shift of the Bragg wavelength
ε	Strain
θ	Grating phase describing the grating chirp
κ	'AC' coupling constant
λ	Wavelength

λ_B	Bragg wavelength
Λ	Grating pitch
ρ	Discrete reflection coefficient of the grating
ρ_e	Photo-elastic constant
τ	Time delay
ϕ	Spatial phase of the grating
ω	Angular frequency

Acronyms

AC	Alternating current
ASE	Amplified spontaneous emission
BER	Bit error rate
CDMA	Code division multiple access
CFBG	Chirped fibre Bragg grating
CPA	Chirped pulse amplification
CTE	Coefficient of thermal expansion
CME	Coupled mode equations
DC	Direct current
DCF	Dispersion compensating fibre
DFB	Distributed feedback
DS	Dispersion slope or direct sequence
DS-CDMA	Direct sequence code division multiple access
EAM	Electro-absorption modulator
EOM	Electro-optic modulator
FBG	Fibre Bragg grating
FE-CDMA	Frequency encoding code division multiple access
FH-CDMA	Frequency hopping code division multiple access
FP	Fabry-Pérot
FROG	Frequency-resolved optical-gating
FSR	Free spectral range
FWHM	Full width at half maximum
GVD	Group delay dispersion
HOM-DCF	Higher-order-mode dispersion compensating fibres
LCFBG	Linearly chirped fibre Bragg grating
MZ	Mach-Zehnder
NA	Numerical aperture
NCFBG	Nonlinearly-chirped fibre Bragg grating

OCDMA	Optical code division multiple access
OFDR	Optical frequency-domain reflectometry
OLCR	Optical low coherence reflectometry
OSA	Optical spectrum analyzer
PDL	Polarization dependent loss
PLC	Planar lightwave circuit
PMD	Polarization mode dispersion
PPG	Pseudo-random pattern generator
RDS	Ratio of dispersion slope to second order dispersion
RIN	Relative intensity noise
RPCA	Ratio between the peak of cross and auto correlation
SESAM	Semiconductor saturable-absorber mirror
SHG	Second-harmonic-generation
SM-DCF	Single mode dispersion compensating fibre
SNR	Signal-to-noise-ratio
SSFBG	Super-structured fibre Bragg grating
SVEA	Slowly varying envelope approximation
TH-CDMA	Time hopping code division multiple access
TMM	Transfer matrix method
TOD	Third order dispersion
UV	Ultraviolet
VIPA	Virtually imaged phased array
WDM	Wavelength division multiplex

Chapter 1

Thesis overview

1.1 Background

Fibre technologies find great success in various applications, including laser, communication and sensor systems. Accompanying this evolution is the proliferation of new optical devices. Fibre Bragg gratings (FBGs), which are inherently compatible with optical fibres, are emerging as one of the key components in fibre systems due to their versatility and unique filtering capabilities [1-2]. The design and fabrication techniques for FBGs are still maturing.

Many powerful devices and valuable applications have been exploited using fibre Bragg gratings [3-5]. In laser systems, FBGs are used as wavelength-selective reflectors or wavelength-stabilization devices. In wavelength division multiplexed (WDM) optical networks, FBGs can be used as WDM de-multiplexers or add/drop multiplexers, and chirped FBGs (CFBGs) can compensate chromatic dispersion in transmission fibres. FBGs with complex structures have also been demonstrated to carry out advanced optical processing, such as pulse shaping, matched filtering, pulse compression and other signal manipulation functions. In sensor systems, FBGs are used for providing distributed sensing of strain and temperature.

Super-structured fibre Bragg gratings (SSFBGs) have been developed to implement all-optical code generation and recognition in optical code division multiple access (OCDMA) systems [6]. SSFBG en/decoders, with a spatial phase distribution following a particular address code, can be easily designed and fabricated to achieve temporal-phase-encoding, which provides far better correlation performances than the amplitude-only encoding. In the encoding process, the optical pulses are reflected from the SSFBG encoder, and the spatial phase of the encoder is encrypted into the temporal phase of the encoded pulse. For successful decoding, the encoded pulses must be reflected from an

SSFBG decoder having a conjugate address code to the encoder. The spatial phase distributions in conventional SSFBG en/decoders are formed by inserting discrete phase-shifts in the process of grating writing.

Dynamic dispersion or dispersion slope compensation is one of the most important applications of FBGs. In a high-bit-rate systems, such as 40Gb/s or 160Gb/s transmission system, due to the large signal bandwidth, the dispersion tolerance becomes so small that even a tiny variation in dispersion can severely influence the network performance and, therefore, a dynamic dispersion compensation is required in these systems [7-8]. The function of dynamic dispersion tuning can be realized by using a tunable FBG. The Bragg wavelength of an FBG is sensitive to temperature or strain. By applying a variable temperature or strain distribution along an FBG, its dispersion or dispersion slope could be dynamically controlled. For a dynamic dispersion compensator, a wide dispersion tuning range is essential and it is also highly desirable that the central wavelength is invariant during the dispersion tuning. For a dynamic dispersion slope compensator based on an FBG, it is crucial that there is no additional dispersion while the dispersion slope is adjusted.

1.2 Motivations and main achievements

To improve the functionality and flexibility of OCDMA based optical networks, it is desirable to have OCDMA en/decoders with the capacity of dynamic reconfiguration. Recently, a reconfigurable phase en/decoder has been demonstrated [9]. It is composed of a uniform fibre Bragg grating and a series of equidistant tungsten wires in contact with the FBG. However, in that work, the specific distribution of thermally induced phase-shifts in the reconfigurable devices was not characterized.

In this thesis, we develop a pulse response method, by which the spatial phase distribution in a reconfigurable phase en/decoder could be directly obtained from measuring temporal phases of the reflected optical pulses from the FBG. Using the new characterization scheme, we measure the thermally induced phase distribution produced by tungsten wires with different diameters. Full characterization of the phase distribution also helps us to understand and analyze OCDMA systems using the reconfigurable phase en/decoders. New reconfigurable-phase devices are then constructed using the wire which produces the most confined phase-shifts. The devices' capacity to conduct fast dynamic reconfiguration is also demonstrated.

In a reconfigurable OCDMA system, the reconfigurable-phase decoders are used to retrieve the signals from fixed-code SSFBG encoders. In conventional fix-code devices, the phase-shifts are discrete, while in a reconfigurable-phase decoder, the phase-shifts are inherently distributed. Therefore, under the same nominal code sequence, the spatial phase distribution in a reconfigurable-phase en/decoder only roughly follows that of a discrete-phase en/decoder. In this thesis, we propose and experimentally demonstrate a novel fixed-code en/decoder with a phase profile designed to accurately match a reconfigurable en/decoder. This new continuous-phase device has the inherent advantage to be able to operate together with reconfigurable-phase devices in a reconfigurable OCDMA system.

By embedding a linearly chirped FBG in a uniform beam and bending the beam in an S-shape, the dispersion of the FBG could be controlled while its central wavelength was invariant [10]. This unique advantage gives the S-bending technique great potential in tuning the dispersion or dispersion slope of an FBG. In this thesis, using the S-bending technique, we develop several novel device configurations and applications, including a tunable dispersion compensator with a wide tuning range, a tunable pure dispersion slope compensator, and also an application in tuning the output pulse width of a fibre laser.

1.3 Organization of the thesis

The thesis is divided into three main subsections. Chapter 2 is an introduction to fibre Bragg gratings. The theoretical parts include how to analyze or synthesize FBGs. Then, the manufacturing and characterization techniques of fibre Bragg gratings are summarized. Also reviewed are the applications of FBGs, including fundamental applications, advanced applications and tunability of fibre Bragg gratings.

The first Subsection is Chapter 3, in which the pulse response method is developed to characterize the spatial phase of an FBG. A frequency-resolved-optical-gating (FROG) technique, based on an electro-absorption modulator (EAM), is used to measure the amplitude and phase of the reflection pulses from an FBG [11]. Under the weak grating approximation, the spatial phase of the grating is directly retrieved from the temporal phase of its pulse response. FBGs with discrete or distributed phase-shifts are characterized using this technique. The methods and results reported in this chapter forms the framework to analyse and design reconfigurable-phase OCDMA en/decoders.

The second Subsection is about the three types of FBG-based OCDMA en/decoders and their system performances. From the point of view of fibre Bragg gratings, Chapter 4 introduces the principles and design of OCDMA systems based on conventional discrete-phase en/decoders. The issues, such as the effects of grating strength, choice of input pulse width, tolerance of central wavelength offset between encoders and decoders, choice of chip length and chip number are discussed. Chapter 5 is related to the reconfigurable-phase OCDMA en/decoders. Based on the characterization of the phase distribution in a reconfigurable-phase en/decoder, the OCDMA system using the reconfigurable-phase devices are analyzed and tested. In Chapter 6, we propose and demonstrate a fixed-code and continuous-phase OCDMA en/decoder, which has the same spatial refractive index distribution as a reconfigurable optical phase encoder-decoder for the same nominal code sequences, and therefore is inherently suitable for the application in a reconfigurable OCDMA system.

The third Subsection is on tuning the dispersion (or dispersion slope) in FBGs using an S-bending technique. Chapter 7 first reviews the dispersion in fibres, the dispersion compensation methods using chirped FBGs or other techniques, and dynamic dispersion compensation techniques using tunable FBGs. Then, the S-bending technique and dispersion tuning devices based on it are described. Following this are two novel devices based on the S-bending technique. One is a tunable dispersion compensator with an enhanced dispersion tuning range, and the other is a tunable pure dispersion slope compensator. Applications of tunable dispersion in controlling the pulse width of a soliton fibre laser are then reported.

The final chapter gives a summary and possible future directions related to the work reported in this thesis.

Chapter 2

Introduction to fibre Bragg gratings

2.1 Analysis of fibre Bragg gratings

A fibre grating is a fibre on which a periodic or quasi-periodic index modulation profile is formed in the core. A fibre Bragg grating is simply an optical diffraction grating [12], in which the incident optical field within the fibre is reflected by successive scattering from the index variations. In a fibre Bragg grating, coupling mainly occurs between two identical modes travelling in opposite directions and, according to the grating equation, constructive interference only occurs as the Bragg reflection condition is fulfilled, i.e.

$$\lambda_B = 2n_{eff}\Lambda \tag{2.1}$$

where λ_B is the Bragg wavelength, n_{eff} is the effective modal index and Λ is the grating pitch.

2.1.1 Coupled mode equations

The grating is treated as a perturbation to the refractive index of the fibre, described by,

$$\Delta n(z) = \Delta n_{dc}(z) + \Delta n_{ac}(z)\cos\left[\frac{2\pi}{\Lambda}z + \theta(z)\right]. \tag{2.2}$$

where, $\Delta n_{ac}(z)$ and $\Delta n_{dc}(z)$ are respectively the "ac" and "dc" index perturbation, Λ is the nominal period and $\theta(z)$ is the grating phase once the $2\pi z/\Lambda$ dependence is removed. If the unperturbed fibre has a refractive index profile $\bar{n}(x, y)$, the overall refractive index profile of the perturbed fibre will be

$$n(x, y, z) = \bar{n}(x, y) + \Delta n(z) \tag{2.3}$$

Fibres are weakly guiding, so we assume $\bar{n} \cong n \cong n_{eff} \cong n_{cl}$, where n_{cl} is the refractive index in the cladding and n_{eff} is the effective refractive index of the guided mode of the unperturbed fibre.

Near the Bragg wavelength, reflection of a mode into an identical counter-propagating mode is the dominant interaction in a Bragg grating. In the ideal mode approximation to coupled-mode theory [1][13-15], we assume that the total electric fields in a Bragg grating can be represented as a superposition of the modes in an ideal waveguide without grating perturbation,

$$E(x,y,z,t) = [A(z)\exp(i\beta z) + B(z)\exp(-i\beta z)]\cdot\Psi(x,y)\cdot\exp(-i\omega t) \tag{2.4}$$

where $A(z)\exp(i\beta z)$ and $B(z)\exp(-i\beta z)$ are respectively the z-dependence of forward and backward modes, $\beta(\omega) = n_{eff}k$ is the scalar mode propagation constant, and $k = 2\pi/\lambda$ is the propagation constant in vacuum. Function $\Psi(x,y)$ describes the transverse dependence of the electrical field. It satisfies the scalar wave equation for the unperturbed fibre,

$$\left[\frac{\partial^2}{\partial x^2} + \frac{\partial^2}{\partial y^2} + k^2\bar{n}^2(x,y) - \beta^2\right]\cdot\Psi(x,y) = 0\,. \tag{2.5}$$

The total electric fields $E(x,y,z,t)$ satisfy the scalar wave equation for the perturbed fibre,

$$\left[\frac{\partial^2}{\partial x^2} + \frac{\partial^2}{\partial y^2} + \frac{\partial^2}{\partial z^2} + k^2 n^2(x,y,z)\right]\cdot E(x,y,z,t) = 0\,. \tag{2.6}$$

In weak coupling, further simplification is possible by applying the slowly varying envelope approximation (SVEA). This requires that the amplitude of the mode change slowly over a distance of the light wavelength as

$$\frac{\partial^2 A}{\partial z^2} << \beta\frac{\partial A}{\partial z} \tag{2.7}$$

Substituting Eq. (2.4) into (2.6), and using Eq. (2.3), (2.5) and (2.7) leads to

$$\left[\frac{dA}{dz}\exp(i\beta z) - \frac{dB}{dz}\exp(-i\beta z)\right]\Psi(x,y) = i\frac{k^2}{2\beta}\left(n^2 - \bar{n}^2\right)[A\exp(i\beta z) + B\exp(-i\beta z)]\Psi(x,y) \tag{2.8}$$

Multiplying both sides by $\Psi^*(x,y)$, integrating over the xy-plane, and using the relation $n^2 - \bar{n}^2 \approx 2n\cdot\Delta n$, results in

$$\begin{aligned}&\frac{dA}{dz}\exp(i\beta z) - \frac{dB}{dz}\exp(-i\beta z)\\ &= ik[A\exp(i\beta z) + B\exp(-i\beta z)]\cdot\left[\Delta n_{dc} + \Delta n_{ac}\frac{1}{2}\left(\exp\left[i\left(\frac{2\pi}{\Lambda} + \theta(z)\right)\right] + \exp\left[-i\left(\frac{2\pi}{\Lambda} + \theta(z)\right)\right]\right)\right]\end{aligned} \tag{2.9}$$

Eq. (2.9) can be greatly simplified by considering the synchronous approximation [14], which neglects terms that contain a rapidly oscillating z dependence, since this contributes little to the growth and decay of the amplitudes. This is also an application of momentum conservation in the system

$$\beta = -\beta + \frac{2\pi}{\Lambda} \tag{2.10}$$

This is valid if the interaction is close to the Bragg wavelength

$$\lambda_B = 2n_{eff}\Lambda \tag{2.11}$$

The following coupled mode equations (CME) are then obtained from Eq. (2.9),

$$\frac{dA}{dz} = i\sigma A + i\kappa B\exp[-i(2\delta z - \theta(z))] \tag{2.12a}$$

$$\frac{dB}{dz} = -i\sigma B - i\kappa A\exp[i(2\delta z - \theta(z))] \tag{2.12b}$$

where

$$\sigma(z) = \frac{2\pi}{\lambda}\cdot\Delta n_{dc}(z) \tag{2.13}$$

$$\kappa(z) = \frac{\pi}{\lambda}\cdot\Delta n_{ac}(z) \tag{2.14}$$

$$\delta = \beta - \frac{\pi}{\Lambda} \tag{2.15}$$

and $\sigma(z)$ is the 'dc' coupling constant, $\kappa(z)$ is the 'ac' coupling constant, δ is the frequency detuning parameter.

To transform Eq. (2.12) into the simplest canonical form, new amplitudes $u(z,\delta)$ and $v(z,\delta)$ are introduced, which are related to the forward and backward fields $A(z)\exp(i\beta z)$ and $B(z)\exp(-i\beta z)$ by

$$u(z,\delta) = A(z)\exp(i\beta z)\exp\left(-i\frac{\pi}{\Lambda}z\right)\exp\left(-i\frac{2\pi}{\lambda_B}\int_0^z \Delta n_{dc}(z')dz'\right) \tag{2.16a}$$

$$v(z,\delta) = B(z)\exp(-i\beta z)\exp\left(+i\frac{\pi}{\Lambda}z\right)\exp\left(+i\frac{2\pi}{\lambda_B}\int_0^z \Delta n_{dc}(z')dz'\right) \tag{2.16b}$$

Substituting (2.16) into (2.12) leads to the final coupled mode equations [16]

$$\frac{d}{dz}u(z,\delta) = +i\delta u(z,\delta) + q(z)v(z,\delta) \tag{2.17a}$$

$$\frac{d}{dz}v(z,\delta) = -i\delta v(z,\delta) + q^*(z)u(z,\delta) \tag{2.17a}$$

Note that the scaling factors in (2.16) are independent of frequency. Hence, we can simply treat the new variables $u(z,\delta)$ and $v(z,\delta)$ as fields themselves once the reference planes have been fixed. The coupling coefficient $q(z)$ is related to the index profile as

$$q(z)=\frac{\pi\Delta n_{ac}(z)}{\lambda_B}\exp\left[i\left(\theta(z)-\frac{4\pi}{\lambda_B}\int_0^z\Delta n_{dc}(z')dz'+\frac{\pi}{2}\right)\right] \tag{2.18}$$

or,

$$q(z)=\kappa(z)\exp\left[i\left(\theta(z)-2\int_0^z\sigma(z')dz'+\frac{\pi}{2}\right)\right] \tag{2.19}$$

The modulus of the coupling coefficient $q(z)$ determines the *grating amplitude*, and the phase corresponds to *the grating phase* envelope, which is composed of grating chirp, average refractive index profile $\Delta n_{dc}(z)$, and discrete phase-shifts. Note that the phase term due to the "dc" index perturbation $\Delta n_{dc}(z)$ has the same effect as the geometrical phase θ; as a result the two types of phase contributions cannot be separately identified from the grating response.

2.1.2 Solving the coupled mode equations

Uniform gratings

The coupled mode equations can be solved analytically when the grating is uniform, that is, when $\kappa(z)$ and $\sigma(z)$ are constant and $d\theta(z)/dz$ =0. In this condition, Eqs.(2.17) are coupled first-order ordinary differential equations with constant coefficients. The reflectivity of a uniform fibre grating of length L can be found by assuming $u(0,\delta)=1$, which means that the forward-going wave is constant at the incident, and $v(L,\delta)=0$, which means that no backward-going wave exists at the end of the grating. Then the resultant amplitude reflection coefficient can be shown to be

$$r(\delta)=\frac{v(0,\delta)}{u(0,\delta)}=\frac{-q^*\sinh(\gamma L)}{\gamma\cosh(\gamma L)-i\delta\sinh(\gamma L)} \tag{2.20}$$

where, $\gamma=\sqrt{|q|^2-\delta^2}$ is the propagation constant inside the scattering region. The value of γ defines the band-gap of gratings. Inside the band-gap, γ is real and the propagation is evanescent, while outside the band-gap, γ is imaginary and normal propagation occurs [17].

Transfer matrix method

For non-uniform gratings, the reflection and transmission spectra can only be solved numerically. One approach is the direct numerical integration using the Runge-Kutta method [18], which is straightforward but usually very slow. The often preferred and more efficient approach is the transfer matrix method (TMM) [19].

The transfer matrix method is a piecewise-uniform approach. The grating is divided into N uniform sections, each section with a length $\Delta z_j \left(j = 1,2,\cdots,N\right)$. Each sub-grating should be long enough so that the synchronous approximation still holds, but sufficiently short so that it can be treated as a uniform grating. Solving the coupled mode equations of each sub-grating, seen as a uniform grating, yields the following transfer matrix relation

$$\begin{bmatrix} u\left(z_j + \Delta z_j\right) \\ v\left(z_j + \Delta z_j\right) \end{bmatrix} = T_j \cdot \begin{bmatrix} u\left(z_j\right) \\ v\left(z_j\right) \end{bmatrix} \tag{2.21}$$

$$T_j = \begin{bmatrix} \cosh\left(\gamma_j \cdot \Delta z_j\right) + i\frac{\delta_j}{\gamma_j}\sinh\left(\gamma_j \cdot \Delta z_j\right) & \frac{q_j}{\gamma_j}\sinh\left(\gamma_j \cdot \Delta z_j\right) \\ \frac{q_j^*}{\gamma_j}\sinh\left(\gamma_j \cdot \Delta z_j\right) & \cosh\left(\gamma_j \cdot \Delta z_j\right) - i\frac{\delta_j}{\gamma_j}\sinh\left(\gamma_j \cdot \Delta z_j\right) \end{bmatrix} \tag{2.22}$$

The matrix T_j connects the fields between z_j and $z_j + \Delta z_j$. Hence, the fields at the two ends of the grating could be connected through

$$\begin{bmatrix} u(L) \\ v(L) \end{bmatrix} = T_N \cdot T_{N-1} \cdots T_1 \begin{bmatrix} u(0) \\ v(0) \end{bmatrix} = T \begin{bmatrix} u(0) \\ v(0) \end{bmatrix} \tag{2.23}$$

where $T = T_N \cdot T_{N-1} \cdots T_1$ is the overall transfer matrix of the complex grating. The overall matrix T is a 2×2 matrix

$$T = \begin{bmatrix} T_{11} & T_{12} \\ T_{21} & T_{22} \end{bmatrix} \tag{2.24}$$

Once T is found, by using the boundary conditions ($u(0) = 1$, and $v(L) = 0$), the reflection coefficient and transmission coefficient of the grating is obtained as

$$r(\delta) = -\frac{T_{21}}{T_{22}} \tag{2.25}$$

$$t(\delta) = \frac{1}{T_{22}} \tag{2.26}$$

The transfer matrix method is stable and efficient since relatively few sections are required for accurately analyzing most common gratings.

2.1.3 Weak gratings

As the grating is very weak, that is, in the limit $q \to 0$, solutions of the coupled-code equations (2.17) are $u = u_0 \exp(i\delta z)$ and $v = v_0 \exp(-i\delta z)$. Using the boundary condition, they are reduced to $u = \exp(i\delta z)$ and $v = 0$. In this case, the first order Born approximation means that the forward propagating wave is unaffected by the grating, and so $u = \exp(i\delta z)$. By substituting this into Eq. (2.17) and using the boundary condition, we obtain the grating reflection coefficient [20]

$$r(\delta) = -\int_0^L q^*(z)\exp(i2\delta z)dz \tag{2.27}$$

where L is the length of the grating. A Fourier transform relationship is established between the grating coupling coefficient $q^*(z)$ and its reflection spectrum $r(\delta)$,

$$q^*(z) = -\int_{-\infty}^{+\infty} r(\delta)\exp(-i2\delta z)d\delta \tag{2.28}$$

Although this Fourier transform relation does not hold when the grating is strong, the information from this Fourier transform is still valuable in the analysis and design for fibre Bragg gratings.

In the following, we will show that, in the weak grating approximation, there is a linear relationship between the complex coupling coefficient *q(z)* and reflection impulse response *h(t)* of FBGs. The time delay *t* of light reflected from an FBG at the spatial point *z* is,

$$t = \frac{2n_{eff}}{c} z \tag{2.29}$$

where, c is light speed in the vacuum, and n_{eff} is the dc effective index in an FBG. Substituting Eq.(2.29) into (2.27) leads to

$$r(\omega) = -\frac{c}{2n_{eff}} \int_0^{\frac{2n_{eff}}{c}L} q^*\left(\frac{c}{2n_{eff}}t\right)\exp(i\omega t)dt \tag{2.30}$$

The impulse response of an FBG is the inverse Fourier transform of its frequency response,

$$r(\omega) = \frac{1}{2\pi}\int_{-\infty}^{+\infty} h(t)\exp(i\omega t)dt \tag{2.31}$$

Comparing Eq.(2.30) and (2.31), the impulse response of an FBG can be expressed by its complex coupling coefficient,

$$h(t) = -\alpha q^*\left(\frac{c}{2n_{eff}}t\right) \tag{2.32}$$

where α is a positive constant. Note that from Eq. (2.19), we have,

$$-q^*(z) = \kappa(z)\exp\left[i\left(2\int_0^z \sigma(z')dz' - \theta(z) + \frac{\pi}{2}\right)\right] \tag{2.33}$$

Therefore, using the space-to-time conversion relationship in Eq. (2.29), the phase of the impulse response of an FBG could be directly obtained from its spatial phase $\left[2\int_0^L \sigma(z')dz' - \theta(z)\right]$.

2.2 Synthesis of fibre Bragg gratings

The synthesis of fibre Bragg gratings involves finding the grating structure, which can be expressed by the complex coupling coefficient $q(z)$, from a specified reflection spectrum $r(\delta)$. One approximate method, which is based on the Fourier transform relationship (as shown in Eq. (2.28)) between the complex coupling coefficient and the complex reflection spectrum of a grating, is useful but can only be used to design weak gratings.

The grating synthesis problems can be solved by solving integral equations, but the simplest and most direct approach is the differential or direct method, which is also called the layer-peeling method [21-25]. The layer-peeling method was first developed by geophysicists like Goupillaud and Robinson and was first applied in the field of grating synthesis by Feced et al. [22]. Later, Skaar et al. reformulated and improved it in a simpler form. Our description of the layer-peeling method largely follows that of Skaar et al. [23-24].

The layer-peeling method is based on causality: the coupling coefficient of the first grating layer is determined only by the leading edge of the reflection impulse response, since at the very beginning of the impulse response, light does not have time to propagate more deeply into the grating, and hence, “sees” only the first layer. Thus one can identify the first layer from the desired response. After this, the fields are propagated to the next layer of the grating. Now one is in the same situation as at the beginning, since the effect of the first layer is “peeled off”. This process is continued to the back of the grating, so that the entire grating structure is reconstructed. The layer thickness must be chosen to be

sufficiently small so that the complex coupling coefficient can be approximated as a constant throughout the layer.

The grating synthesis can be facilitated by discretizing the grating into a stack of complex reflectors. The transfer matrix (2.22) can be approximated by a product of two transfer matrices $T_{\Delta z}T_{\rho}$, one (T_{ρ}) describing a discrete reflector, and the other ($T_{\Delta z}$) describing the pure propagation of the fields [22],

$$T_{\rho} = \left(1-|\rho|^2\right)^{-\frac{1}{2}}\begin{bmatrix} 1 & -\rho^* \\ -\rho & 1 \end{bmatrix} \tag{2.34}$$

$$T_{\Delta z} = \begin{bmatrix} \exp(i\delta\cdot\Delta z) & 0 \\ 0 & \exp(-i\delta\cdot\Delta z) \end{bmatrix} \tag{2.35}$$

where the discrete, complex reflection coefficient is given by

$$\rho = -\tanh(|q|\cdot\Delta z)\frac{q^*}{|q|}. \tag{2.36}$$

The reflector matrix T_{ρ} is obtained from *T* by letting $|q|\to\infty$ and holding the total coupling $|q|\Delta z$ constant, and the propagation matrix $T_{\Delta z}$ is obtained by letting $q\to 0$.

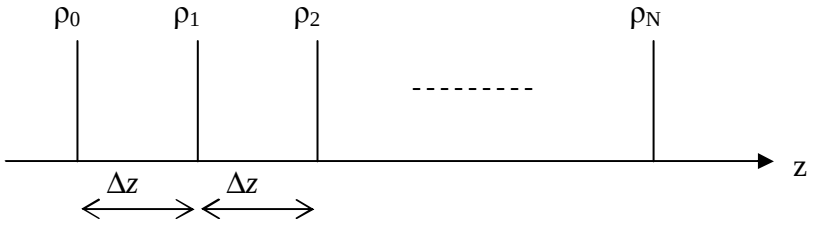

Fig 2.1 A discrete grating model

Then, the grating can be represented as a stack of $N+1$ complex reflectors ρ_j for $j=0,1,\ldots,N$, separated by N propagation sections Δz, as shown in Fig. 2.1. Using (2.34) and (2.35), it can be shown that transferring the fields by the matrix $T_{\Delta z}T_{\rho}$ can also be described as

$$r_{j+1}(\delta) = \exp(-i2\delta\Delta z)\frac{r_j(\delta)-\rho_j}{1-\rho_j^* r_j(\delta)} \tag{2.37}$$

where $r_j(\delta) = v_j(\delta)/u_j(\delta)$.

Under the discrete model of gratings, the reconstruction problem can be stated as finding the coupling coefficients q_j for $j = 0,1,\ldots,N$ through the given reflection spectrum $r(\delta)$ in the interval $-\delta_\omega/2 \le \delta < \delta_\omega/2$.

The reflection impulse response $h(k)$ of the discrete grating is also discrete. It can be determined by calculating the discrete-time inverse Fourier transform of the reflection spectrum $r(\delta)$

$$h(m) = \sum_{\delta=-\delta_\omega/2}^{\delta=\delta_\omega/2} r(\delta)\exp(-i\delta \cdot m \cdot 2\Delta z) \tag{2.38}$$

because the impulse response is discrete with the sample period $2\Delta z$, which is equivalent to the round-trip propagation length of one layer. It follows that $r(\delta)$ is periodic with the spectral period

$$\delta_\omega = \pi/\Delta z\,. \tag{2.39}$$

The layer-peeling algorithm is based on the simple fact that the first point of the impulse response must be independent of the ρ_j's for $j \ge 1$ due to causality. Hence,

$$\rho_0 = h(0)\,. \tag{2.40}$$

Since ρ_0 is already known, we can propagate the fields using (2.37), yielding the fields at the next layer. The algorithm can be described as follows.

(1) Compute $\rho_0 = h(0)$ from $r_0(\delta)$ using (2.38).

(2) Calculate $r_1(\delta)$ from $r_0(\delta)$ and ρ_0 using (2.37).

(3) Repeat step (1) and step (2) until the entire grating structure is determined.

2.3 Formation of fibre Bragg gratings

2.3.1 Photosensitivity in optical fibres

Photosensitivity refers to a permanent change in refractive index induced by exposure to light radiation. Ref [1-2] gives a general review on the photosensitivity of fibres and the routes to photosensitization. In silica (SiO_2) fibres, it is recognized that the germanium (Ge) related defect centres are the major contributors to photosensitivity. Standard telecommunication fibres show weak photosensitivity because of their low Ge concentration. High-Ge-doped fibres can exhibit slightly higher photosensitivity due to the increase of Ge concentration. Doping with boron in the Ge-Si optical fibre can improve the photosensitivity further and another advantage of the presence of boron is

the large reduction in the background refractive index, consequently allowing more Ge to be added in the core for a given core-cladding refractive index difference. Higher photosensitivity can by achieved by soaking Ge-doped fibre in hydrogen [26].

Typical values for the index change in FBGs are ranging between 10^{-6} and 10^{-3}, depending on the UV-exposure and the type of the fibre. By using techniques such as hydrogen soaking, an index change as high as 10^{-2} could be obtained [27].

2.3.2 Fabrication of fibre Bragg gratings

The first fibre grating was formed using the internal writing technique [28], but this can only be used to fabricate the so called 'Hill' grating, which unfortunately only functions close to the wavelength of the writing light. The holographic technique, based on an interferometric structure, was first demonstrated by Meltz et al. [29]. The UV light is first divided into two beams at a beam splitter and then recombined at a certain mutual angle to produce a periodic interference pattern that writes a corresponding periodic index grating in the core of optical fibres. The Bragg wavelength of gratings fabricated by this technique depends on the irradiation wavelength and the mutual angle between the two beams. Therefore, gratings with different Bragg wavelengths can be written by changing the mutual angle. Its main disadvantage is its susceptibility to mechanical vibration.

The holographic technique has been largely superseded by the phase mask technique [30-31]. A phase mask is a uni-dimensional surface-relief grating of period Λ_{PM} etched in a UV-transmitting silica plate, with a carefully controlled mark-space ratio and etching depth. It is designed such that the maximum diffraction efficiency is obtained for the ± 1 orders and the zero order is minimized. UV light, which is incident normal to the phase mask, passes through the mask and a near-field pattern with periodicity $\Lambda = \Lambda_{PM}/2$ is produced by interference of the ± 1 orders. The interference pattern is then imprinted on the fibre core by placing the optical fibre in contact with the phase mask. Through the introduction of a phase mask, sensitivity to mechanical vibrations is minimized. Furthermore, it is possible to scan the UV beam through the phase-mask so that the length of the written grating is not limited by the interference pattern size.

The drawbacks of the phase mask technique are its inherent lack of flexibility and as a result the high-cost considering that fabricating each grating with a new structure requires a new phase mask to be fabricated. In the following section, a continuous grating writing technique will be discussed.

2.3.3 Continuous grating writing techniques

To improve the flexibility of the phase mask technique, a moving fibre-scanning beam approach [32-33] was demonstrated, in which the photosensitive fibre moves slowly relative to the phase mask while the UV beam scans over a phase mask. By controlling the movement of the fibre, various complex gratings could be fabricated using a simple uniform phase mask. Gratings detuned from the fundamental Bragg wavelength of the phase mask are obtained if a fixed moving velocity is applied to the fibre; chirped structures are achieved by applying acceleration; step phase is inserted by moving the fibre through an appropriate fraction of the grating pitch; apodization is accomplished by the application of a dither to the fibre during writing.

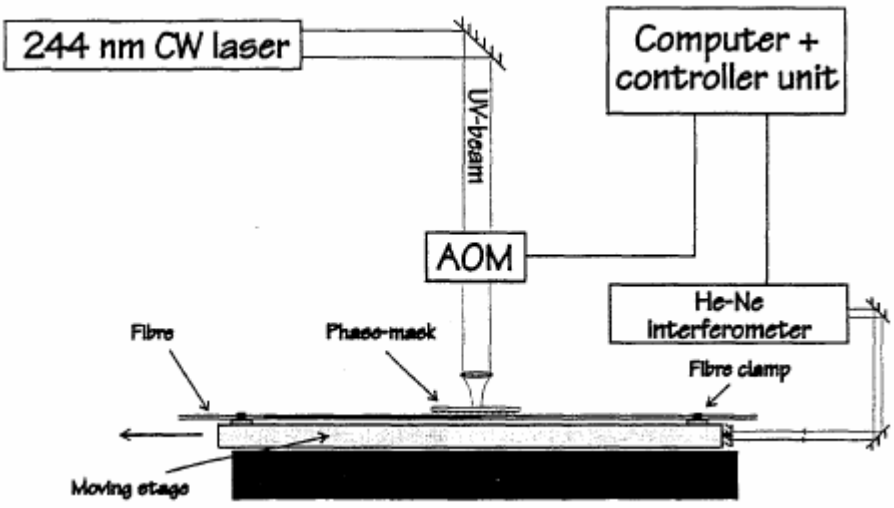

Fig.2.2 Fabrication setup for the continuous grating writing [36].

A more effective approach is the continuous grating writing technique [34-40]. A typical fabrication setup is shown in Fig.2.2. Instead of writing a grating element at a time, the idea is to write a sub-grating per irradiation step, and the whole grating is formed by writing a number of sub-gratings [41]. The UV beam does not scan the phase mask and the phase mask is also stationary. The fibre is translated with constant speed relative to the UV-fringes, with its position being accurately tracked by a Michelson interferometer with a sub-nanometre accuracy in displacement measurement. Each sub-grating is formed by using the data of fibre positions and modulating the UV-laser power

to be on as the fibre reaches the desired position for irradiation. The length of the grating fabricated is therefore no longer limited by the length of the phase-mask.

A fibre grating with complex structures, such as apodization, chirp and discrete phase shifts can be written by controlling the relative phase (position) of consecutive sub-gratings on a local basis. Apodization is obtained by considering the grating as formed by many consecutive pairs of sub-gratings. If two consecutive sub-gratings are in phase, the resulting grating will grow constructively. If they are shifted by half of the grating pitch with respect to each other, the resulting grating will vanish. Then any value between destructive interference and constructive interference can be obtained by controlling the relative phase between the two sub-gratings. A single phase jump between two sub-gratings produces a discrete phase shift; a linear de-phasing of successive sub-gratings results in a Bragg wavelength change; a quadratic de-phasing of successive sub-gratings causes a linear chirp. Using the continuous grating writing technique enabled gratings with almost arbitrary complex features to be manufactured.

2.4 Characterization of fibre Bragg gratings

A grating can be represented by its complex coupling coefficient (including amplitude and phase), as shown in Eq. (2.18). A grating can also be represented by its transfer characteristics, such as reflection spectral or impulse responses (including intensity and phase). The spectral and impulse responses of a grating are a Fourier transform pair. The spectral response of a grating can be deduced from its spatial profiles using the transfer matrix method (as shown in Section 2.1), while the spatial profile of a grating can be recovered from its frequency response through the inverse scattering method (as shown in Section 2.2) [42-43].

In this section, we will discuss the modulation phase-shift [44-46], optical low coherence reflectometry (OLCR) [47-58] and side diffraction techniques [59-63], which directly measure the spectral response, impulse response and complex coupling coefficient of an FBG, respectively. Other techniques developed for charactering an FBG include the heat scan [64], index perturbation [65] and optical frequency-domain reflectometry (OFDR) techniques [66-67].

2.4.1 Modulation phase-shift method

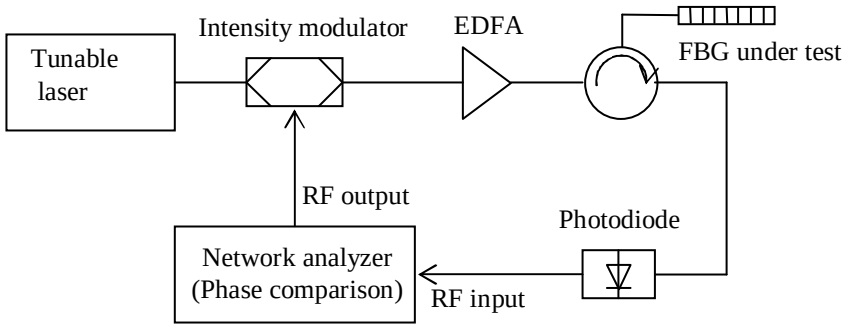

Fig.2.3 Measurement setup for a modulation phase method.

Measuring the intensity of the reflection spectrum of a grating is straightforward. By coupling a broadband source (usually the amplified spontaneous emission (ASE) from a fibre amplifier) via an optical circulator into the fibre grating, the reflected optical power spectrum can be measured by an optical spectrum analyzer (OSA). However, a full characterization also includes the measurement of its phase or time delay response, for which a modulation phase method is frequently used [44].

The setup for a modulation phase method is shown in Fig. 2.3. The light from a tunable laser is modulated by an optical intensity modulator and the driving signal, with a frequency of *f*, is from a network analyser. The modulated light is then launched into the grating to be measured. The reflected signal is detected by a photodiode and then introduced back into the network analyser. The analyzer compares the phase difference between the received signal and the driving electrical signal. As the wavelength of the tunable laser is tuned, the phase difference among different wavelengths $\Delta\phi(\lambda)$ is scanned. The relative time delay at different wavelengths is

$$\tau(\lambda)=\frac{1}{f}\cdot\frac{\Delta\phi(\lambda)}{2\pi}. \tag{2.41}$$

This method has been widely used in characterizing the reflection or transmission time delay spectra of gratings or other optical components. Its main disadvantage is the duration of measurement because temperature variations during the course of measurement may cause errors. Several improved techniques have been proposed to minimize this error, for example, by using the signal following the modulator as a reference or by incorporating a separate reference signal [45-46].

2.4.2 Optical low coherence reflectometry technique

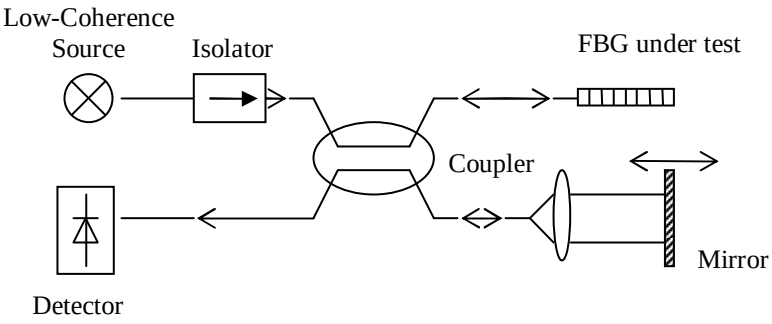

Fig.2.4 Setup for OLCR.

The optical low coherence reflectometry (OLCR) [47-49] is used to directly measure the impulse response of a fibre Bragg grating. The setup is shown in Fig. 2.4, which is a fast scanning Michelson interferometer, with the FBG under test in one arm and a moveable mirror in the other arm. A spatially resolved reflectogram is obtained by varying the optical path length of the other arm. An intuitive explanation of its principle is that interferences only occur when the lengths of both arms are the same to within a coherence length of the light source. The intensity detected by the photodiode can be derived to be [50-52],

$$I(\tau)=\frac{1}{2\pi}\Re\left\{\int_{-\infty}^{+\infty}S(\omega)r(\omega)\exp(i\omega\tau)d\omega\right\} \tag{2.42}$$

where $\Re$ denotes the real part, $S(\omega)$ is the spectrum of the low coherence source, $r(\omega)$ is the complex reflectivity of the grating, $\tau=t_2-t_1$ is the time difference between the two interferometer arms. Therefore, the interferogram is the real part of the Fourier transform of the product of the spectrum of the low coherence source and the complex reflection coefficient of the Bragg grating.

In OLCR, the spectral bandwidth of the source is often much larger than the bandwidth of the FBG under test. In this case, $S(\omega)$ may be treated as a constant, yielding

$$I(\tau)=const\cdot\frac{1}{2\pi}\Re\left\{\int_{-\infty}^{+\infty}r(\omega)\exp(i\omega\tau)d\omega\right\}=const\cdot\Re h_c(\tau) \tag{2.43}$$

Hence, ignoring the background power, the data from the white light interferometer corresponds to the real part of the impulse response of the FBG under investigation. Generally, the amplitude and phase of the pulse response could be obtained by first calculating the imaginary part of the impulse response from the experimentally measured real part using the Hilbert transform, since the impulse response is a causal signal.

Performing an inverse Fourier transform on the measured impulse response yields the reflection and group delay spectrum of the grating [53]. In the case of a weak FBG, the measured impulse response corresponds to the index modulation amplitude and phase (or the complex coupling coefficient). For a stronger FBG, an inverse scattering technique should be used to retrieve the complex coupling coefficient [42, 54-58].

The OLCR measurement can be implemented in one second and therefore is immune to the ambient temperature variations and instrumental shifts. This is a key advantage of the OLCR technique over the modulation phase-shift method.

2.4.3 Side diffraction technique

Although the complex coupling coefficient of a grating could be retrieved from its spectral or impulse response, it requires a sophisticated inverse technique and may be corrupted by noise. Therefore, a direct characterization of the spatial index modulation profile is still necessary. The side scattering technique has been proposed by Krug et al. to measure the ac index modulation externally along the length of a fibre Bragg grating [59]. A short wavelength laser (usually ~633nm) is focused onto the core of the fibre at an angle where the first-order diffracted Bragg condition is satisfied for the probing wavelength. The diffracted light is collected by a lens and an optical detector. The diffracted intensity is directly proportional to the square of the ac index modulation. As the beam is scanned along the length of the grating, the diffracted intensity gives the refractive index modulation profile. A modified technique, the interferometric side scattering technique, can also directly measure the longitudinal changes in period of FBGs, such as chirp, stitching errors and phase-shifts [60-63].

2.5 Review of various fibre Bragg gratings and their applications

2.5.1 Standard fibre Bragg gratings and applications

Advantages of fibre Bragg gratings include low insertion loss, compatibility with existing optical fibres, low cost, and relatively simple fabrication. Fibre Bragg gratings have become a critical part in optical fibre systems [1-5]. Operating in reflection mode, a uniform fibre Bragg grating functions as a narrow-bandwidth mirror or optical band-pass filter, only reflecting the light in a predetermined narrow wavelength range. While on the

transmission mode, it works as an optical band-rejection filter. In WDM optical networks, cascaded fibre Bragg gratings have been used as wavelength division multiplex (WDM) demultiplexers or add/drop multiplexers [68]. In lasers, fibre Bragg gratings are used as the laser cavity of fibre lasers, or used to stabilize the operational wavelength of laser diodes [4] [69-70].

A chirped Bragg grating is a grating with a varying Bragg wavelength along its length. Different wavelength components incident in the grating will be reflected at a different position, and therefore will experience a different time delay in the grating. Hence, chirped Bragg gratings are used as dispersion compensators in transmission systems [71]. Tailoring the chirp of FBGs allows the compensation of higher-order dispersion. Chirped FBGs can also be used to stretch optical pulses for reducing the peak power before amplification, and therefore mitigating nonlinear effects; this is called chirped pulse amplification (CPA) [72]. In ref [73], ~16000 times extreme pulse compression is demonstrated.

Another critical application area of fibre gratings is in sensor systems [5]. Any change in fibre properties, such as strain, or temperature which varies the modal index or grating pitch, will change the Bragg wavelength, and hence the spectrum of the incident optical signal. Therefore, a fibre grating is an intrinsic sensor to temperature or strain.

2.5.2 Advanced fibre Bragg gratings and applications

A distinguishing feature of fibre Bragg gratings is the flexibility they offer for achieving desired spectral characteristics. By controlling the refractive index modulation amplitude, chirp, or phase-shift, we may obtain gratings with flexible reflectivity, bandwidth, and time delay features. Based on this flexibility is the advanced grating fabrication technique: the continuous writing technique, by which a grating with a complex spatial index modulation profile can be fabricated using a uniform phase mask. Summarized in the following are advanced FBGs and their applications.

Fibre DFB laser

In the fibre distributed feedback (DFB) laser, a phase-shifted Bragg grating is incorporated into the active fibre [74]. Its advantage includes: simple all-fibre structure, high stability, tunability, narrow line-width, a low relative intensity noise (RIN), and a precise lasing wavelength.

Dispersion-free filter and pure third order dispersion compensator

The dispersion-free filter [75] and pure third order dispersion compensator [76] are two typical examples to demonstrate the capacity of fibre Bragg gratings in accurate time-delay control. Both of them have complex spatial index modulation profiles, which is composed of multiple pi-phase-shifts and complex apodization. Their design and fabrication also demonstrate the power of the inverse scattering grating design technique and the continuous grating writing technique.

Optical processing using fibre Bragg gratings

As a filter with a versatile amplitude and phase characteristic, a fibre Bragg grating could provide complex optical processing functions to an incident optical signal. Superstructured fibre Bragg gratings (SSFBGs) with a series discrete phase-shifts are successfully utilized as OCDMA encoder/decoders to generate and recognize optical codes [6]. Soliton to rectangular pulse conversion is achieved using a superstructured fibre Bragg grating designed through the Fourier transform technique [77]. Pulse multiplication is demonstrated using a sampled fibre Bragg grating which is in fact a multi-pass-band filter [78].

Optical buffer

The function of optical buffering has been experimentally demonstrated in Moiré or phase-shifted fibre Bragg gratings [79-82]. Optical pulses transmit through the Bragg gratings, and are slowed down due to the photonic resonances in fibre Bragg gratings.

Broadband or multi-channel filters or dispersion compensators

In nature, fibre Bragg gratings are narrowband devices, but they can be made broadband by increasing the grating length, or by making it multichannel through superimposing, Fabry-Pérot (FP) or sampling techniques.

Increasing the length of a chirped FBG will increase its bandwidth, but at the same time, the fabrication error will increase and consequently deteriorate the grating performance seriously. Using a velocity-controlled approach, Brennan et al. reported the realization of 10m-long chirped FBGs [40] [83-84].

A multi-channel dispersion compensator or filter can be made by writing separate FBGs along the fibre, but this will be too large a device. A better approach is to

superimpose multiple FBGs in a common section of the fibre, with each grating being characterized by its central wavelength and dispersion characteristics. Individual gratings do not affect each other, but the number of superimposed gratings is limited by the maximum fibre photosensitivity. Using the superimposing technique, 16-channel 100GHz-spacing dispersion compensators [85-86] and 4-channel 50GHz-spacing dispersion-free WDM filters [87] have been demonstrated.

By writing two chirped FBGs on one optical fibre as wide-band mirrors [88-91], Fabry-Pérot-like filters are formed. Moiré gratings [92] exhibit similar performances as the FP structures. In a fibre FP filter with a reasonable free spectral range (FSR), the two chirped FBGs can possibly be superimposed since its FSR is inversely proportional to the displacement between the two gratings. To obtain a flat amplitude response characteristic, the fibre FP filters have been developed with multiple coupled-cavities [93-94], or been combined with a Mach-Zehnder (MZ) [95] or Michelson interferometer [96-98]. A special fibre FP filter, Gires-Tournois etalon, has also been demonstrated using FBGs, in which the reflectivity of one mirror (FBG) approaches one [99-102]. The fibre FP structure can be used as interleaver or mux/demux filters [95] [97-98] in WDM systems, while operating in reflection mode, they function as multi-channel tunable dispersion or dispersion slope [99-102] compensators.

Another approach is the sampled FBG [103-106], in which a periodic amplitude and/or phase sampling superstructure is imposed on the seed FBG so as to generate a number of equally spaced reflective channels. Simple binary sampling [105] will create channels of un-equal strength and bandwidth, while a sinc-shaped sampling function [107] can produce channels with identical characteristics. However, by amplitude sampling, the increase of channel number will result in the increase of required refractive index to maintain the reflectivity of the grating. Phase sampling [108-110] has been proposed to solve this difficulty. Minimum optimization methods, such as the simulated annealing method [111], simplex method [112], and conjugate gradient method [113] are used for choosing an appropriate phase sampling function. Multi-channel dispersion compensators, mux/demux filters or interleavers [112] [114] have been designed and fabricated using sampled gratings. Sampled gratings can also be made to compensate dispersion slope by chirping the sample period of the gratings [115-117].

2.5.3 Tunable fibre Bragg gratings

Fibre Bragg gratings are sensitive to the strain and temperature applied on them. The strain response arises due to both the physical elongation of the FBG (and the corresponding fractional change in grating pitch), and the change in fibre refractive index due to photo-elastic effects. The thermal response arises due to the inherent thermal expansion of the fibre material and the temperature dependence of the refractive index [5]. The shift of Bragg wavelength with strain and temperature can be expressed by

$$\Delta\lambda_B = \lambda_B\left[(1-\rho_e)\varepsilon + \left(\alpha + \frac{1}{n}\frac{dn}{dT}\right)\Delta T\right] \tag{2.44}$$

where, ε is the applied strain, ρ_e is the photo-elastic constant, α is the coefficient of thermal expansion (CTE) of fibres, and ΔT is the temperature change. For silica fibres, $\rho_e \approx 0.22$. The thermal effect is dominated by the dn/dT effect, which accounts for 95% of the observed shift. Typically, $dn/dT \approx 0.5 \sim 1\times10^{-5}$ $^oC^{-1}$. At a Bragg wavelength of 1500 nm, the change in the Bragg wavelength with temperature is around 0.01~0.02 nm^oC^{-1}.

For a grating with a Bragg wavelength of ~1550nm, the Bragg wavelength shift is 1~2 nm with a temperature variation of 100 ^oC. Bragg grating tuning by strain is limited by the fibre strength. For a tensile strain, a maximum strain of roughly 1% can be applied without degrading the fibre strength and breaking the fibre [118]. The limitations are relieved when a compressive stress is implemented, because silica is 23 times stronger under the compression than under the tension. Therefore, for a grating with a Bragg wavelength of ~1550nm, the maximum Bragg wavelength shift is ~10nm under a tensile strain and ~270nm under a compressive strain. Using the compression tuning technique, a Bragg wavelength tuning range of ~110 nm has been demonstrated experimentally [119].

2.6 An example: FBG design and fabrication

In this section, an FBG is designed and fabricated to reshape an optical pulse by using the inverse scattering technique. The target reflection and time delay spectrum of the grating is shown in Fig. 2.5. It is designed to perfectly compensate the nonlinear chirp of the optical pulse from a gain-switched laser diode [120].

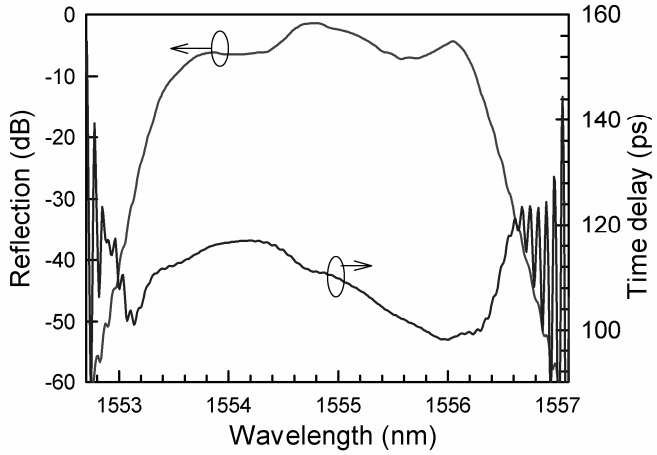

Fig.2.5 The target reflection and time delay spectrum of the grating.

From this target spectrum, the grating is then synthesized by using a homemade program based on the layer-peeling method described in Section 2.2 [23-24]. The resultant effective ac index modulation and Bragg wavelength distributions of the grating are shown in Fig.2.6. Obviously, it is quite a complex grating, since the target spectrum is very complicated.

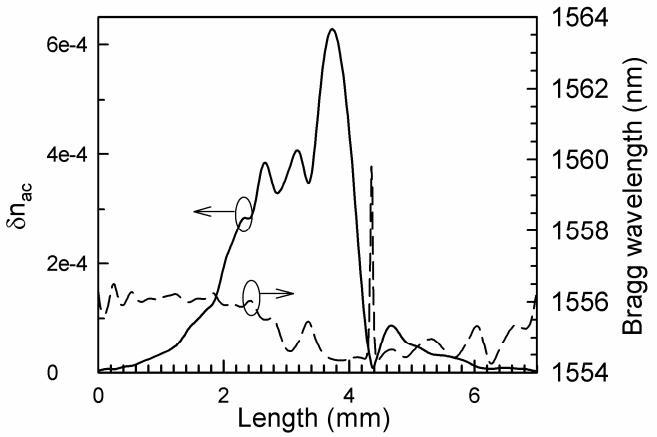

Fig.2.6 The designed grating structure.

Based on the design shown in Fig.2.6, the grating is fabricated using a uniform phase mask and the continuous grating writing technique. As described in Section 2.3, the complex apodization and chirp structure is achieved by controlling the relative phase of consecutive sub-gratings. The reflection and time delay spectrum of the grating are then characterized using the modulation phase-shift method. As shown in Fig. 2.7, the measured spectrum has a good agreement with the target, although they are very complex.

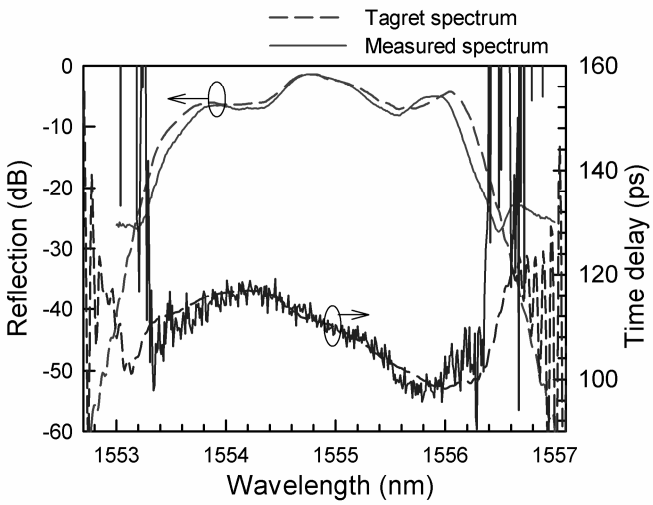

Fig.2.7 Measured (solid lines) and target (dashed lines) spectra of the grating.

This example shows that a grating can be designed and fabricated with a flexible spectral filtering characteristic. It also demonstrates the effectiveness of the grating design and fabrication techniques we use.

Chapter 3

Characterizing spatial phases in FBGs using a pulse response method

3.1 Introduction

As shown in Section 2.1, a fibre Bragg grating (FBG) is described as a refractive index perturbation to the fibre,

$$\Delta n(z) = \Delta n_{dc}(z) + \Delta n_{ac}(z)\cos\left[\frac{2\pi}{\Lambda} + \theta(z)\right]. \tag{3.1}$$

where, $\Delta n_{ac}(z)$ is the ac refractive index modulation, $\Delta n_{dc}(z)$ is the dc (average) refractive index modulation, Λ is the nominal period, and $\theta(z)$ is the grating phase once the $2\pi z/\Lambda$ dependence has been removed. In the coupled-wave formalism, the FBG is defined through the complex coupling coefficient,

$$q(z) = \frac{\pi\Delta n_{ac}(z)}{\lambda_B}\exp\left[i\left(\theta(z) - \frac{4\pi}{\lambda_B}\int_0^z \Delta n_{dc}(z')dz' + \frac{\pi}{2}\right)\right] \tag{3.2}$$

The modulus of the complex coupling coefficient $q(z)$ determines the *grating amplitude*, and the phase of the complex coupling coefficient corresponds to *the grating phase* profile.

Although various techniques, such as side-scattering [59], heat-scan [64] and optical low coherence reflectometry (OLCR) [47], have been proposed to measure the amplitude of the complex coupling coefficient of FBGs, little attention has been paid to the characterization of phase of the complex coupling coefficient. This includes the discrete phase shift, dc refractive index variation (or distributed phase shift), and chirp of FBGs. Although in principle, the OLCR technique could be used to measure the phases of FBGs, the experimental results reported are very limited [51-52].

In this Chapter, we will characterize the full spatial phase profiles of FBGs by directly measuring their pulse response. A short input pulse is incident on the FBG, and the amplitude and phase of the reflection pulses are measured by using a frequency-resolved-optical-gating (FROG) technique, based on an electro-absorption modulator (EAM) as an optical gate. Under the weak grating approximation, the spatial phase of an FBG is related to, and as a result can be directly retrieved from, the temporal phase of its pulse response.

3.2 Characterization principles

3.2.1 Characterizing the spatial phases of FBGs using a pulse response method

The characterization is based on measuring the pulse response of an FBG under test (as shown in Fig. 3.1). A train of short optical pulses is reflected from the FBG. If the input pulse is far shorter compared to the length of the grating, the reflected pulse response is a good approximation to its impulse response.

As shown in Section 2.1.3, if the FBG under test is weak, the spatial phase of a grating will cause an equivalent temporal phase in its impulse response due to the space-time duality. Thus, the spatial phase shift distribution of the grating can be approximately obtained from the temporal phase distribution of its impulse response.

With this method, the discrete phase-shifts, dc refractive index variation and chirp in an FBG could be directly characterized.

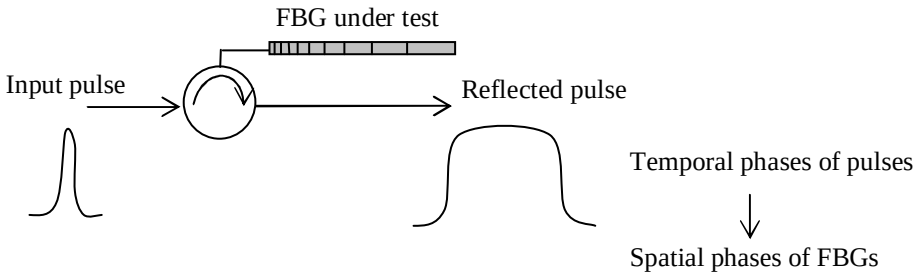

Fig.3.1 Principle of the pulse response method.

A. Discrete phase-shifts

Fibre Bragg gratings with one or more phase-shifts along their length are typically referred to as phase-shifted gratings. Phase shifts are usually introduced by imposing a spatial gap between two sub-gratings during fabrication. If a discrete spatial phase-shift

ϕ_s exists in the grating, there will be a discrete phase-shift ϕ_t in the temporal phase of its pulse response, and the spatial phase is equivalent to the temporal phase, i.e.,

$$\phi_s = \phi_t \ . \tag{3.3}$$

Therefore, the discrete spatial phase of an FBG could be determined by measuring the temporal phase of its pulse response.

B. dc refractive index variation

A dc (average) refractive index variation along the grating will accumulate and form a distributed phase shift. Assuming that the distribution of the dc refractive index variation is $\Delta n_{dc}(x)$ from x_1 to x_2, the resultant phase shift is

$$\phi = \frac{4\pi}{\lambda_B} \int_{x_1}^{x_2} \Delta n_{dc}(x) dx \tag{3.4}$$

where, λ_B is the Bragg wavelength of the FBG. Furthermore, differentiation of Eq. (3.4) with respect to space x gives,

$$\Delta n_{dc}(x) = \frac{\lambda_B}{4\pi} \frac{d\phi}{dx} \tag{3.5}$$

If a distributed spatial phase-shift exists in a grating, there will be a corresponding distributed phase-shift in the temporal phase of its pulse response. From the space-to-time conversion relationship,

$$\Delta t = \frac{2 n_{eff} \Delta x}{c} \tag{3.6}$$

and the approximation that the temporal phase shift is equivalent to the spatial phase shift, a relationship between the dc refractive index distribution of the FBG and the temporal phase distribution of its impulse response can be obtained as:

$$\Delta n_{dc} = \frac{\lambda_B \cdot n_{eff}}{2\pi c} \frac{\Delta\phi}{\Delta t} \ . \tag{3.7}$$

Therefore, from Equation (3.7), the spatial dc refractive index profile of an FBG can be determined by measuring the temporal phase distribution of its impulse response.

C. Chirp

The grating chirp refers to the variation of the grating pitch along the fibre. Using the Bragg relation, $\lambda_B = 2 n_{eff} \Lambda$, we have,

$$\Delta\lambda_B = \lambda_B \frac{\Delta n_{eff}}{n_{eff}} \tag{3.8}$$

From Eq. (3.7), a relationship between the grating chirp and the temporal phase

distribution of its impulse response is obtained as,

$$\Delta\lambda_B = \frac{\lambda_B^2}{2\pi c}\frac{\Delta\phi}{\Delta t}. \tag{3.9}$$

Therefore, the grating chirp is also determined from the temporal phase distribution of its impulse response.

3.2.2 Characterizing optical pulses using the FROG technique based on an EAM

Full characterization of a short optical pulse includes measuring its intensity and phase vs. time. The difficulty lies in that if you want to measure a short event, you need an even shorter one. The intensity vs. time of optical pulses can possibly be measured using an optical sampling oscilloscope, but if the pulse is too short, the measurement will be constrained by the limited bandwidth of practical oscilloscopes. Furthermore, it has not been possible to measure the phase in the time domain directly.

Auto-correlators are also used to measure the intensity vs. time of a short optical pulse [121]. It involves splitting the pulse into two, variably delaying one with respect to the other, spatially overlapping the two pulses by an optical gate, usually through some instantaneously responding nonlinear optical medium, and *measuring the intensity of the overlapped signal* using a detector. Since the autocorrelator measures the pulse to be measured using the pulse itself, it can measure ultrashort (femtosecond) optical pulses which the optical sampling oscilloscope can not measure. However, the information of an optical pulse cannot be completely retrieved from its autocorrelation intensity. For example, auto-correlators are not able to determine the specific shape or phase of optical pulses.

A successful technique which can fully measure short and even ultra-short optical pulses is the frequency-resolved-optical-gating (FROG) technique [121], which is based on the autocorrelation-type measurement, but the autocorrelator signal is *spectrally resolved*. Instead of measuring the autocorrelator signal energy vs. delay, which yields an autocorrelation, FROG involves measuring the autocorrelator signal spectrum vs. delay, which yields a spectrogram. A spectrogram is the time-frequency representation of optical pulses, from which we can extract complete information (including intensity and phase) about the pulse and the gate. The extraction of both the pulse and the gate from the measured spectrogram is the well-known two-dimensional phase-retrieval problem, which can be solved with the principal component generalized projection algorithm [122-

123]. The retrieval does not require any assumptions and can provide the complete description of the pulse and the gate, except for the meaningless absolute time delays and phase constants.

While nonlinear processes are commonly used as the optical gate to measure ultra-short optical pulses, it is also possible to use linear process, for example, a temporal modulator as a gate. Dorrer et al. recently demonstrated this technique using an electro-absorption modulator (EAM) [11] [124]. The use of the temporal gating from a modulator gives the critical advantage of high sensitivity, since it does not rely on nonlinear optics.

3.2.3 Experimental setup for EAM-FROG

The setup for measuring the pulse responses of FBGs through the FROG technique, using an EAM as an optical gate [125-126], is shown in Fig.3.2. This is also the setup we use in our experiments reported in next sections. First, an input optical pulse train is split by a 3dB coupler. The central wavelength of the input pulse train is tuned to the Bragg wavelength of the FBG under test. In one arm, the pulses are reflected from the FBG, and then the reshaped optical pulses are incident into the EAM. In the other arm, the pulse train passes through an optical stage with a controllable time delay, and is detected by a fast (>33GHz) photodiode (PD), and then amplified to generate a sinusoidal electrical drive signal to the EAM as the switching window, which is synchronous with the optical pulse train incident to the EAM. The shaped optical pulses are thus optically sampled by the EAM. By varying the optical delay in a controlled fashion and measuring the optical spectra through an optical spectrum analyzer (OSA), (0.01nm resolution, and >70dB dynamic range), we obtain a spectrogram of the reflected optical pulses from the FBG.

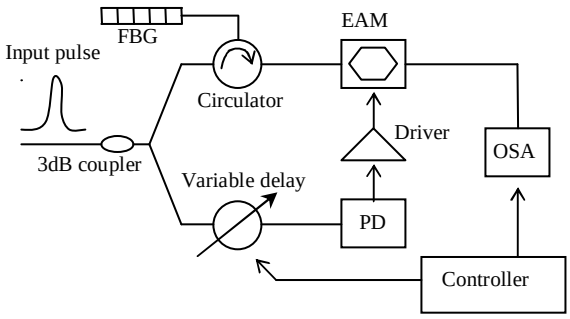

Fig.3.2 The EAM-FROG experimental setup.

The expression for the EAM-FROG spectrogram is given by

$$I_{spect}(\omega,\tau)=\left|\int_{-\infty}^{+\infty}E(t)G(t-\tau)\exp(-i\omega t)\right|^2 \tag{3.10}$$

where $G(t-\tau)$ is a variable-delay gate function, defined by the optically driven EAM switching window. Then, the intensity and phase of the electric field $E(t)$ of shaped optical pulses is extracted from the spectrogram via a numerical retrieval algorithm [122-123], which is not limited by the duration of the gating signal.

3.3 Characterizing discrete phase-shifts in Bragg gratings

3.3.1 Grating parameters and reflection spectra

Table 3.1 Parameters of FBGs to be measured

	Phase	Length (mm)	Strength	Maximum Transmission(dB)
1	0	5	9.25×10^{-5}	3.4
2	0.5π	5	11.2×10^{-5}	4.1
3	π	5	13.0×10^{-5}	3.5
4	1.5π	5	9.2×10^{-5}	2.9

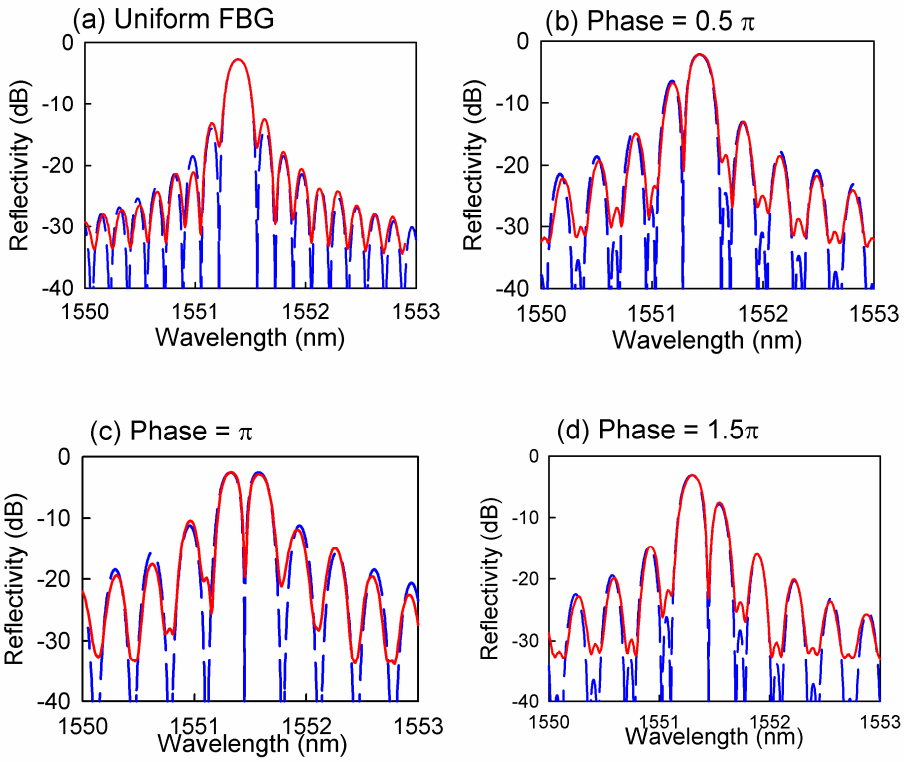

Fig.3.3 Measured (solid lines) and simulated (dashed lines) power reflection spectra of gratings with a phase shift of (a) 0, (b) 0.5π, (c) π and (d) 1.5π respectively.

Four 5mm-long FBGs having a uniform index modulation are fabricated with a discrete phase-shift of 0, 0.5π, π or 1.5π at the center. The parameters of the FBGs are shown in Table. 3.1.

Shown in Fig. 3.3 are the measured (solid lines) and simulated (dashed lines) reflection spectra of the four gratings. The simulation is based on the parameters in Table. 3.1. The agreement between the simulation and measured results demonstrates the good quality of gratings to be characterized.

3.3.2 Experimental results

The experimental setup is as shown in Fig.3.2. The FWHM and repetition rate of the input optical pulse train are, respectively, 2.2-ps and 5GHz. The central wavelength of the input pulse train is tuned to the Bragg wavelength of the FBG. The 5GHz sinusoidal electrical drive signal to the EAM has a pulse width of ~50ps.

Shown in Fig. 3.4 are the measured (a) and retrieved (b) spectrograms of the reflected pulses from the 0.5π phase-shifted grating. An excellent agreement between the measured and retrieved spectrogram is obtained, confirming the quality of the measurement and retrieval process.

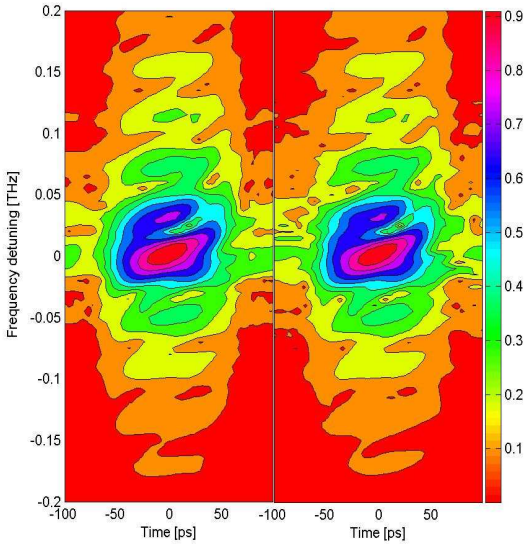

Fig.3.4 (a) Measured and (b) retrieved spectrograms of the reflected pulse from the 0.5π phase-shifted FBG (the input pulse width is 2.2 ps). The RMS retrieval error is 0.0024 on a 128x128 grid [125] [Retrieved spectrogram provided by M. A. F. Roelens].

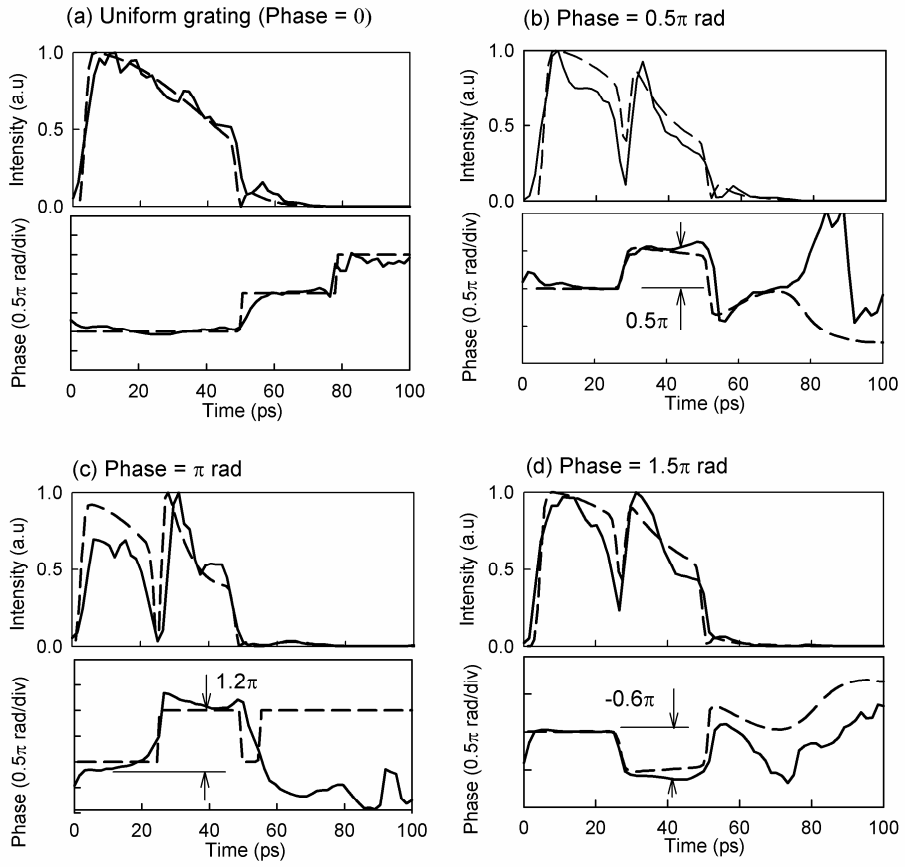

Fig.3.5 Measured (solid line) and simulated (dotted line) temporal intensity and phase of the reflected pulses from the gratings with a discrete phase-shift (a) 0, (b) 0.5π, (c) π and (d) 1.5π respectively.

Shown in Fig. 3.5 are the simulated (dashed lines) and retrieved (solid lines) temporal intensities and phases of reflected pulses from the four gratings. In the numerical simulation, the reflected pulse is calculated through the inverse Fourier transform of the product of the input pulse spectrum and the reflection spectral response of FBG. The simulation is based on the FBG parameters shown in Table. 3.1. The features of the measured results agree well with the simulation. Reflected pulses of all the gratings consist of one or two main pulses and some very weak pulses. For the uniform grating, the main reflected pulse has a square-like shape with a gradual fall-off in intensity and its duration is equal to the round-trip propagation time through the grating ($\Delta t = 2n_{eff} L/c \approx 50 ps$). For the gratings with a phase-shift at their center, the reflected pulses consist of two discrete square-like parts, whose durations are both the round-trip propagation of half the grating length (25 *ps*). For the uniform grating, the temporal phase of the reflected pulse is kept constant through the square-like pulse. For the phase-shifted

gratings, the temporal phases of the two discrete square-like pulses are constant in their own durations, but between them there is an obvious phase step. The amount of simulated temporal phase-shift is equivalent to the spatial phase-shift of the gratings. Note that the discrete phase in the grating is defined as a spatial gap between sub-gratings, and this spatial gap is transformed into the temporal phase in its pulse response. The measured temporal phases almost follow the simulation, not only in the amount of phase-shifts, but also in the distribution. The discrepancy between the measured and simulated temporal-phase-distributions (especially in Fig.3.5 (c)) is mainly due to a lack of stablility in the input optical pulses. The spatial phase-shifts of the gratings, the simulated temporal phase-shifts and the measured temporal phase-shifts are summarized in Table. 3.2. The accuracy of the discrete-phase-shift measurement can be less than 0.1π.

Table.3.2 The amount of measured phases for different FBGs

	Designed spatial phase-shift (rad)	Simulated temporal phase-shift (rad)	Measured temporal phase-shift (rad)
1	0	0	0
2	0.5π	0.5π	0.5π
3	π	π	1.2π
4	1.5π	1.5π	1.4π

As far as we know, this is the first direct characterization of pulse responses and discrete phase-shifts for fibre Bragg gratings, although pulse responses of FBGs have already been studied by numerical simulation [127]. Shown here are only the results for FBGs with a single phase-shift. Using the same techniques, we also measured the superstructured FBGs (SSFBG) with as much as 15 discrete phase-shifts [126].

The measurements experimentally demonstrate the function of temporal-phase-encoding of phase-shifted FBGs, which is the basis for OCDMA systems based on SSFBGs (to be shown in Chapter 4).

3.4 Characterizing dc refractive index variations in Bragg gratings

3.4.1 FBGs with a tunable and distributed phase-shift

As shown in Fig.3.6, to obtain a tunable phase-shift in an FBG, a fine tungsten wire is

put in contact with a uniform FBG and an electric current passes through the wire [9]. The heat produced by the electrical current will affect the FBG due to the temperature increase. The effect can be described by the Bragg wavelength shift [5]

$$\Delta\lambda_B = \lambda_B\left(\alpha + \frac{1}{n_{eff}}\frac{dn_{eff}}{dT}\right)\Delta T \tag{3.11}$$

where, ΔT is the temperature variation. The first item describes the thermal expansion effect, and α is the coefficient of thermal expansion (CTE) of the fibre. The second item describes thermally induced dc effective index change (dn_{eff}/dT). In silica fibres, the thermal effect is dominated by the dn_{eff}/dT effect, which accounts for 95% of the observed shift. Typically, $dn_{eff}/dT \approx 0.5 \sim 1\times10^{-5}\,^{\circ}C^{-1}$. In Eq. (3.11), the overall effect is described by a Bragg wavelength shift, and equivalently, it can be described by an effective index variation,

$$\Delta n_{eff} = n_{eff}\left(\alpha + \frac{1}{n_{eff}}\frac{dn_{eff}}{dT}\right)\Delta T \tag{3.12}$$

According to Eq. (3.4), an effective index variation $\Delta n_{eff}(x)$ along an FBG will accumulate and form a distributed phase shift,

$$\phi = \frac{4\pi}{\lambda_B}\int_{x_1}^{x_2}\Delta n_{eff}(x)dx \tag{3.13}$$

If the electrical current on the tungsten wire is tuned, different temperature distributions, and hence different current-induced phase-shifts, can be obtained.

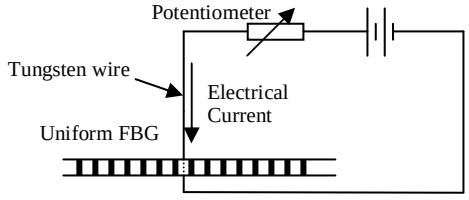

Fig.3.6 The structure of an FBG with a wire-induced phase shift.

This principle forms the basis of the reconfigurable optical code division multiple access (OCDMA) encoder-decoder, with multiple tunable phase shifts, that we will show in Chapter 5. For their design and application, it is essential to know two features of the grating. One is the relationship between the applied electrical current on the wire and the resultant phase-shift, and the other is the spatial dc refractive index profile under the applied current. In the following sections, we will use the EAM-FROG technique to characterize the thermally induced phase-shift distribution in FBGs.

3.4.2 Experimental results using a 20-ps pulse train

To characterize the FBG with a tunable phase-shift, we fabricated a 17mm-long uniform grating in a standard single mode fibre, and a 18μm diameter tungsten wire was placed in direct contact with the grating, 8mm from one end, as shown in Fig.3.6. The Bragg wavelength, ac effective index modulation, peak reflectivity and FWHM of the FBG are respectively 1548nm, $3.3\text{x}10^{-5}$, 66% and 0.1nm. By experimentally observing the shift of the dip wavelength in the reflection spectrum of the grating, we measure the amount of thermally-induced phase-shifts under different electrical currents [153]. In this configuration, to achieve a phase-shift of 0.5π, 1.0π and 1.5π, the required electrical currents applied on the tungsten wire are respectively 52mA, 70mA and 84mA.

Having known the amount of the phase-shifts induced by the electrical currents, we use the pulse response method, based on the EAM-FROG technique, to characterize the spatial dc refractive index profile corresponding to the phase-shifts. The setup is the same as Fig. 3.2 in Section 3.2.3. The input optical pulse train, composed of 20-ps pulses at a repetition rate of 2.5GHz, is produced by passing a tunable semiconductor laser through an electro-optic modulator (EOM).

Using the EAM-FROG technique, the intensities and phases of reflected pulses from the FBGs are measured, when the applied electrical currents are respectively 0mA, 52mA, 70mA and 84mA, and the results are shown in Fig.3.7. We can see that the measured temporal phase-shifts are respectively 0, ~0.5π, ~π and ~1.5π at these different electrical currents. This is consistent with the results obtained by observing the reflection spectrum of the grating.

The corresponding dc refractive index profiles under these electrical currents are calculated, using Eq. (3.7), and the results are plotted in Fig.3.8. When the electrical current along the wire is 0mA, there is a small background refractive index profile on the uniform FBG. This might be from the non-uniformity in the fibre core [128]. When the electrical current is 70mA, the FWHM (full-width at half-maximum) of the dc spatial refractive index distribution is ~4.2mm.

Shown in Fig. 3.9 are the measured and calculated reflection spectra of the grating when the electrical current along the tungsten wire is respectively 0mA and 70mA. The calculated results are based on the retrieved dc refractive index distribution shown in Fig. 3.8.

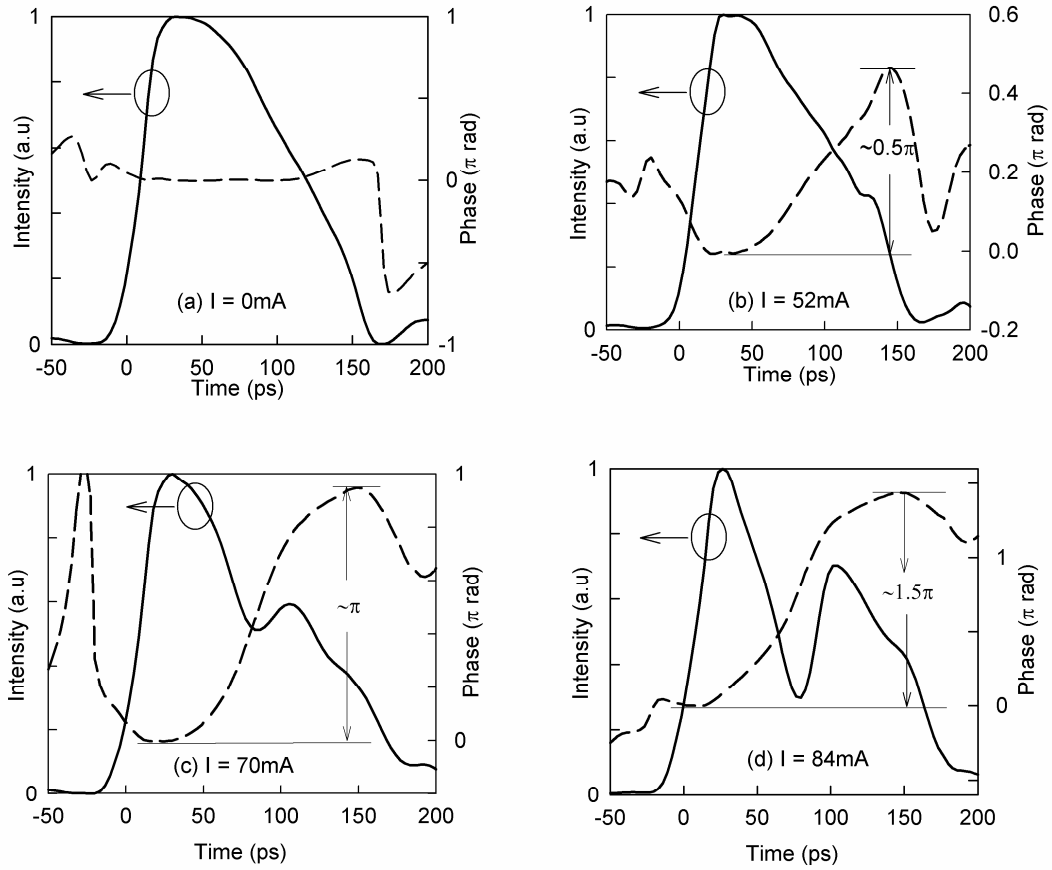

Fig.3.7 Measured intensity (solid line) and phase (dashed line) of the reflected pulses from the FBG when the electrical currents along the tungsten wire are respectively (a) 0mA, (b) 52mA, (c) 70mA, and (d) 84mA.

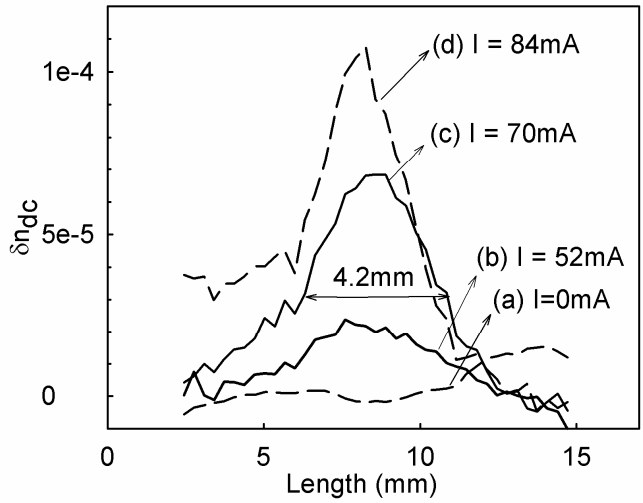

Fig.3.8 Retrieved spatial refractive index distributions when the electrical current along the tungsten wire is (a) 0mA. (b) 52mA, (c) 70mA, or (d) 84mA.

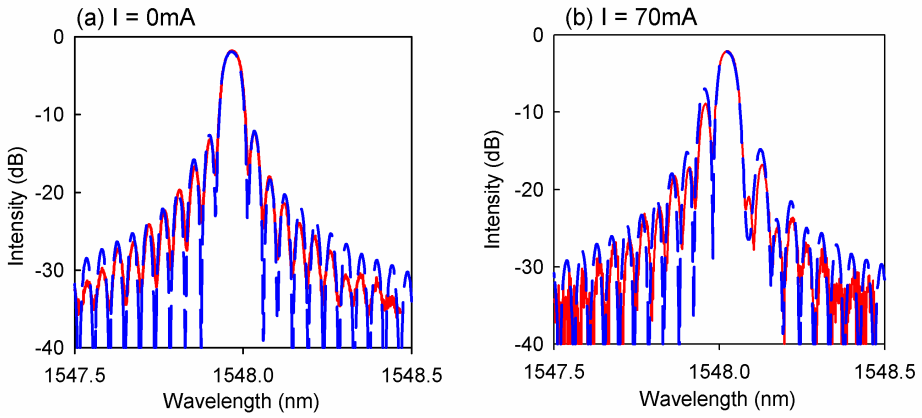

Fig.3.9 Measured (solid lines) and calculated (dashed lines) reflection spectra of the FBG when the applied electrical current is respectively 0mA and 70mA

A numerical simulation is shown in Fig.3.10 to assess the accuracy of the experimentally retrieved results, which are affected by our practical choice of the input pulse and grating strength. In this simulation, we utilize the grating and input pulse having the same parameters as in the experiments. A 17-mm long grating, with a uniform ac index modulation of $3.3\text{x}10^{-5}$ and peak reflectivity of 66%, has a spatial phase-shift of π, consisting of a dc refractive index profile, as shown in Fig.3.10(a), which is similar to the measured result of the 70mA-wire-current case in the experiment. Then, a 20-ps optical pulse is reflected from the FBG. The temporal intensity and phase of the reflected pulse are calculated and shown in Fig.3.10(c). The temporal phase is differentiated and then, using Eq. (3.7), the dc refractive index profile of the FBG is theoretically retrieved and is shown in the solid line of Fig. 3.10(d).

The deviation between the assumed and theoretically recovered results of phase-shift and dc refractive index profile can be explained in the following argument. Firstly, there is a deviation between the assumed spatial phase shift of π and the retrieved temporal phase shift of 0.93π. This deviation is caused by the relatively high peak reflectivity, of 66%, of the grating. Secondly, as shown in Fig. 3.10(d), the spatial refractive index distribution is slightly smeared near its maximum, which is due to the spatial resolution limitation imposed by the input pulse width of 20-ps. Thirdly, there is an obvious discrepancy of the refractive index profile at the rear part of the grating. This is caused by the high peak reflectivity of the grating, because less light can propagate to the rear part of the grating. This kind of simulation can give us a useful tool to analyze the accuracy of the practical experiments.

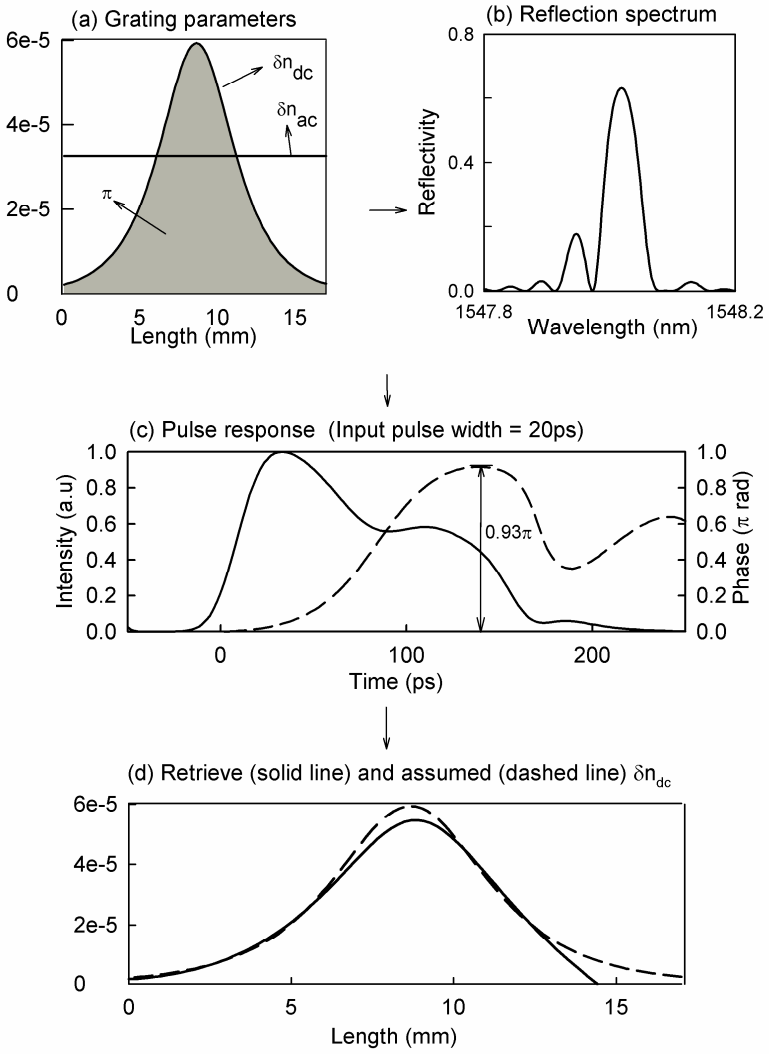

Fig.3.10 (a) Assumed dc and ac refractive index distribution of an FBG with a π phase shift, (b) its reflection spectrum, (c) intensity and phase of the reflected pulse from the grating (input pulse width =20ps), (d) Retrieved (solid line) and assumed (dotted line) dc refractive index variation.

3.4.3 Experimental results using a 5-ps pulse train

The spatial resolution of the dc refractive index profile is limited by the input pulse width used in the characterization. In the measurement in Section 3.4.2, the input pulse width is 20-ps, so the spatial resolution is ~2mm. Here, a 5-ps pulse train is used.

A 40mm long uniform grating was fabricated on a standard single mode fibre, and a 18μm diameter tungsten wire was placed in direct contact with the grating, 10mm from one end, as shown in Fig.3.6. The uniform grating, with a Bragg wavelength of 1550nm and an index modulation of 2.2×10^{-5}, has a peak reflectivity of 90%. However, because the tungsten wire is put near the front of the grating, the grating strength will not have an obvious affect on the characterization.

We use a similar setup to Fig.3.2 to characterize the spatial dc refractive index profile induced by different electrical currents. The input optical pulse train is composed of 5-ps pulses at a repetition rate of 1.25GHz from a gain-switched laser diode.

The intensities and phases of reflected pulses from the FBGs are measured, and shown in Fig.3.11, when the electrical currents applied on the tungsten wire are respectively 0mA, 52mA, 70mA and 84mA (corresponding to a phase-shift of 0, 0.5π, π, or 1.5π respectively). The corresponding effective dc refractive index profiles under these electrical currents are calculated, using Equation (3.7), and the results are plotted in Fig.3.12. When the electric current is 70mA (corresponding to a phase-shift of π), the FWHM of the spatial refractive index distribution is ~2.7mm.

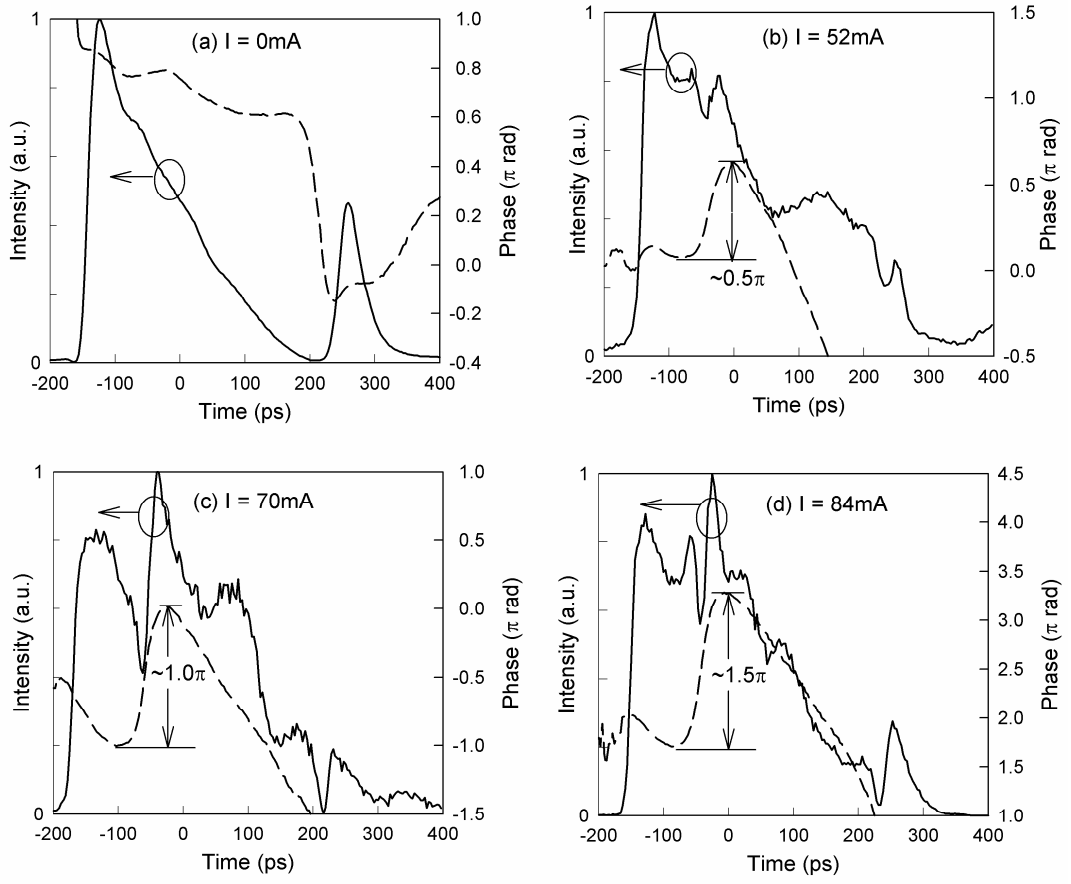

Fig.3.11 The measured intensities (solid lines) and phases (dashed lines) of the reflected pulses from the FBG when the electrical currents along the tungsten wire are respectively (a) 0mA, (b) 52mA, (c) 70mA, and (d) 84mA.

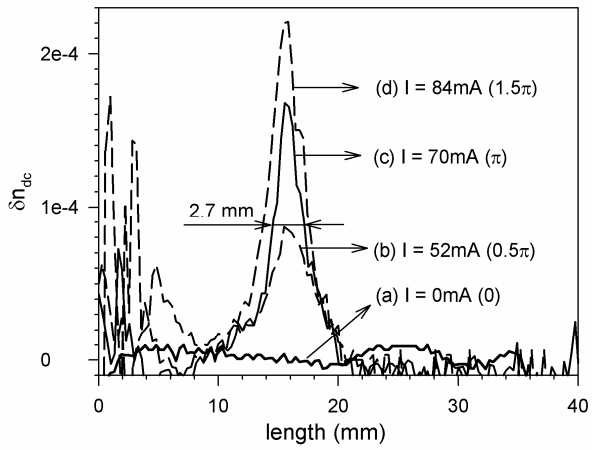

Fig.3.12 Retrieved spatial refractive index distributions when the electrical currents along the tungsten wire are (a) 0mA, (b) 52mA, (c) 70mA, and (d) 84mA.

3.4.4 Discussions

Spatial resolution of the above characterization is limited by the input pulse width. Therefore, a shorter input pulse is obviously a desirable choice. But obtaining very short optical pulses usually involves complicated techniques. In the experiments, we obtain the dc refractive index profile directly from the measured temporal phase of optical pulses without using its intensity. Theoretically, if we also know full information (intensity and phase) of the input pulses, it would be possible to obtain impulse responses of FBGs by the de-convolution techniques, and then the requirement for a short input pulse could surely be relaxed. But due to the noise in experimental data, this is quite difficult in practice. In the practical experiment, a reasonable tradeoff is to make sure that the bandwidth of input pulses is no narrower than the bandwidth of the gratings to be characterized.

As shown in section 3.4.2, the strength of the grating will also largely affect the measurement accuracy. As the strength of the grating increases, the equivalence of the amplitude of spatial phase shift and temporal phase shift will break gradually, so does the proportional relationship between the spatial refractive index distribution of the grating and the temporal phase differentiation of its pulse response. In theory, the grating parameters of strong gratings can possibly be retrieved through the inverse scattering technique [42]. But this is also very complicated, because it involves complex calculations, and the noise in the experimental data can affect the retrieved grating parameters seriously and un-expectedly [42].

3.5 Conclusions

We propose a pulse response method to directly characterize the spatial phase of the complex coupling coefficient, including the dc refractive index distribution (distributed phase shift), discrete phase, and chirp of fibre Bragg gratings. This method is based on the observation that the spatial phase of an FBG is directly related to the temporal phase of its pulse response. Therefore, the phase of the spatial index modulation can be characterized directly by measuring temporal phase of the pulse response of FBGs. Its main advantage is that the dc refractive index distribution only depends locally on the temporal phase of its pulse response.

Using this method, we have characterized the spatial phase profile of FBGs with a discrete phase-shift or a current-induced distributed phase-shift. In Chapter 5, using this technique, we will characterize a thermally induced dc refractive index distribution when tungsten wires with different diameters are used. These results are fundamental for our understanding of reconfigurable-phase OCDMA encoder-decoders.

Chapter 4

OCDMA systems based on super-structured fibre Bragg gratings

4.1 Introduction

OCDMA is a broadband access network technique, which combines the advantages of optical fibre communication and access networks. It also has the unique features of all optical processing in the encoding-decoding operation, full asynchronous access without complex protocols, low access delay, and potentially excellent system security [129-130].

In the CDMA systems, the same time slot and the same wavelength bandwidth are shared by many users, and different users are designated by a specific address codes. CDMA techniques fall into four categories: direct sequence (DS), frequency encoding (FE), frequency hopping (FH), and time hopping (TH) [131]. In DS-CDMA, each data bit is broadened into a series of pulses defined by a code sequence in the time domain. By contrast, in FE-CDMA, the code sequence is directly imprinted in the frequency spectrum of the input signal. In FH-CDMA, the coding is done in two dimensions: time and frequency. Each bit interval is subdivided in time (into chip intervals) and a certain frequency is transmitted during each chip. In TH-CDMA, a time interval is subdivided into a number of time slots. The coded information symbols are transmitted in a pseudo-randomly selected time slot as a block of one or more code words.

The former three CDMA techniques have already been demonstrated in the optical domain [132]-[140]. In optical DS-CDMA, a short light pulse is used as the input source, and various optical time delay lines, such as optical fibre delay lines [132] and planar lightwave circuit (PLC) delay lines [133], are the fundamental devices to achieve encoding and decoding in the time domain. In optical FE-CDMA, incoherent broadband sources such as LEDs, or coherent ultra-short pulses are used as the input source, and

usually a pair of bulk gratings plus an optical phase modulator array are used to achieve frequency encoding [134]-[136]. In optical FH-CDMA, broadband ASE sources or ultra-short pulses are used as the input source, and usually a series of FBGs with different central wavelengths are used as encoder and decoder, achieving frequency hopping [137]-[140].

A group in *Southampton University* proposed and demonstrated the use of SSFBGs as OCDMA encoder-decoders [6] [141]. An SSFBG is defined as a standard fibre grating, i.e., with a rapidly varying refractive index modulation of uniform amplitude and pitch, onto which an additional, slowly varying refractive index profile are imposed along its length. Due to the space-to-time conversion relation, an SSFBG with low overall reflectivity has an impulse response following its spatial superstructure. Therefore, when a short optical pulse (or a signal bit) is reflected from an SSFBG, with a superstructure profile designed according to a particular code sequence, the reflected pulse will be spread out in the time domain, following the superstructure profile of the SSFBG. This process is called encoding in OCDMA, and the SSFBG functions as an OCDMA encoder. If the encoding pulse is then reflected from a physically reversed grating, the information bit can be recovered or decoded due to the matched filtering. This process is called the decoding, and the decoding grating is called the OCDMA decoder.

Compared with OCDMA techniques, which utilize optical fibre delay lines, planar lightwave circuit (PLC) delay lines, FBG series, or bulk gratings as the encoding and decoding elements, OCDMA based on the SSFBG technique has the advantage of simplicity (one grating is enough for encoding or decoding), small size, tunability, polarization insensitivity, and the potential for easy fabrication. The most important advantage of SSFBGs is that the optical phase of light reflected from the SSFBG can be exploited, allowing the use of optical phase as a coding parameter. Phase coding is important since it exhibits far better crosscorrelation characteristics than amplitude only coding [6] [133], which in turn allows lower inter-channel interference, and thus more simultaneous users for a given code length than amplitude only coding.

SSFBG OCDMA systems with different grating strength, input pulse width, code number and chip length have been successfully demonstrated in a number of experiments [6] [142-150]. Despite this, there are no detailed discussions on how the various grating parameters affect the system performances. In this chapter, a detailed analysis on the system principle is given, from the viewpoint of FBG, and based on this we will analyze how the SSFBG parameters separately, or working together, affect the OCDMA system

performances.

This Chapter is organized as follows. In Section 4.2, the impulse responses of the SSFBGs are directly given from the space-to-time conversion, and their frequency responses by the Fourier transform. Then, we derive the autocorrelation condition: phase matching condition, and the crosscorrelation condition of the SSFBG OCDMA system. The conclusion is that, in the weak grating approximation, the phase matching condition between the SSFBG encoder and its matching decoder is satisfied automatically, while the crosscorrelation characteristics, as expected, are largely dependent on the choice of the code sequences.

In Section 4.3, we use the transfer matrix theory and Fourier transform technique to numerically calculate the frequency and pulse responses of the SSFBG encoders and decoders. We clearly show that the code sequences are encoded into the temporal phases of their pulse responses, which have recently been directly measured by us in experiments [126]. Then the autocorrelation and crosscorrelation pulses, their corresponding spectral intensities, and especially spectral phases are presented, emphasizing the autocorrelation and crosscorrelation conditions.

In Section 4.4, the effects of various parameters of SSFBG encoders and decoders on the OCDMA system performances are analyzed. First of all, we show the system performance deterioration with the increase of the grating strength, and explain this by showing that the increase of the grating strength breaks the phase matching condition gradually. Secondly, by means of an example, we analyze how the input pulse width affects the autocorrelation pulse width and system performances, emphasizing that the relative bandwidth of the input pulse and the encoding-decoding gratings are critical to the final performance. Thirdly, the tolerance of the central wavelength offset between the encoding and decoding SSFBGs is evaluated. Fourthly, we analyze the effect of different chip duration, and conclude that the chip duration will have no obvious effects on the final system performance under particular conditions, but it is still an important parameter because it will affect the choice of the input pulse width, the highest chip bit rate, device size, time slot allocation and wavelength spacing. Finally, we analyze the effects of the chip number on the system performance, and conclude that a larger chip number can accommodate more users and improve the system performance significantly because of the improved spectral phase characteristics provided by the longer phase series.

The conclusions for this chapter are summarized in Section 4.5.

4.2 Principles: a general description

4.2.1 Structure, impulse and frequency responses of SSFBG en/decoders

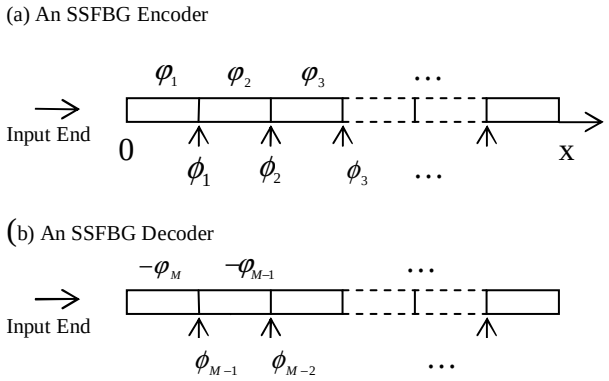

Fig.4.1 Structures of (a) an SSFBG encoder and (b) the matching decoder.

The structures of an SSFBG OCDMA encoder, and its matching decoder, are shown in Fig.4.1. A series of M–1 discrete phase shifts, $\phi_1, \phi_2, \ldots, \phi_{M-1}$, are imposed uniformly on a uniform grating with a length of L, and divides the grating into M chips. The spatial phases of the resultant SSFBG are consecutively $\varphi_1, \varphi_2, \cdots \varphi_M$. The spatial superstructure profile of the SSFBG encoder, shown in Fig.4.1 (a), is,

$$S(x) = \sum_{m=1}^{M} \exp(i\varphi_m) \cdot rect\left[\frac{x - \left(m - \frac{1}{2}\right) \cdot \frac{L}{M}}{\frac{L}{M}}\right] \tag{4.1}$$

where, *rect*[] is the rectangular function.

The matching decoder to an encoder is its spatially reversed grating. Its spatial superstructure profile is,

$$S^{I}(x) = \sum_{m=1}^{M} \exp[i(-\varphi_m)] \cdot rect\left[\frac{x - (M - m + 1 - 1/2) \cdot \frac{L}{M}}{\frac{L}{M}}\right] \tag{4.2}$$

In the weak SSFBG limit, i.e., where the peak reflectivity of the grating is low, so that the light penetrates the full grating length, and the individual elements of the grating contribute equally to the reflected response, the impulse response of the SSFBG can be directly obtained from the refractive index superstructure profile. The impulse response of the SSFBG encoder described by Eq. (4.1) is,

$$h(t)=\sum_{m=1}^{M}\exp(i\varphi_m)\cdot rect\left[\frac{t-(m-1/2)\cdot\Delta t}{\Delta t}\right] \tag{4.3}$$

where

$$\Delta t=\frac{2n}{c}\cdot\frac{L}{M} \tag{4.4}$$

is called the chip duration, n is the background refractive index of FBGs, and c is the light speed in vacuum. Its frequency response is the Fourier transform of the impulse response,

$$H(\omega)=\frac{1}{2\pi}\int_{-\infty}^{+\infty}h(t)\exp(i\omega t)dt=\frac{1-\exp(-i\omega\Delta t)}{i2\pi\omega}\sum_{m=1}^{M}\exp\left[i(\varphi_m+m\omega\Delta t)\right] \tag{4.5}$$

The central frequency of its frequency response is dependent on the Bragg wavelength of the SSFBG.

Similarly, the impulse and frequency responses of the decoder, described by Eq. (4.2), are respectively,

$$h^{I}(t)=\sum_{m=1}^{M}\exp\left[i(-\varphi_m)\right]\cdot rect\left[\frac{t-(M-m+1-1/2)\cdot\Delta t}{\Delta t}\right] \tag{4.6}$$

$$H^{I}(\omega)=\frac{1-\exp(i\omega\Delta t)}{-i2\pi\omega}\cdot\exp(i\omega M\Delta t)\cdot\sum_{m=1}^{M}\exp\left[i(-\varphi_m-m\omega\Delta t)\right] \tag{4.7}$$

4.2.2 Encoding, decoding, autocorrelation and crosscorrelation

In the SSFBG OCDMA system, the encoding process can be described as the response of the encoder to the input signal. An input signal is reflected from the encoder, and the spectrum of the reflected pulse, i.e., the encoding pulse, $Y(\omega)$, is given by the product of the spectrum of the input pulse $X(\omega)$ and the frequency response of the encoding grating $H(\omega)$,

$$Y(\omega)=X(\omega)H(\omega) \tag{4.8}$$

In the temporal domain, the reflected pulse $y(t)$ is given by the convolution between the input pulse $x(t)$ and the impulse response of the grating $h(t)$,

$$y(t)=x(t)\otimes h(t) \tag{4.9}$$

where, $\otimes$ denotes convolution, and $y(t)$, $x(t)$ and $h(t)$ are respectively the inverse Fourier transform of $Y(\omega)$, $X(\omega)$ and $H(\omega)$ in Eq.(4.8).

Similarly, the decoding process can be described as the response of the decoder. The pulse reflected from the encoder is reflected from the decoder, and the resultant decoding

pulse $Z(\omega)$ is given by the product of the spectrum of the pulse reflected from the encoder $Y(\omega)$, and the frequency response of the decoding grating $G(\omega)$:

$$Z(\omega) = Y(\omega)G(\omega) = X(\omega)H(\omega)G(\omega) \tag{4.10}$$

This process can also be described in the time domain by convolution.

In an OCDMA system, many users share one transmission channel. A 2x2 OCDMA network is shown in Fig.4.2 as an example. It is composed of two SSFBG OCDMA encoders, A and B, with the frequency response of $H_A(\omega)$ and $H_B(\omega)$ respectively, the corresponding OCDMA decoders, A and B, with the frequency response of $G_A(\omega)$ and $G_B(\omega)$, and two 2x1 optical couplers. The encoder A and decoder A are the matched OCDMA encoder-decoder pair, and so are the encoder B and decoder B.

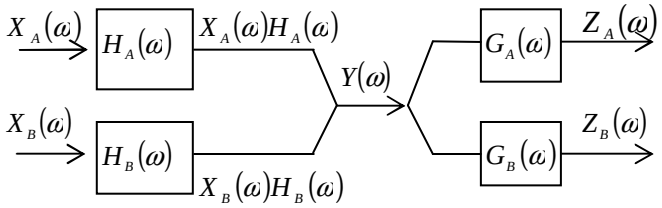

Fig.4.2 A 2x2 OCDMA network.

As shown in Fig.4.2, two input optical signals, $X_A(\omega)$ and $X_B(\omega)$, are encoded by the OCDMA encoder A and B respectively, resulting in the encoded signals $X_A(\omega)H_A(\omega)$ and $X_B(\omega)H_B(\omega)$. The two encoded signals are combined by the 1x2 optical coupler, producing

$$Y(\omega) = X_A(\omega)H_A(\omega) + X_B(\omega)H_B(\omega) \tag{4.11}$$

After transmitting along the fibre, the signal $Y(\omega)$ is then split by the 2x1 optical coupler, and decoded by the OCDMA decoders A and B respectively. Neglecting the transmission effects of the fibre, the signal following the decoder A is

$$Z_A(\omega) = Y(\omega)G_A(\omega) = Z_{AA}(\omega) + Z_{AB}(\omega) \tag{4.12}$$

where

$$Z_{AA}(\omega) = X_A(\omega)H_A(\omega)G_A(\omega) = \alpha_{AA}(\omega)X_A(\omega)\exp[i\Phi_{AA}(\omega)] \tag{4.13}$$

$$\alpha_{AA}(\omega) = |H_A(\omega)| \cdot |G_A(\omega)| \tag{4.14}$$

$$\Phi_{AA}(\omega) = \arg[H_A(\omega)] + \arg[G_A(\omega)] \tag{4.15}$$

$$Z_{AB}(\omega) = X_B(\omega)H_B(\omega)G_A(\omega) = \alpha_{AB}(\omega)X_B(\omega)\exp[i\Phi_{AB}(\omega)] \tag{4.16}$$

$$\alpha_{AB}(\omega) = |H_B(\omega)| \cdot |G_A(\omega)| \tag{4.17}$$

$$\Phi_{AB}(\omega) = \arg[H_B(\omega)] + \arg[G_A(\omega)] \tag{4.18}$$

$Z_{AA}(\omega)$ is the autocorrelation spectrum. $H_A(\omega)G_A(\omega)$ is the autocorrelation factor, and $\alpha_{AA}(\omega)$ and $\Phi_{AA}(\omega)$ are respectively its amplitude and phase. Conversely, $Z_{AB}(\omega)$ is the crosscorrelation spectrum. $H_B(\omega)G_A(\omega)$ is the crosscorrelation factor, and $\alpha_{AB}(\omega)$ and $\Phi_{AB}(\omega)$ are respectively its amplitude and phase.

Suppose the phase series of two SSFBG encoders, A and B, are respectively $(\varphi_1^A, \varphi_2^A, \ldots, \varphi_M^A)$ and $(\varphi_1^B, \varphi_2^B, \ldots, \varphi_M^B)$. The frequency responses of the encoders and decoders can be obtained using Eqs. (4.5) and (4.7).

The autocorrelation factor of encoder A and decoder A is:

$$H_A(\omega)G_A(\omega) = \alpha_{AA}(\omega)\exp[i\Phi_{AA}(\omega)] \tag{4.19}$$

$$\alpha_{AA}(\omega) = \frac{1-\cos(\omega\Delta t)}{2\pi^2\omega^2}\cdot\left|\sum_{m=1}^{M}\exp\left[i\left(\varphi_m^A + m\omega\Delta t\right)\right]\right|^2 \tag{4.20}$$

$$\Phi_{AA}(\omega) = \omega M\Delta t \tag{4.21}$$

On the other hand, the cross-correlation factor of encoder B and decoder A is:

$$H_B(\omega)G_A(\omega) = \alpha_{AB}(\omega)\exp[i\Phi_{AB}(\omega)] \tag{4.22}$$

$$\alpha_{AB}(\omega) = \frac{1-\cos(\omega\Delta t)}{2\pi^2\omega^2}\cdot\left|\left(\sum_{m=1}^{M}\exp\left[i\left(\varphi_m^B + m\omega\Delta t\right)\right]\right)\cdot\left(\sum_{m=1}^{M}\exp\left[i\left(-\varphi_m^A - m\omega\Delta t\right)\right]\right)\right| \tag{4.23}$$

$$\Phi_{AB}(\omega) = \omega M\Delta t + \arg\left(\sum_{m=1}^{M}\exp\left[i\left(\varphi_m^B + m\omega\Delta t\right)\right]\right) + \arg\left(\sum_{m=1}^{M}\exp\left[i\left(-\varphi_m^A - m\omega\Delta t\right)\right]\right) \tag{4.24}$$

In an OCDMA system, the signal following each decoder is the combination of an autocorrelation and many crosscorrelation signals. From the viewpoint of communication, the autocorrelation signal is the desired signal, whereas the crosscorrelation is the interference, or noise to the autocorrelation. The objective of communication is to obtain a large signal-to-noise-ratio (SNR), i.e. to obtain autocorrelation with a high peak intensity and crosscorrelation with a low peak intensity.

Eq. (4.21) is called the phase matching condition, which shows that the phase of the autocorrelation factor is a linear function of frequency, implying that all the frequency components of the input signal experience the same time delay after the decoding process, and constitute a short pulse with high peak intensity. It is noteworthy that all physically reversed FBG pairs satisfy the phase matching condition if the weak grating approximation is satisfied. While for practical SSFBGs, this condition is only nearly satisfied due to the breaking of the weak grating approximation. Eq. (4.19) shows that the autocorrelation pulse spectrum is an amplitude-modulation of the input pulse spectrum. The amplitude modulation might narrow the bandwidth of the autocorrelation spectrum

and reshape the input pulse. This will therefore slightly decrease the peak intensity of the autocorrelation pulse. However, its effect is not very serious.

According to Eq.(4-24), $\Phi_{AB}(\omega)$ *is a nonlinear function to frequency* ω, which means that different spectral components of $Z_{AB}(\omega)$ will experience different time delays, and the cross-correlation signal is distributed over a long time duration so that its peak intensity is far lower than the autocorrelation signal. The extent of the nonlinearity in the phase $\Phi_{AB}(\omega)$ is not easy to measure, but it is crucial to suppress the peak intensity of the cross-correlation pulse. $\Phi_{AB}(\omega)$ is directly related to the phase series of the encoder-decoder. So, it is very important to choose a phase series which produces a good cross-correlation performance, so as to obtain high-contrast code recognition.

The code sequences suitable for the radio frequency CDMA to achieve good autocorrelation and cross-correlation performance are also applicable to OCDMA systems. The well-known *M*-sequences [151], and the quaternary coding sequence, such as the family *A* sequences [152], have been broadly utilized in the OCDMA system. In the following sections, our numerical examples are based on family *A* sequences.

4.3 Principles: a numerical example

The numerical simulation is based on the calculation of the reflection spectral responses of the SSFBG encoder-decoders. Firstly, two SSFBG encoder-decoder pairs are chosen, and their reflection spectral responses are obtained through the transfer matrix model. Secondly, a short optical pulse is reflected from the encoder, and the reflected pulse, i.e. the encoded pulse, is calculated through the inverse Fourier transform of the product of the input pulse spectrum, and the spectral response of the encoder. Finally, the decoding pulses, i.e., the autocorrelation and crosscorrelation pulses, are similarly obtained through the inverse Fourier transform of the product of the input pulse spectrum, the spectral response of the encoder, and that of the decoder.

4.3.1 SSFBG encoder-decoders

Two 15-chip, four-phase-level sequences Q1 = [1.5π 0.0π 0.0π 0.5π 1.0π 0.0π 0.0π 1.5π 0.5π 1.5π 0.5π 0.0π 0.5π 1.0π 1.5π], and Q2 =[1.5π 0.5π 1.0π 1.5π 0.0π 0.5π 1.5π

1.0π 0.0π 1.5π 0.0π 0.0π 0.0π 0.5π 0.5π], from the family *A*-sequences [21], are chosen as address codes of the OCDMA encoders. Phase distributions of Q1, Q2, Q1* and Q2* are shown in Fig. 4.3.

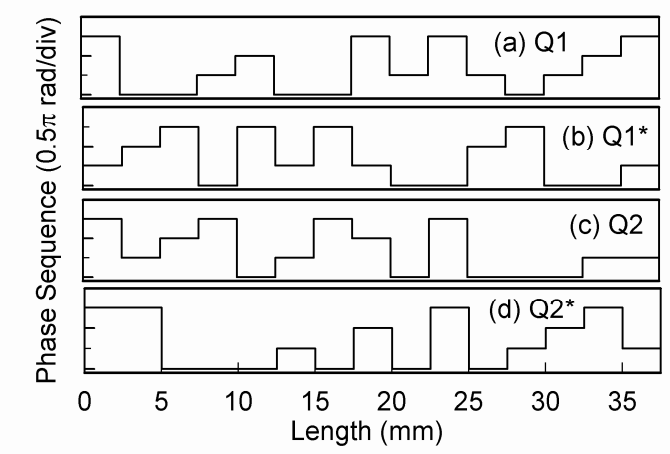

Fig.4.3 Phase distributions of the SSFBGs Q1, Q1*,Q2 and Q2*.

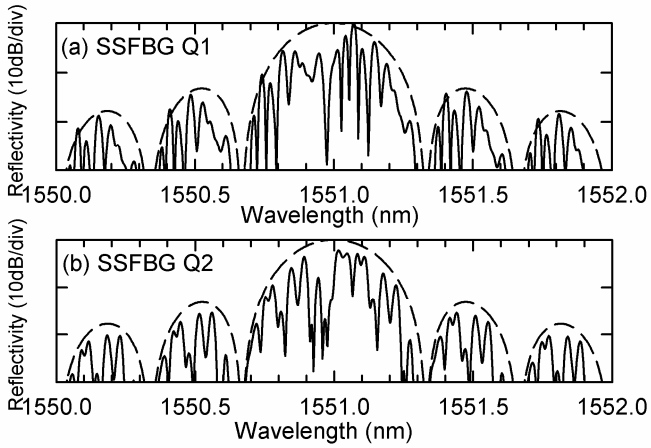

Fig.4.4 Solid lines: reflection spectra of the SSFBGs Q1 and Q2, dashed lines: reflection spectrum of the single-chip grating.

Parameters of the SSFBG en/decoders are as follows. The total length is 37.5mm, composed of 15 chips, each with a chip-length of 2.5mm. The Bragg wavelength of all the SSFBGs is 1551nm, and the refractive index modulation is 1.3×10^{-5}, resulting in a peak reflectivity of ~20%. The effective index of the host fibre of the SSFBGs is assumed to be 1.452.

Theoretical power reflection spectra of the SSFBGs Q1 and Q2 are plotted in the solid lines of Fig. 4.4. The reflection spectra of their matching decoders are not shown here, because they have similar profiles to their corresponding encoders. Also shown in the dashed lines of Fig. 4.4, are the theoretical power reflection spectra of the single-chip

grating, i.e., the 2.5mm uniform grating with the same strength and Bragg wavelength as the SSFBGs. The reflection spectrum of the single-chip grating constitutes the envelope to that of an SSFBG that is composed of a series of chips. This implies that the overall bandwidth of an SSFBG is dependent on its single chip length.

Through the Fourier transform technique, the reflection spectra of the SSFBGs have been analytically derived in Eq. (4.5). The square of (4.5) is,

$$|H(\omega)|^2 = \frac{1}{\pi^2\omega^2}\sin^2\left(\frac{\omega\Delta t}{2}\right)\cdot\left|\sum_{m=1}^{M}\exp\left[i(\varphi_m + m\,\omega\Delta t)\right]\right|^2 \tag{4.25}$$

Assuming $\varphi_1 = \varphi_2 = \cdots = \varphi_M$, (4.25) becomes,

$$|H(\omega)|^2 = \frac{1}{\pi^2\omega^2}\sin^2\left(\frac{\omega M\Delta t}{2}\right) \tag{4.26}$$

From Eq. (4.25), the envelope period of the reflection spectra is $\lambda^2/(c\Delta t)$. Similarly, from Eq. (4.26), the period of minute structures in the reflection spectra is $2\lambda^2/(cM\Delta t)$.

In the above example, the chip duration $\Delta t \approx 24.2\,ps$, so the envelope period of the reflection spectra is $\lambda^2/(c\Delta t) \approx 0.32nm$, and the period of the minute structures in the reflection spectra is $2\lambda^2/(cM\Delta t) \approx 0.04nm$.

4.3.2 Encoding pulses

A transform-limited Gaussian pulse, with a 2ps FWHM (full-width at half-maximum), is reflected respectively from SSFBGs Q1, Q2, Q1* and Q2*, and the temporal intensities and phases, of the reflected pulses are shown in Fig.4.5. The total duration is ~363ps, equivalent to the roundtrip time of the 15-chip gratings. The temporal phases strictly follow spatial phases of the SSFBGs, that is, the address code sequences are encoded into the temporal phases of the reflected pulses, both in period and amplitude.

In this simulation, the peak reflectivity of the SSFBGs is ~20%, which means that all the elements of the grating contribute roughly equally to the reflected response. The input pulse width is 2ps, far shorter than the chip duration of 24.2ps, which makes the reflected pulse a good approximation to the impulse responses of the gratings.

In the following simulation, the 2ps transform-limited Gaussian pulse will be used as the input optical pulse of the OCDMA system, so the reflected pulses from the encoders, Q1 and Q2, are called the encoding pulses.

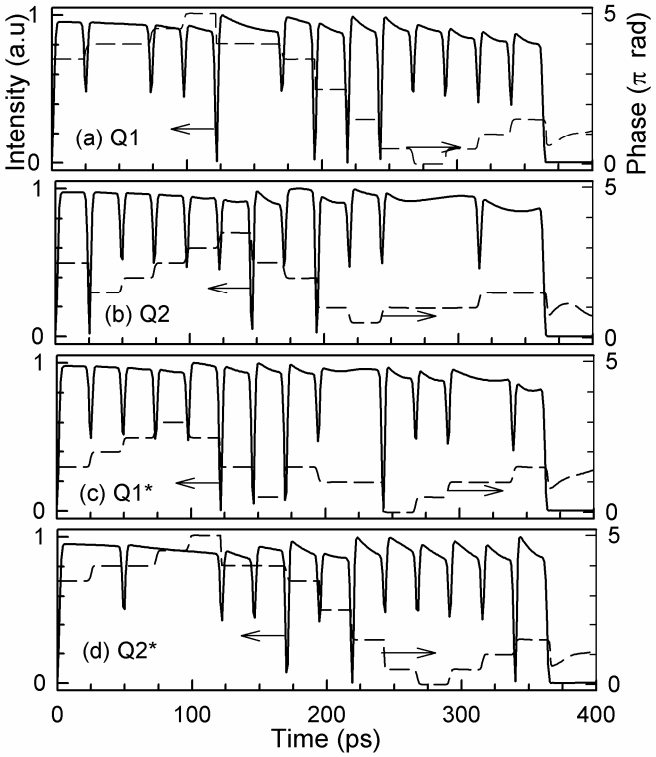

Fig.4.5 Intensities (solid line) and phases (dashed line) of reflected pulses from (a) Q1, (b) Q2, (c) Q1* and (d) Q2*.

4.3.3 Decoding pulses--autocorrelation and crosscorrelation

The autocorrelation Q1:Q1*, Q2:Q2*, and crosscorrelation Q1:Q2*, Q2:Q1* are shown in Fig.4.6. Note that the autocorrelation pulse is composed of a single dominant peak, and some low-level sidelobes, while the crosscorrelation pulse is composed of only low-level peaks. The features of the autocorrelation and crosscorrelation pulses can be explained in the frequency domain. Shown in Fig.4.7 are spectral intensities and phases of the autocorrelation and crosscorrelation pulses. The spectral phases corresponding to autocorrelation pulses, as shown in Fig.4.7 (a) and (d), are nearly linear, which suggests that the phases between the encoder and decoder are roughly conjugate and, consequently, most of the spectral components appear at roughly the same time, constituting the autocorrelation peak, as shown in Fig. 4.6 (a) and (d). On the other hand, the spectral phases corresponding to crosscorrelation pulses, as shown in Fig.4.7 (b) and (c), are nonlinear, which causes the optical power to distribute across a large time scale, as shown in Fig.4.6 (b) and (c).

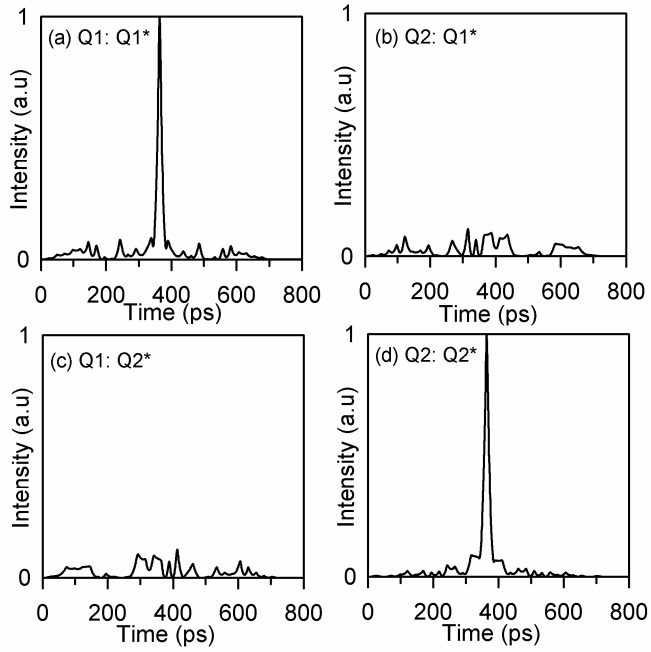

Fig.4.6 (a) Autocorrelation Q1:Q1*, (b)crosscorrelation Q1:Q2* (c) cross-correlation Q2:Q1* (d) autocorrelation Q2:Q2* (The input pulse width is 2ps).

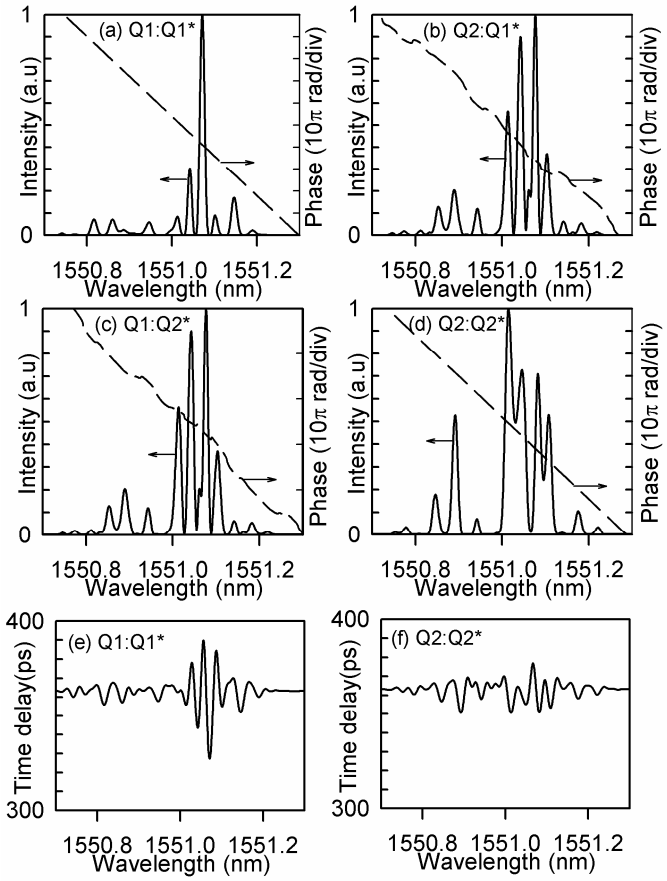

Fig.4.7 Spectral intensities (solid line) and phases (dotted line) corresponding to (a) autocorrelation Q1: Q1*, (b) cross-correlation Q1: Q2*, (c) crosscorrelation Q2: Q1*, (d) autocorrelation Q2: Q2*. Differentiation of the spectral phase with respect to frequency for autocorrelation (e) Q1: Q1* and (f) Q2: Q2*. (The input pulse width is 2ps).

To present the details of spectral phase characteristics, we differentiate spectral phases of the autocorrelation pulses, with respect to frequency, and obtain the spectral phase slope, which is in fact the time delay, $\tau = d\Phi/d\omega$, and the results are shown in Fig.4.7(e) and (f). We can see that the spectral phase slope is ~363ps, which is the time shift of autocorrelation pulses. The minor oscillation of time delay indicates that the spectral phases are not perfectly linear, which is due to the breaking of the weak grating approximation.

4.4 Discussions about the SSFBG OCDMA design

In this section, the effects of several parameters, such as the SSFBG strength, chip length, chip number, and the input pulse width, on the system performances, are analyzed. This analysis is essential for the design and evaluation of SSFBG OCDMA systems.

The objective of an OCDMA system is to obtain a high signal-to-noise-ratio (SNR), i.e. to obtain an autocorrelation pulse with high peak intensity and crosscorrelation pulses with low peak intensity. Here, for simplicity, the ratio between the peak of cross and auto correlation (RPCA) pulses is defined as the parameter to evaluate the OCDMA system performance. For an OCDMA system, a lower RPCA implies a higher SNR, and consequently a better system performance, and more possible simultaneous users.

4.4.1 SSFBG strength

As shown in section 4.2, Eq. (4.21) is automatically satisfied under the weak grating approximation. However, if the gratings are too weak, their insertion loss will be very high. Reducing the power loss of the SSFBG encoder-decoder is another key design objective. Therefore, to design a system with an acceptable final performance and less power loss, it is necessary to analyze how, and to what extent, the SSFBG strength affects the performance of OCDMA systems.

We still use the 15-chip, four-phase-level SSFBGs with a chip-length of 2.5mm as the encoder-decoder and 2ps transform-limited Gaussian pulses as the input pulses. The code sequence is chosen to be Q1, and Q2. But we change the effective index modulation of the SSFBGs so that peak reflectivity of the grating Q1 varies from 0.1% to 99.9%, while gratings Q1*, Q2 and Q2* always have the same refractive index modulation as Q1. The

resultant RPCA value between Q2: Q1* and Q1: Q1* with respect to the peak reflectivity of grating Q1 are plotted in Fig.4.8. It shows that RPCA increases gradually with the increase of peak reflectivity of the encoder-decoder. But it is noteworthy that the change of RPCA value is not obvious as the peak reflectivity of gratings increases from 0.1% to 50%.

In Fig.4.9, the autocorrelation Q1: Q1* (indicated by the solid lines) and crosscorrelation Q2: Q1* (indicated by the dashed lines) pulses are plotted as the peak reflectivity of Q1 varies. With the increase of the SSFBG strength, the sidelobe of autocorrelation gradually becomes prominent, decreasing the peak intensity of the autocorrelation pulse and, simultaneously, the peak intensity of the crosscorrelation pulse increases. Both of these situations will consequently cause a decrease of the RPCA value.

Differentiation of the spectral phase, corresponding to the autocorrelation pulses produced by SSFBGs with different peak reflectivity, is shown in Fig.4.10. As shown, the time delay oscillations increase with the increase of the grating strength, implying that the phase matching condition is gradually broken.

To decrease the insertion loss of SSFBG encoder-decoders, while maintaining the system performances, a suitable apodization or chirp can be applied to the SSFBGs. In Ref [146-147], an apodization technique was demonstrated experimentally.

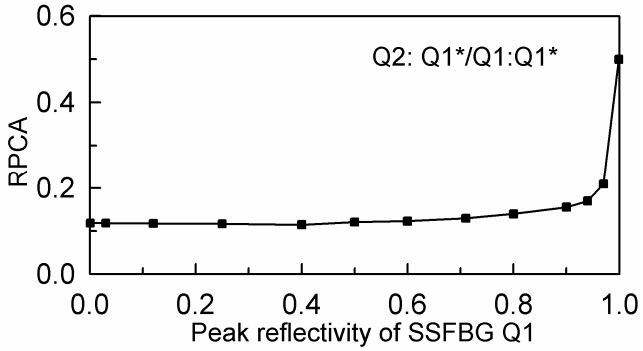

Fig.4.8 Relationship between peak reflectivity of SSFBG and RPCA of Q2: Q1*/Q1: Q1*.

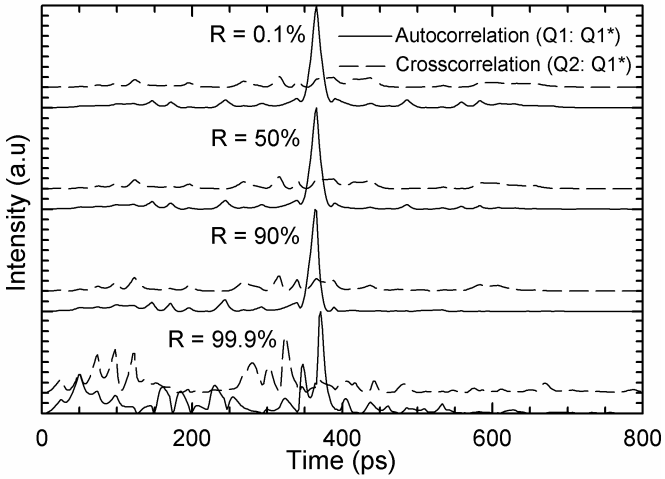

Fig.4.9 Correlation pulses when the peak reflectivity of the SSFBG varies.

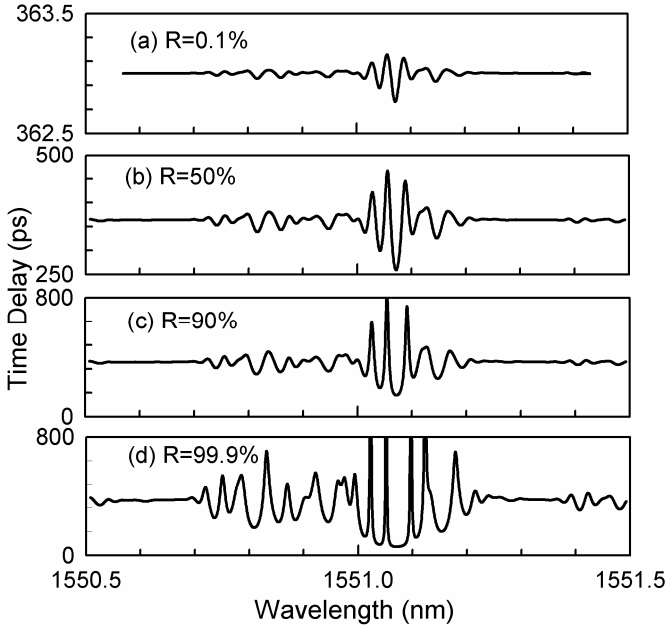

Fig.4.10 Time delay spectra of the autocorrelation pulse, when the peak reflectivity of the SSFBGs varies.

4.4.2 Input pulse widths

The choice of a suitable light source, especially the input pulse width, is critical for the OCDMA system design. Ideally, the input pulse width should be much shorter than the single chip duration of the encoder-decoder to meet the requirements of impulse response. In Ref [6] [9] [142-144], 2.5ps or 20ps short pulses were utilized in different system configurations. Ref. [145] provides systematic experimental results on the effects of different input pulse widths. Here, by numerical simulations, we analyze how the input pulse width affects the OCDMA systems.

We still use the 15-chip, four-phase-level SSFBGs, with a chip-length of 2.5mm, as examples. To satisfy the weak grating approximation, we select the refractive index modulation of the SSFBG so that their peak reflectivity is ~12%.

Then, transform-limited Gaussian pulses, with an FWHM of 2ps, 5ps, …, 100ps, are used as the input pulses, and by simulation, the FWHM of the autocorrelation pulse Q1: Q1* and RPCA of Q2: Q1* over Q1: Q1*, are obtained and shown in Fig.4.11. As the input pulse width increases, both the autocorrelation pulse width and the RPCA value increase nearly linearly. In Fig.4.12, we show autocorrelation pulses Q1: Q1*, and crosscorrelation pulses Q2: Q1*, under the input pulse width of 2ps, 25ps, and 100ps. With the increase of input pulse width, the resultant autocorrelation pulse is broadened, decreasing its peak intensity and, simultaneously, crosscorrelation pulses exhibit much higher peak intensity.

To illustrate this, the spectra of grating Q1, and input pulse with an FWHM of respectively 2ps, 25ps and 100ps are plotted in Fig.4.13. When the input pulse width is very short (for example, 2ps), its bandwidth is far broader than that of the SSFBG, so the spectral width of the autocorrelation pulse depends only on the bandwidth of the SSFBG and, as a result, the autocorrelation pulse width is kept constant to a particular value, which is decided by the bandwidth of SSFBGs. On the other hand, when the input pulse width is large (for example, 100ps), its spectral width is narrower than that of SSFBG. As a result, the spectral width of autocorrelation pulses will follow the bandwidth of the input pulse. Consequently, in the time domain, the autocorrelation pulse width will be nearly equivalent to the input pulse width.

In Fig. 4.14, we plot the spectral intensities and phases of the autocorrelation Q1: Q1* and crosscorrelation Q2: Q1*, when the input pulse width is 2ps and 100ps respectively. Note that, at different input pulse widths, the phase matching relation between Q1 and Q1* (comparing the spectral phases in Fig. 4.14 (a) and (b)) is invariant, and the phase mismatch between Q1 and Q2* (comparing the spectral phases in Fig.4.14(c) and (d)) does not change either.

Despite this, their spectral width will change under different input pulse widths. When the bandwidth of the input pulse is narrow (~0.05nm for the input pulse width of 100ps), the spectral width of the autocorrelation/crosscorrelation pulses is narrow. This narrow bandwidth results in a long autocorrelation pulse width. At the same time, this narrow bandwidth reduces the extent of phase mismatch and, as a result, the crosscorrelation pulse will have a relatively higher peak power.

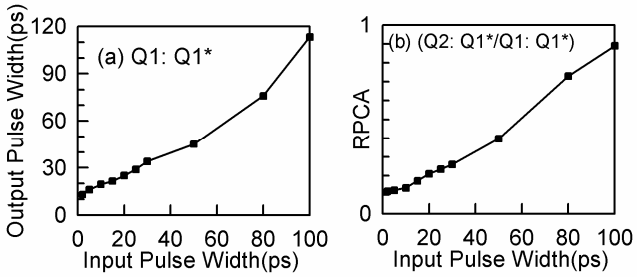

Fig.4.11 (a) The relation between the input pulse width and the output autocorrelation (Q1: Q1*) pulse width, (b) the relation between the input pulse width and the RPCA of Q2: Q1*/Q1: Q1*.

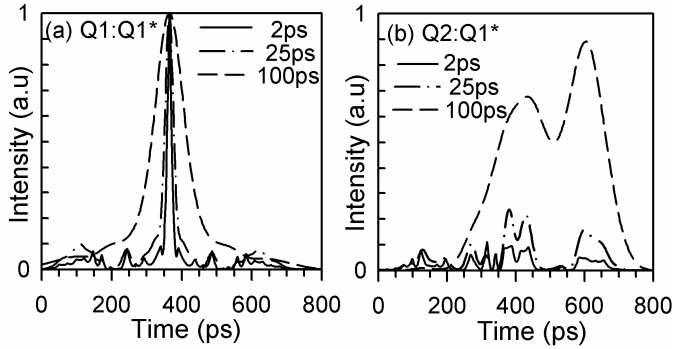

Fig.4.12 (a) Autocorrelation (Q1: Q1*) and (b) crosscorrelation (Q2:Q1*) pulses when the input pulse width is respectively 2ps, 25ps and 100ps.

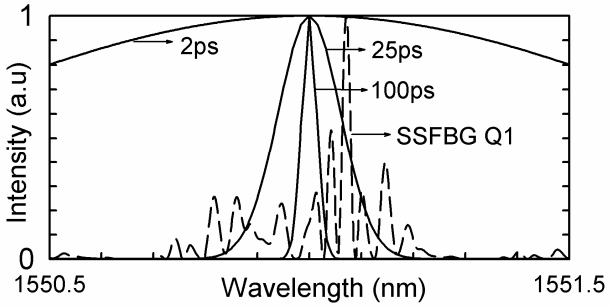

Fig.4.13 Power spectrum of SSFBG Q1, and the spectrum of the input pulse with an FWHM of 2ps, 25ps, and 100ps.

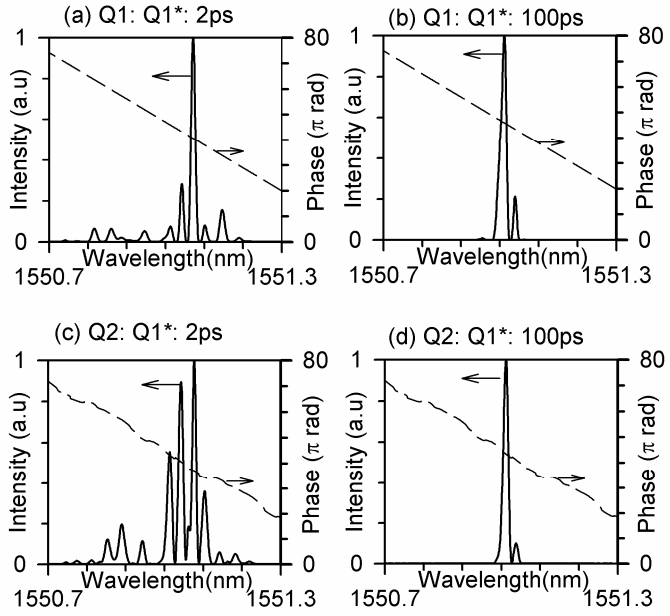

Fig.4.14 Spectral intensities (solid line) and phases (dashed line) corresponding to: (a)autocorrelation Q1: Q1* when the input pulse width is 2ps, (b)autocorrelation Q1:Q1*when the input pulse width is 100ps, (c)crosscorrelation Q2: Q1* when the input pulse width is 2ps, (d) crosscorrelation Q2: Q1* when the input pulse width is 100ps.

4.4.3 Tolerance of central wavelength offset between encoders and decoders

In above discussions, we assume that the central wavelength of the decoder is calibrated to that of the encoder. Here, by simulation, we evaluate the effect of the offset between the central wavelength of encoders and decoders. We use systems with three different configurations: (1) 15-chip codes with a chip length of 1.25mm, (2)15-chip codes with a chip length of 2.5mm, and (3) 31-chip codes with a chip length of 2.5mm. The total lengths of corresponding SSFBGs are respectively 18.75mm, 37.5mm, and 77.5mm. As above, the codes are 4-phase-level from family *A* sequences. In all these systems, the refractive index modulation of the SSFBG is chosen so that their peak reflectivity is ~10%, and the input pulse width is ~2ps.

For each configuration, we choose two code sequences to obtain the autocorrelation and crosscorrelation, and the central wavelengths of the two encoding SSFBGs are always equivalent and kept without change. The central wavelength of decoding SSFBGs is varied to produce different offsets with respect to that of encoding gratings. The resultant variations of values of autocorrelation peak and RPCA are shown in Fig.4.15. As anticipated, the system performance deteriorates gradually with the increase of wavelength offset. The values of autocorrelation peak and RPCA are sensitive even to a

wavelength shift of ~0.001nm (~125MHz). Therefore, the temperature of both the encoding and decoding SSFBGs must be accurately controlled to avoid the central wavelength shift. If a system operates at a wavelength of ~1550nm and dn/dT is chosen as 1×10^{-5} $^{o}C^{-1}$, a temperature variation of 0.1 ^{o}C will lead to a central wavelength shift of 0.001nm. In addition, the birefringence of a grating written in a communication fibre is typically 10^{-7}~10^{-5}, which will cause a central wavelength difference of 0.01~0.0001nm. Therefore, the polarization effect must be considered.

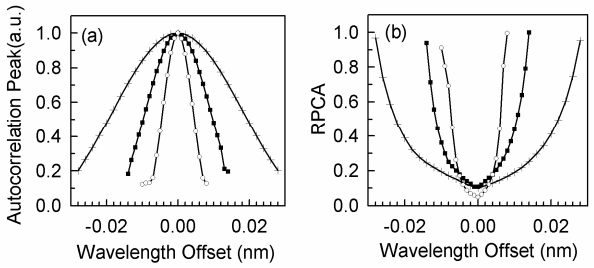

Fig.4.15 (a) The autocorrelation peak and (b) RPCA under the different central wavelength offset between the encoding and decoding SSFBGs. The auto-correlation peaks are normalized to the system with a wavelength offset of 0. Cross (+): 15-chip system with a chip length of 1.25mm. Square (■): 15-chip system with a chip length of 2.5mm. Circle (○): 31-chip system with a chip length of 2.5mm.

The performance deterioration caused by the central wavelength offset of encoding and decoding SSFBGs is due to the fact that this offset breaks the phase matching condition. As shown in Fig.4.15, the tolerance to this central wavelength offset is different for different systems and, roughly, it is inversely proportional to the total length (the product of chip length and chip number) of encoder-decoder gratings. The reflection spectra of encoding-decoding SSFBGs contain many minute structures (see Fig. 4. 4), whose period is inversely proportional to its total length. The breaking of the phase matching condition caused by the central wavelength offset is related to this period. With the increase of the total length of the SSFBGs, the period of the minute structures will become shorter and, consequently, the tolerance of the central wavelength offset will be more stringent. Therefore, for practical systems, the calibration of central wavelength between encoding and decoding gratings is crucial, especially for the SSFBG with a long physical length.

4.4.4 Chip duration

OCDMA systems based on SSFBGs, with different chip durations, have already been demonstrated in experiments [142-150]. The effects of chip duration on the OCDMA system performance are as follows.

(1) Shorter chip duration implies a smaller size of the encoder-decoder because the chip duration is proportional to the chip length of SSFBGs,.

(2) If an SSFBG encoder-decoder is composed of N chips, each with a chip duration of T, a single autocorrelation or crosscorrelation pulse will occupy a time slot of $2NT$. To avoid the interference between neighboring bits in one data sequence, the bit rate of each OCDMA user should be no more than $1/2NT$. Therefore, a shorter chip duration will make a higher data bit rate possible for each user.

(3) SSFBG encoder-decoders with shorter chip duration will occupy a wider frequency slot, which means that for WDM applications of OCDMA, the wavelength channel spacing will have to be wider.

(4) To keep the system performance, an OCDMA system with shorter chip duration requires shorter optical pulses as the input.

(5) The performance of OCDMA systems, with the same chip number and code sequences, is invariant under different chip durations, if a suitable input pulse width is chosen.

We still use the 15-chip, four-phase-level SSFBG encoder-decoder as an example. The chip length is varied from 0.2mm to 10mm, and for each chip length, the input pulse width is accordingly chosen to be the same as the chip duration. The grating strength is chosen so that all the gratings have the same peak reflectivity of ~10%. Numerically, we show the autocorrelation pulse width, and the RPCA between the crosscorrelation Q2:Q1* and autocorrelation Q1:Q1*, under different chip durations in Table 4.1. We can see that, under these particular conditions, the chip duration has no obvious affect on the RPCA value of the system.

Table 4.1 Effects of different chip lengths (chip number = 15)

Chip Length	Input Pulse Width	Autocorrelation Pulse Width	RPCA
0.2mm	2ps	2.9ps	23%
0.5 mm	5ps	5.9ps	23%
1.0 mm	10ps	10.7ps	23%
2.5 mm	25ps	27.4ps	23%
5 mm	50ps	56.7ps	23%
10mm	100ps	111.4ps	23%

4.4.5 Chip number

SSFBG OCDMA systems with increasing chip numbers have been demonstrated [142-150]. A larger chip number corresponds to a longer code sequence and a system with a larger chip number can accommodate more simultaneous users. The reason is that the correlation performance of longer sequences is better than that of shorter sequences. For both bipolar Gold sequences and the quaternary family *A* sequences with a length of *N*, the relative crosstalk level (the ratio between the variance of crosscorrelation and peak of autocorrelation) is $\sim 1/2N$.

Table 4.2 Effects of different chip numbers (chip duration = 5ps)

Chip Number	Input Pulse Width	Autocorrelation Pulse Width	RPCA
8	2ps	3.9	18%
16	2ps	3.9	15%
32	2ps	3.9	6%
64	2ps	3.9	5%

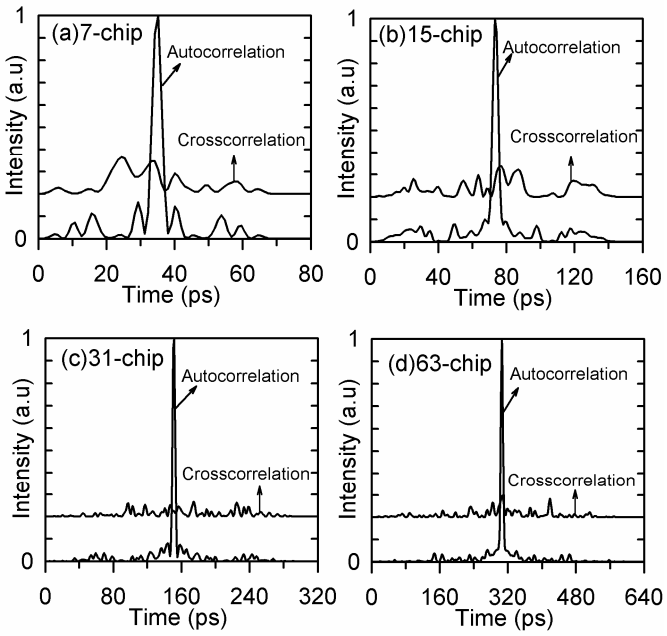

Fig.4.16 Autocorrelation/crosscorrelation traces as chip number is: (a)7, (b)15, (c)31, (d)63, where, chip length = 0.5mm, input pulse width = 2ps. Note that an offset of 0.2 is added to the crosscorrelation traces in the axis of intensity.

We use code sequences from sequence *A* [152], with the chip number of 7, 15, 31, and 63 respectively as an example. The chip length is kept constant to be 0.5mm, and the

input pulse width is 2ps. The autocorrelation pulse width and the RPCA value, under the different chip numbers, are shown in Table 4.2. With an increase of chip number, the RPCA values decrease. The autocorrelation and crosscorrelation pulses, under the different chip numbers, are shown in Fig.4.16.

Nevertheless, for an OCDMA system, with a particular chip duration and a larger chip number, its decoding pulse will occupy a longer time slot and, consequently, the maximum data bit rate each OCDMA user can achieve will be lower. Therefore, to obtain a system with many users, each with a high data bit rate, the SSFBG encoder-decoder should have a large chip number and, at the same time, short chip duration.

4.5 Conclusions

In this chapter, the SSFBG OCDMA systems are studied from the viewpoint of the FBGs. The analytical expressions are derived under the weak grating approximation, and the numerical simulations are performed using the transfer matrix method. They together give us insight into how the encoding and decoding functions are achieved in the SSFBG OCDMA systems, and how and when the autocorrelation and crosscorrelation conditions are satisfied by the SSFBG encoders and decoders.

The effects of input pulse width and various SSFBG parameters are analyzed. The input pulse width has a significant effect on the system performance, and its choice is related to the chip duration of the SSFBG encoder-decoder. With the increase of the SSFBG strength, the reflectivity of the SSFBG increases, while the phase matching condition is gradually broken. In the design of the practical OCDMA system, the choice of the SSFBG strength involves the tradeoff between the power loss of the encoder-decoders, and system performances. The central wavelength of the encoding and decoding SSFBGs must be calibrated with a high accuracy. The chip duration and chip number are also critical parameters, because they are directly related to the maximum data bit rate of each user, and the possible user number of the OCDMA system. Note that in the analysis, although the system performances, such as the encoded pulses, autocorrelation and crosscorrelation pulses, are usually evaluated in the time domain, it is often easier to explain them in the frequency domain.

Chapter 5

Reconfigurable-phase OCDMA en/decoders

5.1 Introduction

Optical code division multiple access (OCDMA) systems based on super-structured fibre Bragg gratings (SSFBGs) have been demonstrated as a promising technique for future optical networks. An SSFBG en/decoder, with a spatial phase distribution following a specific address code sequence, can achieve the function of temporal-phase-encoding, which provides far better correlation performances than the amplitude-only encoding. The conventional SSFBG en/decoders are *discrete-phase en/decoders* because spatial phase distributions in them are formed by inserting discrete phase-shifts, which are shorter than a grating pitch.

In a discrete-phase OCDMA en/decoder, the address code sequence is fixed since it is permanently inscribed during the FBG writing process. It is highly desirable if the code sequence in an FBG en/decoder could be reconfigured dynamically, since this would largely improve the functionality and flexibility of OCDMA networks. Recently, Mokhtar et al. proposed and demonstrated *a reconfigurable-phase en/decoder*, which is composed of a uniform fibre Bragg grating and a series of equidistant tungsten wires in contact with the FBG [9] [153]. Electrical currents pass through the tungsten wires, heat the wires and FBG, and produce a background refractive index variation. This constitutes a phase-shift in the FBG, which can be tuned by varying the electrical currents through the tungsten wires. Because the thermally induced dc (background) refractive index distribution usually covers a length of several millimetres, phase shifts in *a reconfigurable-phase en/decoder* are inherently distributed.

However, in previous work, the distribution of thermally induced phase-shifts in the reconfigurable-phase en/decoders was not characterized and its effect on overall system performances has not been addressed. In this work, based on characterization of the phase-shift distribution of reconfigurable en/decoders, we will analyze the effects of phase-shift distribution on OCDMA system performances. Moreover, the *reconfigurable phase en/decoder*s are improved to possess the capacity of fast reconfiguration.

In conventional discrete-phase en/decoders, phase shifts are induced by spatial gaps between uniform grating sections forming the individual chips. While in the reconfigurable-phase en/decoders, the phase-shifts are produced by thermally induced background refractive index variations along the FBG (as described in Section 3.4.1). A temperature variation of $\Delta T(x)$, applied on the fibre core, will induce a background (dc) effective index variation $\Delta n_{dc}(x)$ along the FBG, and result in a phase shift of

$$\phi = \frac{4\pi}{\lambda_B}\int \Delta n_{dc}(x)dx \tag{5.1}$$

The effective dc refractive index and spatial phase distribution, for a discrete phase-shift and a distributed phase-shift, are compared in Fig. 5.1. The effective dc refractive index for a discrete phase-shift is usually a constant along the FBG, while it is the variation of effective dc refractive index that accumulates and produces a distributed phase-shift. The physical length for a discrete phase-shift is less than a grating pitch, while a distributed phase-shift usually covers a length of several millimeters, containing a number of grating pitches.

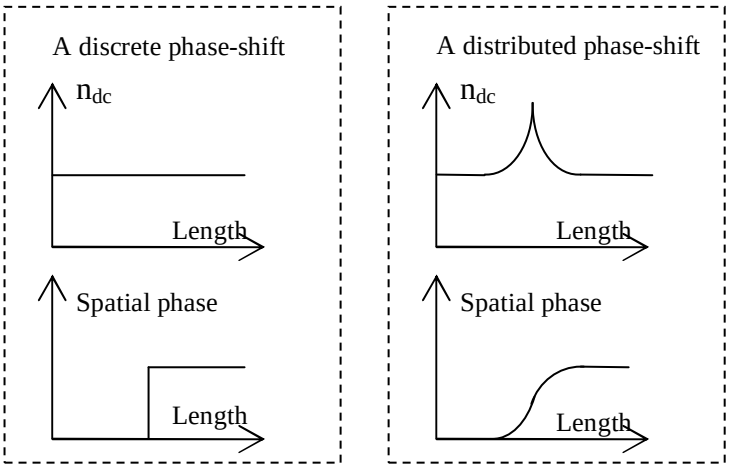

Fig.5.1 The effective dc refractive index and spatial phase distribution for a discrete phase-shift and a distributed phase-shift.

.

This chapter is organized as follows. In Section 5.2, we report our characterization

result of a thermally induced phase-shift. The reconfigurable-phase en/decoders are introduced in Section 5.3 and their system performance is simulated and discussed in Section 5.4. Section 5.5 contains the experimental results, including device fabrication, characterization, performance and demonstration of the capacity for fast reconfiguration.

5.2 Characterizing phase-shifts in reconfigurable-phase en/decoders

5.2.1 Characterization method

A series of tungsten wires are used in a reconfigurable-phase en/decoder to achieve multiple phase-shifts. For simplicity, we assume that the phase-shift or dc refractive index distribution induced by a tungsten wire is not affected by the addition of other tungsten wires. Therefore, the overall dc (background) refractive index distribution in a reconfigurable en/decoder is simply the sum of the dc refractive index distributions corresponding to all the spatially displaced phase-shifts. Later, we will demonstrate this assumption by comparing the measured reflection spectrum of a reconfigurable-phase encoder and the simulated one based on this assumption. This assumption is a good approximation to practice because, although interference among neighboring wires does exist, it is not serious.

Based on this assumption, if the phase-shift and dc refractive index distribution induced by a single tungsten wire are characterized, full information of a reconfigurable en/decoder can be obtained. Two features of the fibre grating with a thermally induced phase-shift have to be characterized. One is the relationship between the applied electric current and the amount of induced phase shift, from which we can determine the electric current required for a particular phase shift. The other is the dc refractive index distribution corresponding to a phase-shift, which is useful for predicting the performance of OCDMA systems based on reconfigurable-phase en/decoders.

Mokhtar et al. have already developed a method to address the first problem [153]. The electrical current is applied only to a tungsten wire in contact with the center of a uniform grating, and the amount of phase-shift is determined by experimentally observing the shift of the dip wavelength in the reflection spectrum of the grating. In the following section, we will use this method to measure the amount of phase-shift induced by different applied electrical currents.

In Chapter 3, we have developed a pulse response method to directly characterize dc refractive index distribution in an FBG with a single thermally-induced phase-shift. A

train of short optical pulses is reflected from the gratings, and the dc refractive index distribution along the grating can be determined by measuring the temporal phase distribution of the reflection pulses. We will use this method to characterize the distribution of thermally induced phase-shifts.

5.2.2 Characterization results

By experimentally observing the shift of the dip wavelength in the reflection spectrum of FBGs, we measure the thermally-induced phase-shifts under different electrical currents as the diameter of the tungsten wires is respectively 18μm, 50μm, or 100μm. The fibre, on which the grating is written, is a standard telecom compatible fibre with a diameter of 125μm (numerical aperture is ~0.12). The results are shown in Fig.5.2. The measurement accuracy for the phase-shifts is ±0.04 π, and the measurement error for the electrical currents is less than 2%. The electrical currents corresponding to a phase shift of 0.5π, π, and 1.5π, which is fundamental for a four-phase-level OCDMA system, are summarized in Table 5.1.

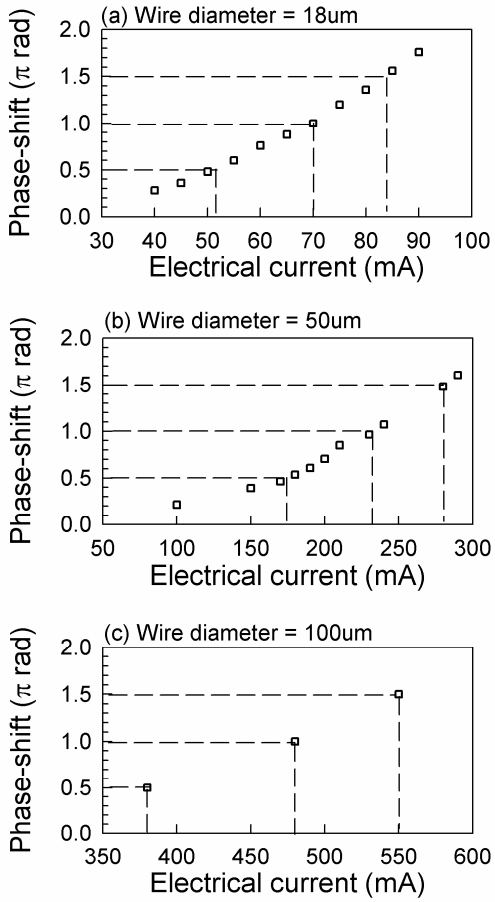

Fig.5.2 The relationship between the amount of phase-shifts and the electrical currents passing through the tungsten wire with a diameter of (a) 18μm, (b) 50μm, or (c) 100μm.

Table 5.1 Electrical currents required for producing a phase shift of 0.5π, π, and 1.5π

Phase-shift (rad)	Electrical current (mA)		
	18μm wire diameter	50μm wire diameter	100μm wire diameter
0.5π	52	174	380
1.0π	70	235	480
1.5π	84	285	550

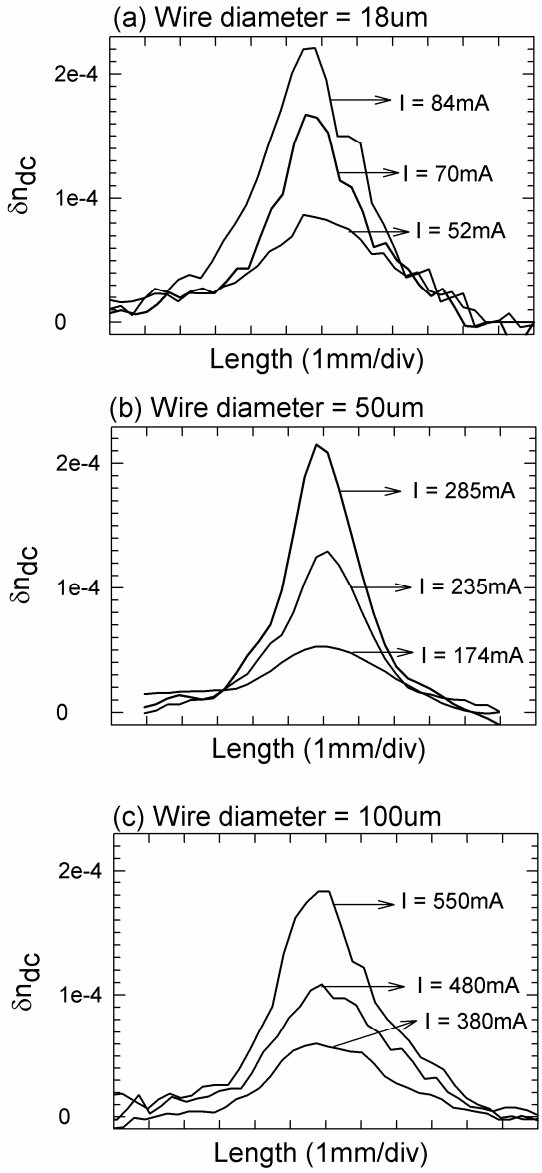

Fig.5.3 Measured distribution of the dc refractive index variation corresponding to a phase-shift of 0.5π, π, and 1.5π as the wire-diameter is (a) 18μm, (b) 50μm, or (c) 100μm.

Using the pulse response method, we characterize the dc refractive index distribution

corresponding to a phase shift of 0.5π, π, and 1.5π as the diameter of the tungsten wires is respectively 18μm, 50μm, or 100μm. The input pulse width used in the measurement is 5ps, and the grating parameters and experimental setup are same as those in Section 3.4.3. The results are shown in Fig.5.3. The measurement error may arise from the non-stability of the input optical pulses, ambient temperature variations or the pulse retrieval algorithm. The maximum dc refractive index variations and FWHM's of their distributions are respectively summarized in Table 5.2 and Table 5.3. From Fig.5.3, the characterization error for the FWHM is estimated to be ±0.2mm.

Table 5.2 Maximum dc refractive index variation for different phase-shifts

Phase-shift (rad)	$\max(\delta n_{dc})$		
	18μm wire diameter	50μm wire diameter	100μm wire diameter
0.5π	0.9×10^{-4}	0.5×10^{-4}	0.6×10^{-4}
1.0π	1.7×10^{-4}	1.3×10^{-4}	1.1×10^{-4}
1.5π	2.2×10^{-4}	2.2×10^{-4}	1.8×10^{-4}

Table 5.3 FWHM of dc refractive index variation for different phase-shifts

Phase-shift (rad)	FWHM (mm)		
	18μm wire diameter	50μm wire diameter	100μm wire diameter
0.5π	4	4.1	3.5
1.0π	2.7	2.5	3.5
1.5π	2.9	2.2	3.0

As we will show later, the FWHM of the dc refractive index distribution corresponding to a thermally induced phase-shift should be as short as possible to achieve OCDMA en/decoders with short chip-duration. From intuition, the thinnest wires should give the most localized dc refractive index distribution. However, the information we obtained from above experimental results is mixed. According to Table.5.3, it seems that the 50μm-diameter-wires will produce dc refractive index distributions with the lowest FWHM, but this is not entirely consistent with the results in Table.5.2, as the 18μm-diameter-wires give the highest maximum-dc-refractive-index-variation at each phase-shift. From a practical point of view, however, the 50μm-diameter wire is the easiest to handle, and we select the 50μm-diameter wires for our reconfigurable-phase en/decoders.

5.2.3 Modelling the phase-shift in a reconfigurable-phase en/decoder

To model the reconfigurable-phase en/decoders using tungsten wires with a diameter of 50μm, we assume that the dc refractive index variation induced by a single wire follows a hyperbolic secant square distribution, as shown in the solid line of Fig.5.4, which is a good approximation to the measured one (also shown in dashed lines in Fig.5.4). The overall distribution of dc refractive index variation in a reconfigurable-phase en/decoder is obtained by adding the dc refractive index distribution corresponding to all the displaced phase-shifts.

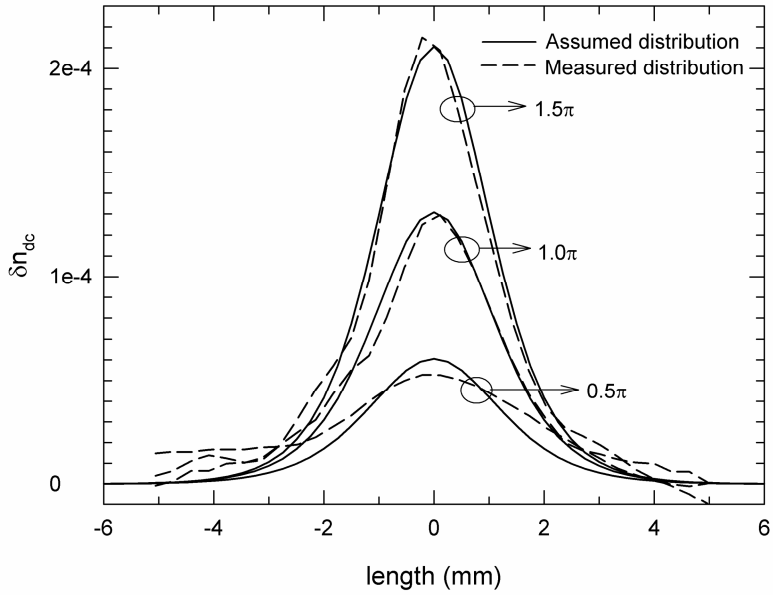

Fig.5.4 Assumed (solid lines) and measured (dashed lines) distributions of dc refractive index variations corresponding to a phase-shift 0.5π, π, and 1.5 π (as the wire-diameter is 50μm).

5.3 Reconfigurable-phase en/decoders

Shown in Fig.5.5 is the structure of a 16-chip reconfigurable-phase en/decoder with a chip-length of 2.5 mm (corresponding to a chip duration of ~25ps). It is constructed by positioning 15 parallel wires 2.5mm apart along the FBG, with the first wire being placed 2.5mm into the grating. The diameter of tungsten wires is 50μm. The uniform FBG is 40 mm long and is written in a standard telecom compatible fibre with a numerical aperture (NA) of ~0.12. As mentioned above, the phase-shifts are introduced by the localized heat from tungsten wires and can be controlled by varying the electrical currents passing through the wires. This causes the temperature and dc refractive index variation on the FBG and, consequently, results in a reconfigurable-phase en/decoder.

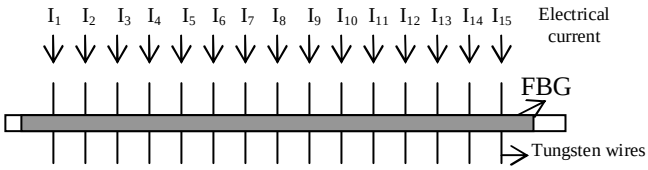

Fig.5.5 Device layout of a 16-chip reconfigurable-phase en/decoder.

Two 15-bit quaternary codes, Q1 = [1.5π 0.0π 0.0π 0.5π 1.0π 0.0π 0.0π 1.5π 0.5π 1.5π 0.5π 0.0π 0.5π 1.0π 1.5π], and Q2 = [1.5π 0.5π 1.0π 1.5π 0.0π 0.5π 1.5π 1.0π 0.0π 1.5π 0.0π 0.0π 0.0π 0.5π 0.5π], are chosen from the family *A* sequences [152]. By applying appropriate electrical currents along the 15 wires, a reconfigurable-phase en/decoder with a code sequence of Q1 or Q2 can be achieved. Q1R and Q2R are used to designate reconfigurable-phase encoders with code sequences of Q1 and Q2, while Q1R* and Q2R* are corresponding reconfigurable-phase decoders.

By adding the dc refractive index variation distribution, corresponding to all the spatially displaced phase-shifts, the overall dc refractive index distributions in Q1R and Q2R are obtained and shown in Fig. 5.6. They are based on the single-phase distribution shown in the solid lines in Fig. 5.4.

In the following simulation and experiments, we will also use discrete-phase en/decoders. Q1D and Q2D are respectively used to designate 16-chip discrete-phase encoders with code sequences of Q1 and Q2, while Q1D* and Q2D* are the corresponding decoders. The chip lengths of Q1D, Q2D, Q1D*, and Q2D* are also 2.5mm. Shown in Fig. 5.7 are the spatial phases of discrete-phase encoders Q1D and Q2D.

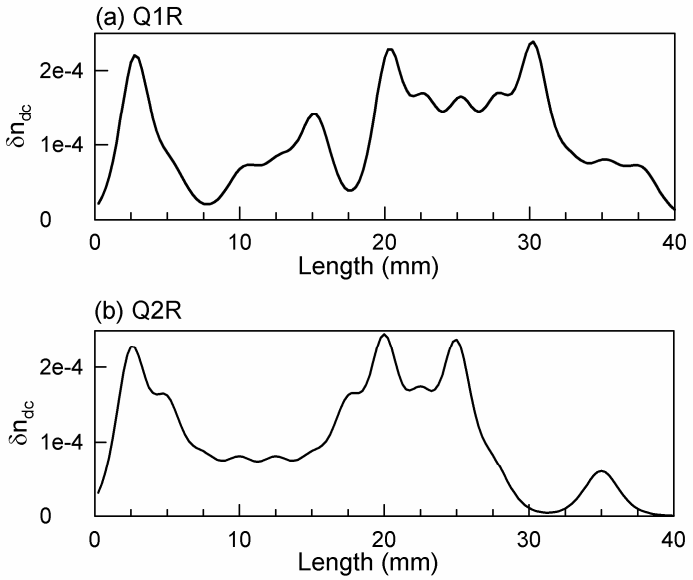

Fig.5.6 dc refractive index distributions of the reconfigurable-phase encoders (a) Q1R and (b) Q2R.

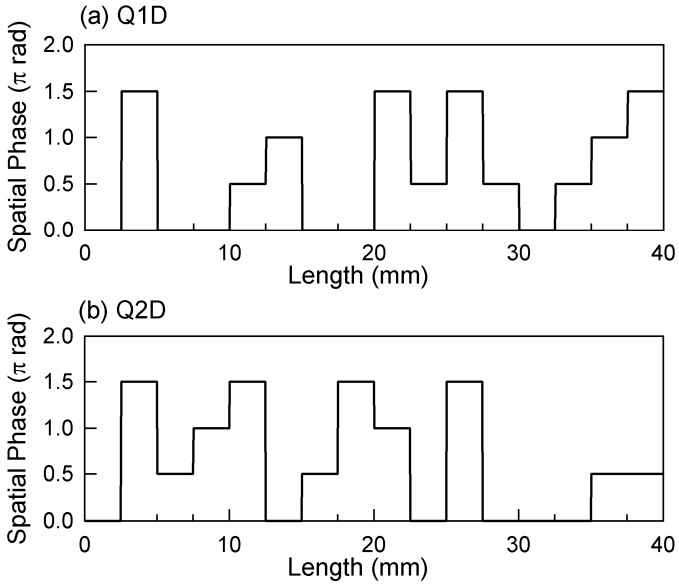

Fig.5.7 Spatial phases of the discrete-phase encoders (a) Q1D and (b) Q2D.

5.4 OCDMA systems based on reconfigurable-phase decoders

5.4.1 En/decoders with distributed or discrete phase-shifts

In this section, we will first compare the spatial phase distribution, reflection spectra, and encoding pulses of discrete-phase en/decoders and reconfigurable-phase en/decoders. Then, OCDMA systems using discrete-phase encoders and reconfigurable-phase decoders are simulated. The Bragg wavelength, and effective index modulation of all the

encoding and decoding gratings (Q1D, Q2D, Q1D*, Q2D*, Q1R, Q2R, Q1R* and Q2R*) are respectively 1550nm, and 1.0×10^{-5}. The peak reflectivity of all the FBG en/decoders used for the simulation is less than 20%.

The spatial phase distribution in the reconfigurable-phase encoder Q1R is obtained from Fig.5.6 (a) by using $\phi = \frac{4\pi}{\lambda_B}\int \Delta n_{dc}(x)dx$ and is shown in Fig. 5.8. Spatial phase distribution in the discrete-phase encoder Q1D is also shown in Fig. 5.8, in a dashed line for comparison. We can find that the spatial phase distribution in the reconfigurable-phase encoder Q1R is an approximation to that in the discrete-phase device Q1D.

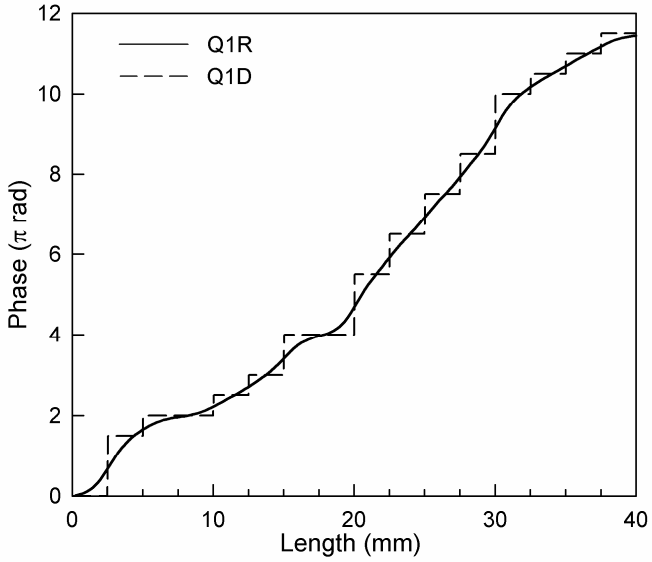

Fig.5.8 Spatial phase distributions in Q1D and Q1R.

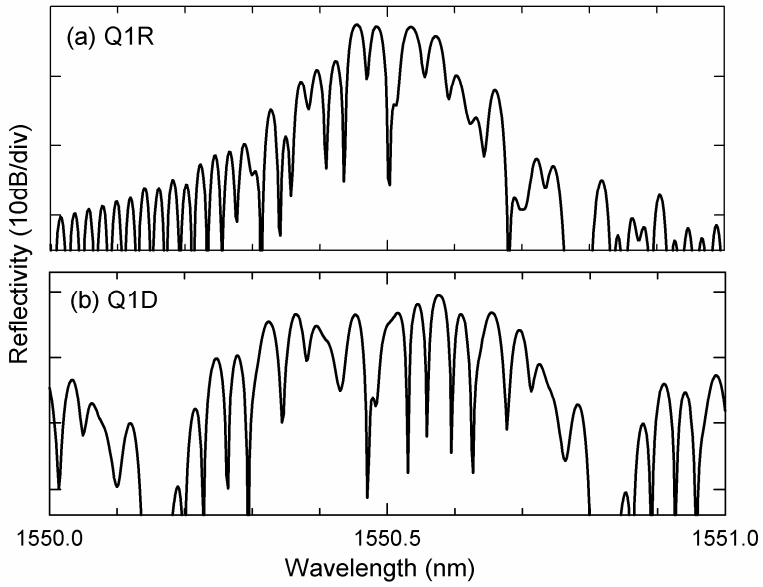

Fig.5.9 Simulated reflection spectra of (a) Q1R and (b) Q1D.

The simulated reflection spectra of the reconfigurable-phase FBG Q1R and discrete-phase FBG Q1D are respectively shown in Fig.5.9 (a) and (b). For the same nominal address codes, the reflection spectrum of the reconfigurable-phase-encoder is narrower than that of the discrete-phase-encoder and it also has much lower spectral features away from the main band.

The simulated pulse responses (when the input pulse width is 2ps) of the reconfigurable-phase grating Q1R and discrete-phase grating Q1D are shown in Fig.5.10 (a) and (b). The central wavelength of input optical pulses is tuned to the central wavelength of the gratings. The response of Q1R is a pulse with distinct edges and a smooth top-section, while that of Q1D is composed of a series of short pulses divided by dips at each phase transition. For both Q1R and Q1D, temporal phases of the reflected pulses strictly follow the spatial phases of corresponding gratings. This is called temporal phase encoding.

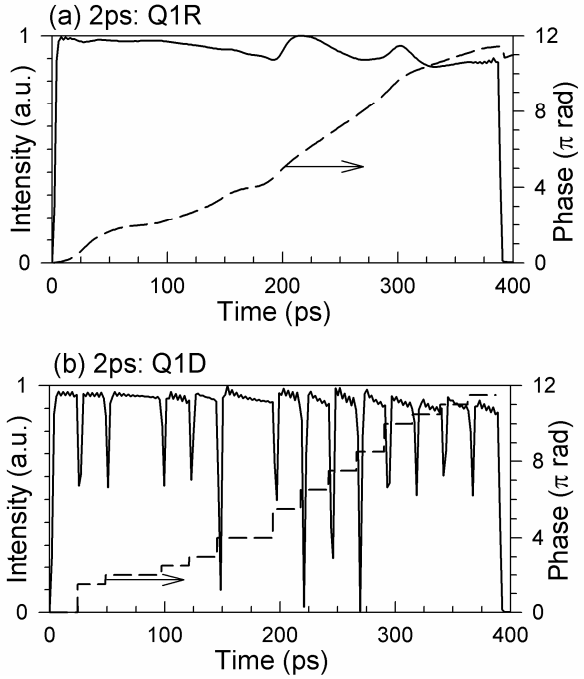

Fig.5.10 Simulated pulse responses of (a) Q1R and (b) Q1D (the input pulse width is 2ps).

5.4.2 Correlation between distributed and discrete phases

In a reconfigurable OCDMA system, the fixed-code devices with discrete phase-shifts are used as encoders, while the reconfigurable-phase devices with distributed phase-shifts are used as decoders. In this section, we will show how the distributed phases in

reconfigurable-phase decoders correlate with discrete phases in the discrete-phase encoders.

Shown in Fig. 5.11 (a) is the simulated decoding pulse as the encoders are Q1D plus Q2D, and the decoder is Q1R*, while in Fig. 5.11 (b) the decoder is Q1D* (when the input pulse width is 2ps). The central wavelength of the input optical pulses is tuned to the central wavelength of en/decoding FBGs. Firstly, the autocorrelation pulse width of Q1D: Q1R* is broader than that of Q1D: Q1D*. Secondly, the side-lobes of autocorrelation Q1D: Q1R* are higher than that of Q1D: Q1D*. Thirdly, the ratio between the peak of cross and auto correlation (RPCA) of (Q1D+Q2D): Q1R* is larger than that of (Q1D+Q2D): Q1D*. All these differences are due to the fact that phases of encoder Q1D and decoder Q1D* are completely conjugate, while the phases of encoder Q1D and decoder Q1R* are only approximately conjugate. Therefore, the decoding performance is largely dependent on the specific distribution length of the distributed phases. It is apparent that the more confined the distributed phase-shifts are, the better they will match the discrete phase-shifts. Nevertheless, as shown in Fig.5.11 (a), even when the lengths of the phase-shift distribution are comparable to the chip length, the autocorrelation pulse, and hence the recognition signature, is still clear.

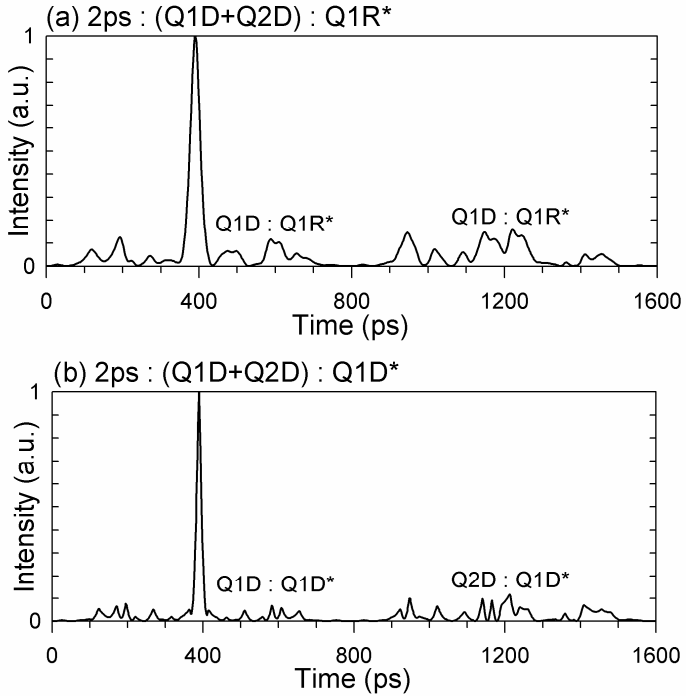

Fig.5.11 Simulated decoding pulse as the encoders are Q1D plus Q2D, and the decoder is (a) Q1R*, or (b) Q1D* (when the input pulse width is 2ps).

5.4.3 Choice of chip length

As shown in Fig. 5.4, if the tungsten wires used in reconfigurable-phase decoders have a diameter of 50μm, the FWHM of a single-phase-shift distribution is ~2.5mm. In this section, by a numerical simulation, we will show how to choose the chip length of the reconfigurable OCDMA en/decoders.

We assume that the total length of en/decoders is 40mm and compare three configurations of reconfigurable en/decoders: (a) chip number = 8, and chip length = 5mm; (b) chip number = 16, and chip length = 2.5mm; (c) chip number = 32, and chip length = 1.25mm. Note that for all the three configurations, the FWHM of a single-phase-shift distribution is 2.5mm. The codes for (a) are chosen from the Gold sequences [151], while the codes for (b) and (c) are chosen from the Family *A* sequences [152].

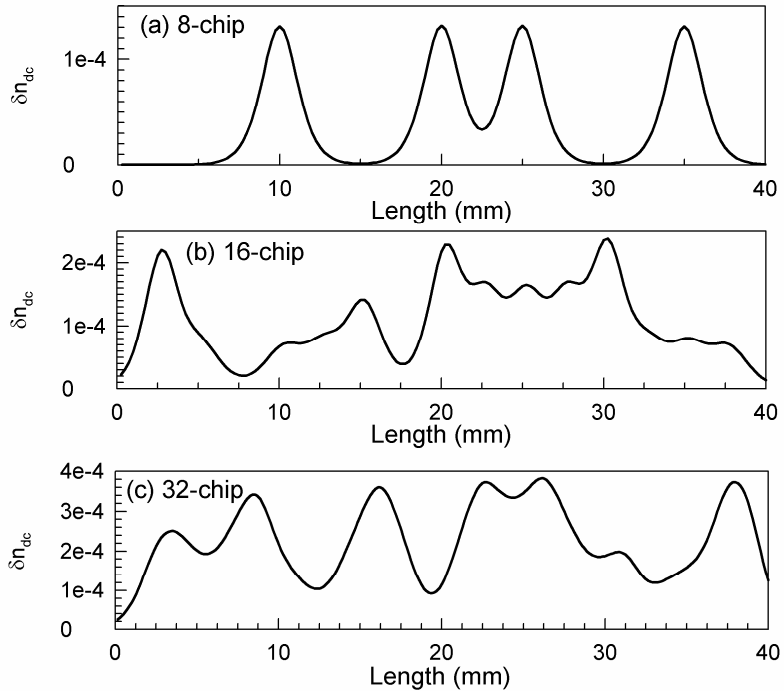

Fig.5.12 dc refractive index distributions in reconfigurable-phase encoders with a configuration of (a) chip number = 8, and chip length = 5mm; (b) chip number = 16, and chip length = 2.5mm; (c) chip number = 32, and chip length = 1.25mm.

Shown in Fig.5.12 are the dc refractive index distributions in reconfigurable-phase encoders with a configuration of (a), (b) or (c). The dc refractive index distribution corresponding to a code is obtained by adding the dc refractive index distribution corresponding to all the displaced phase-shifts, and the dc refractive index distribution of a single phase-shift follows the solid lines in Fig.5.4. For a chip length of 5 mm, the adjacent phase-shifts are nearly separate; for a chip length of 2.5 mm, equivalent to the

FWHM of a single-phase-shift distribution, the adjacent phase-shifts begins to have an obvious interference; for a chip length of 1.25 mm, all the adjacent phase-shifts are interleaved together.

To calculate the auto and cross correlation performances, two codes are chosen for each configuration. For all the three configurations, the fixed-code devices with discrete phase-shifts are used as encoders, while the reconfigurable devices with distributed phase-shifts are used as decoders. The decoding (auto and cross correlation) pulses under the three configurations are shown in Fig.5.13. In the simulation, the input pulse width is 2ps and the index modulation of the gratings is chosen so that their peak reflectivity is less than 10%. Based on comparing RPCA's under the three configurations, we find that configuration (b) has the best performance. The better performance of (b) over (a) is due to the fact that the code sequences in configuration (b) are longer than in (a). Although the code sequences in configuration (c) are longer than in (b), the performance of (c) is still no better than in (b) because in configuration (c), the single-phase-shifts are seriously smeared by the short chip-length.

However, if only considering the autocorrelation pulse, we find that configuration (c) has the best performance. The autocorrelation of configuration (c) has the shortest pulse-width and lowest side-lobes.

In practical OCDMA systems, both the autocorrelation and cross-correlation are important. Therefore, in the following experiments, the chip length of reconfigurable-phase en/decoders will be chosen as 2.5 mm.

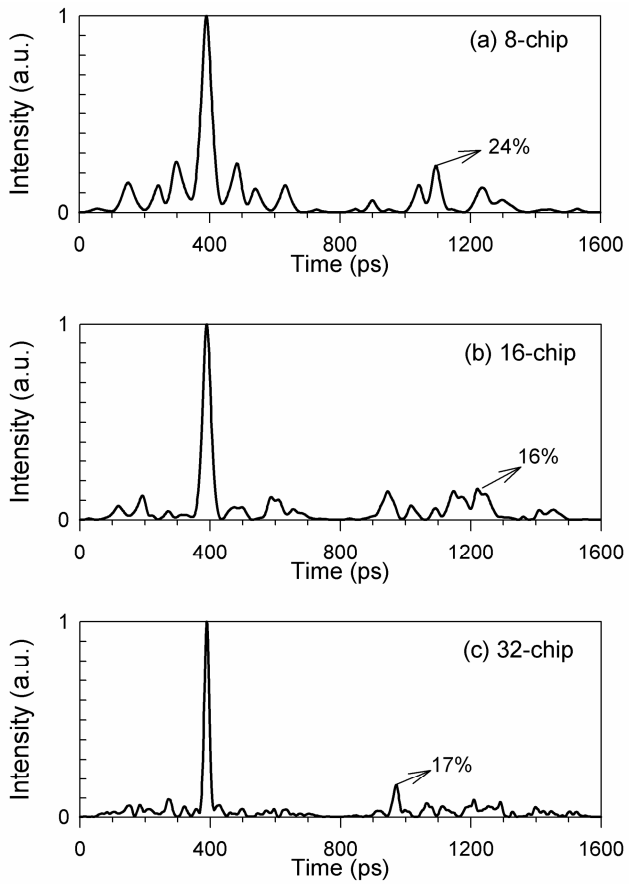

Fig.5.13. Simulated decoding (auto and cross correlation) pulses under the configurations (a) 8-chip, (b) 16-chip, and (c) 32-chip.

5.5 Experiments and results

5.5.1 Device parameters and characterization

To test the performances of reconfigurable OCDMA systems, we fabricate discrete-phase en/decoders Q1D, Q2D, Q1D*, Q2D*, and reconfigurable-phase en/decoders Q1R, Q2R, Q1R*, Q2R*. The encoding and decoding gratings used in following experiments have the same code sequences and designations as in Section 5.4. Their Bragg wavelength, effective index modulation, chip length, and total length are respectively 1550nm, 2.2×10^{-5}, 2.5mm and 40mm. The peak reflectivity of all the FBG en/decoders for the experiments is less than 50%.

The discrete-phase en/decoders are fabricated using the continuous grating writing technique (as described in section 2.3.3). The spatial phase distributions of Q1D and Q2D have been shown in Fig.5.7. Note that Q1D* and Q2D* are respectively the physically reversed gratings of Q1D and Q2D. To obtain reconfigurable-phase en/decoders, uniform gratings are written in a standard telecom compatible fibre. The reflection spectrum of the

uniform grating is shown in Fig. 5.14. The 16-chip reconfigurable-phase en/decoders Q1R, Q2R, Q1R*, Q2R* with a chip length of 2.5mm are constructed using the technique described in Section 5.3. The diameter of tungsten wires used for constructing the reconfigurable devices is 50μm. Therefore, the dc refractive index distribution in the reconfigurable-phase en/decoders could be obtained based on the single-phase-distribution shown in the solid lines in Fig.5.4. The dc refractive index distributions in Q1R and Q2R have been shown in Fig.5.6. Note that Q1R* and Q2R* are respectively the physically reversed gratings of Q1R and Q2R.

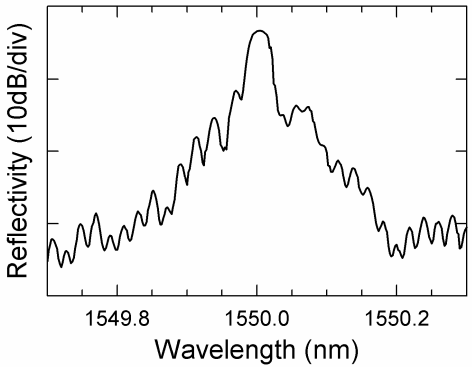

Fig.5.14 Reflection spectrum of the uniform grating.

Shown in Fig. 5.15 (a) and (b) are the simulated (dashed lines) and measured (solid lines) reflection spectra of reconfigurable-phase encoders Q1R and Q2R. In the simulation, the dc refractive index distributions of Q1R and Q2R follow those shown in Fig.5.6. The measurements roughly agree with the simulation results. This agreement also demonstrates our previous assumption: the overall dc (background) refractive index distribution in a reconfigurable-phase en/decoder could be approximated by directly adding dc refractive index distributions corresponding to all the spatially displaced phase-shifts.

Shown in Fig. 5.15(c) and (d) are the reflection spectra of discrete-phase encoders Q1D and Q2D. The excellent agreement between the experiment and simulation results demonstrates the high-quality of grating writing technique. For the same nominal address codes, the reflection spectra of the reconfigurable-phase-encoders are narrower than those of the discrete-phase-encoders and they also have much lower spectral features away from the main band. Their spectral inequality occurs because the phase-shifts are distributed for the reconfigurable device, while they are discrete for the fixed one.

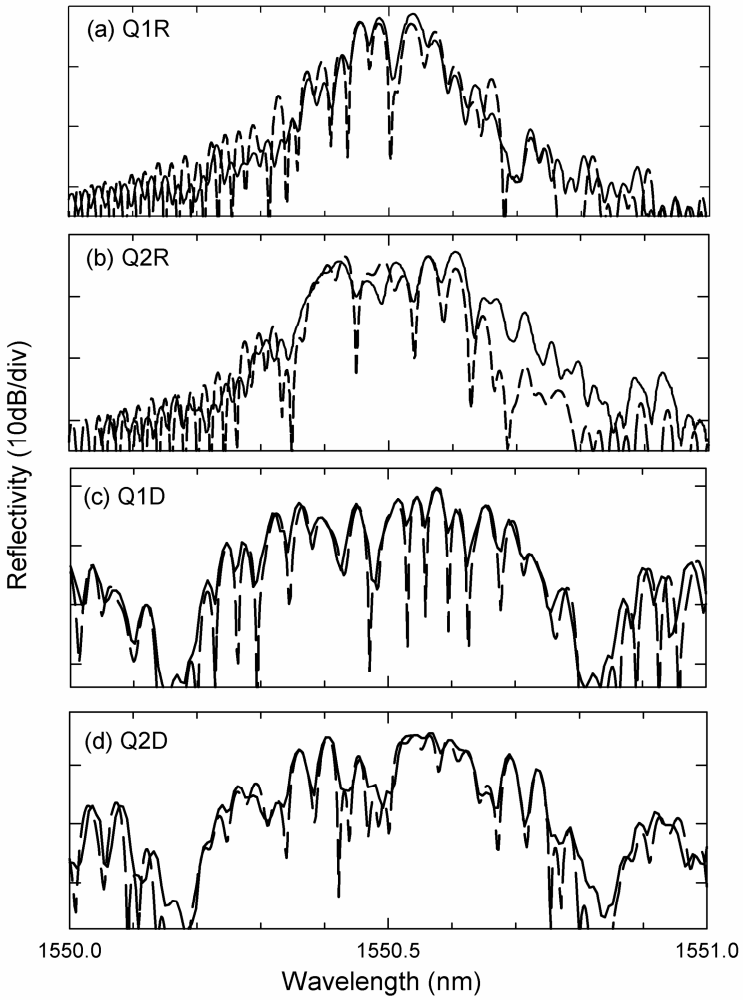

Fig.5.15 Simulated (dashed lines) and measured (solid lines) reflection spectra of reconfigurable-phase encoders (a) Q1R, (b) Q2R, and discrete-phase encoders (c) Q1D (d) Q2D.

5.5.2 Systems using discrete-phase encoders and reconfigurable-phase decoders

We first test the OCDMA system using discrete-phase encoders (Q1D and Q2D) and reconfigurable-phase decoders (Q1R* or Q2R*). The experimental setup is shown in Fig.5.16. A tunable laser, operated at ~1550 nm, is carved through an electro-absorption modulator (EAM) which is driven by a 10GHz sinusoidal clock signal, producing a 10GHz pulse train with an FWHM of ~20 ps. The pulse train is then modulated by a $LiNbO_3$ electro-optic intensity modulator (EOM) in response to the data signal from a pseudo-random pattern generator (PPG). This pulse train is split by a 3dB coupler into two parts, each reflected from the fixed and discrete-phase encoders Q1D and Q2D, respectively, and then combined by another 3dB coupler. A fibre time-delay-line is utilized to divide the signals from the two encoding gratings in the time domain. Then the combined signal is reflected from the reconfigurable-phase decoding grating Q1R* or

Q2R*.

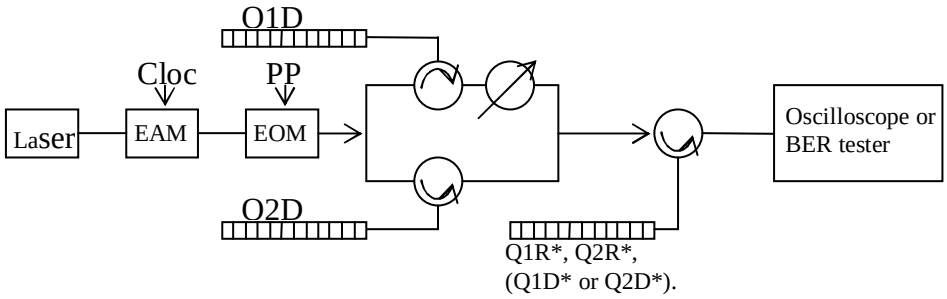

Fig.5.16 Experimental setup.

By applying a 300MHz clock signal through the PPG, a 300MHz pulse train with an FWHM of ~20 ps is produced from the EOM. The decoded pulses are detected with a 20GHz photodiode and then fed into a fast sampling oscilloscope. The measured and calculated auto- and cross correlation pulses, when the reconfigurable-phase devices (Q1R* and Q2R*) are used for decoding, are shown in Fig.5.17 (a) and (b). The measured ratios between the peak of cross and auto correlation (RPCA) are ~34%. The autocorrelation pulse widths are measured by an autocorrelator, which is based on the second-harmonic-generation (SHG) technique. When the decoder is a reconfigurable FBG, the output pulse width is ~39ps.

For comparison, we also measure the system using fixed-code devices (Q1D* and Q2D*) as decoders. The measured and calculated auto- and cross correlation pulses are shown in Fig.5.17 (c) and (d). The measured ratios between the peak of cross and auto correlation are ~30%. The autocorrelation pulse widths are measured to be ~23ps. Note that the input pulse width is ~20ps, while the chip duration is ~25ps.

If we compare the experimental results (the input pulse with is 20ps) shown here and the simulation results shown in Fig.5.11 (the input pulse width is 2ps), we find that using a shorter input pulse can improve the performance of the fixed-code system, while it has no obvious effect on the reconfigurable-code system. This we believe can be explained from Fig.5.15, which shows that the reflection spectrum of a reconfigurable-phase device is narrower than that of a fixed-code device, therefore implying that the reconfigurable device is more tolerant to a longer input pulse width.

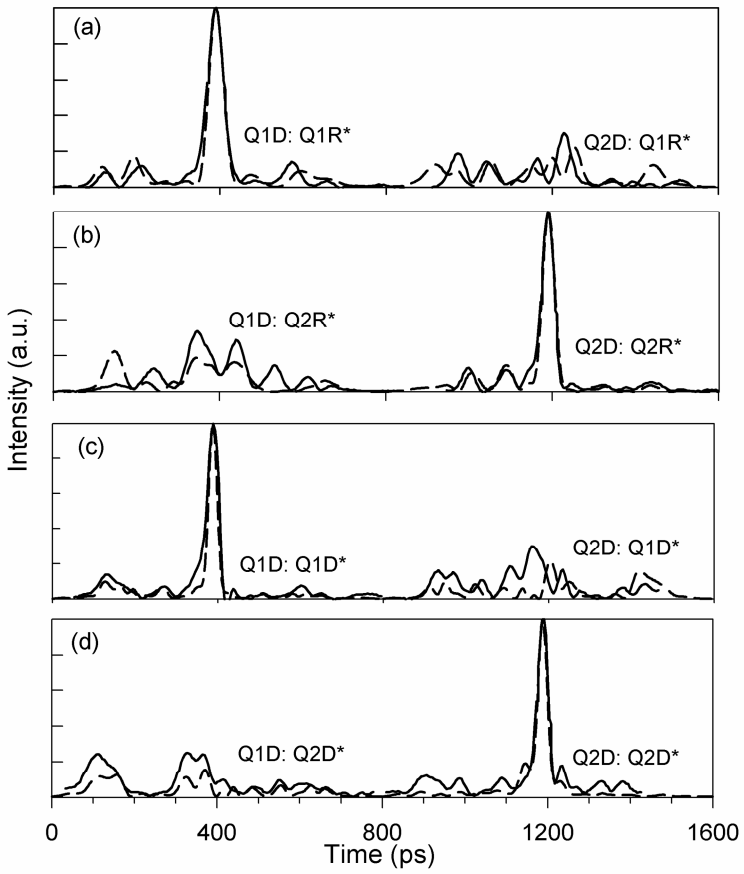

Fig.5.17 Measured (solid lines) and calculated (dashed lines) decoded pulses for decoder (a) Q1R*, (b) Q2R*, (c) Q1D*, and (d) Q2D*.

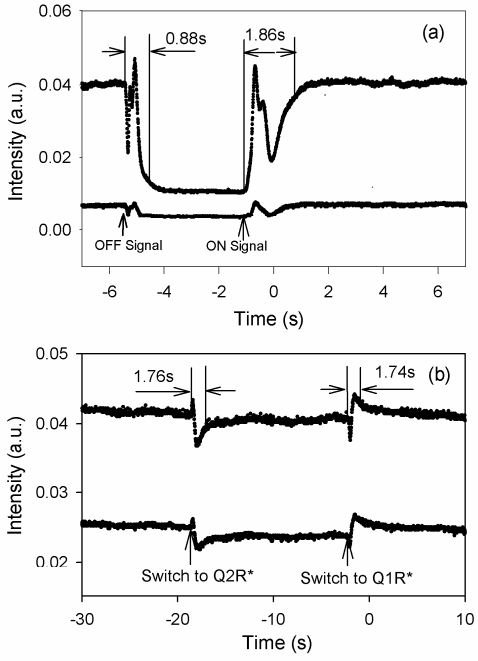

Fig.5.18 The power of decoded pulses (a) when the reconfigurable decoder is switched ON-OFF-ON, (b) when the phase code sequence is switched from Q1R* to Q2R*, and then back to Q1R*.

The tuning speed of the reconfigurable-phase decoders is measured by feeding the decoded pulses into an oscilloscope having an effective detection bandwidth of 100MHz. The experimental setup is the same as Fig.5.16. The reconfigurable decoder is switched from ON to OFF by controlling wire-currents, and then back to ON, i.e., from code to no code (uniform grating) and back to code. The power of the reflected signal (in the ON state, it is the peak of autocorrelation pulse; in the OFF state, it is measured at the background noise level) from the reconfigurable decoder is shown in Fig.5.18 (a). Furthermore, the phase code sequence is switched from Q1R* to Q2R*, and then back to Q1R*. The power of the reflected signal (including autocorrelation and crosscorrelation pulses) from the reconfigurable decoder is shown in Fig.5.18 (b). The response time of all the switching process is observed to be less than 2s. This is due to the fact that the tungsten wire has a fast heat response to electrical currents, and the silica fibre used as the host for the gratings also has a fast thermo-optic response.

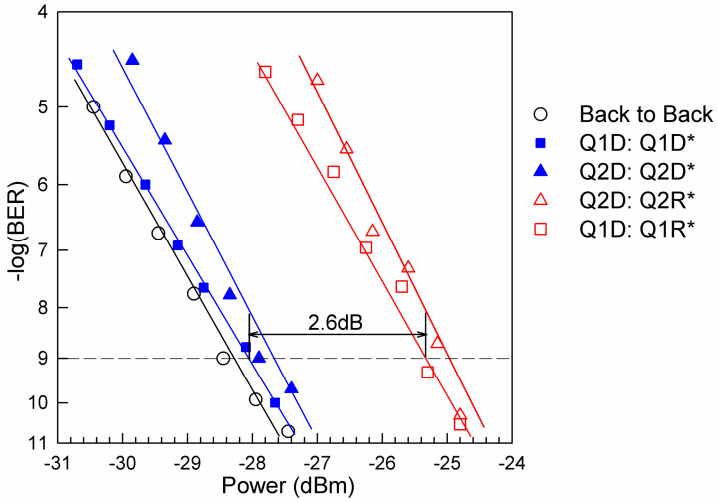

Fig.5.19 BER test results for the system which uses fixed or tunable decoders (the data bit rate is 1.25 Gb/s).

The bit error rate (BER) of the autocorrelation is then measured when the data bit rate is 1.25 Gb/s (with a 2^7-1 pseudo-random-bit-sequence data pattern). In this BER test, only one encoder and its corresponding fixed or reconfigurable decoder exist in the experimental setup, therefore, no cross-correlation interferes with the autocorrelation signal. The results are summarised in Fig.5.19. Due to the appearance of autocorrelation side-lobes, a power penalty is measured in the autocorrelation signal compared with the back-to back case. The power penalty is ~0.6dB when the decoder is a fixed-code FBG. An additional ~2.6dB penalty is measured when the decoder is a reconfigurable FBG.

This additional penalty is found mainly to be due to the increased power in the shoulders of autocorrelation pulses when a distributed-phase grating is used.

5.5.3 Systems using reconfigurable-phase encoders and decoders

We also test the OCDMA system using reconfigurable-phase encoders (Q1R or Q2R) and decoders (Q1R* or Q2R*). The experimental setup is similar to Fig.5.16. The input pulse train, with a pulse-width of ~5ps, is from a gain-switched semiconductor laser.

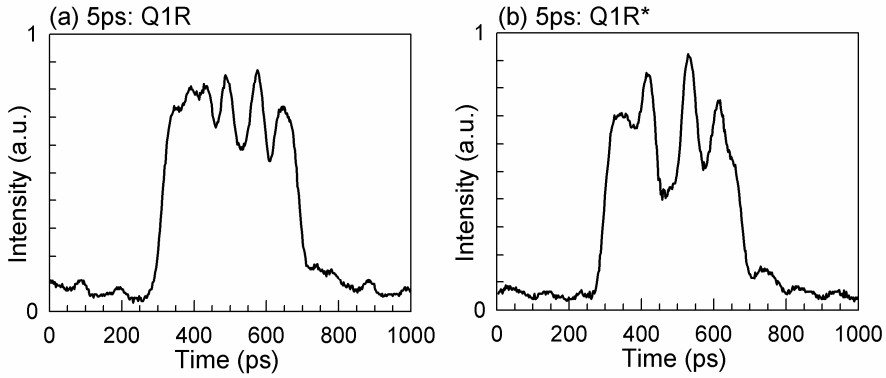

Fig.5.20 Measured pulse responses of (a) encoder Q1R and (b) decoder Q1R* (the input pulse width is ~5ps).

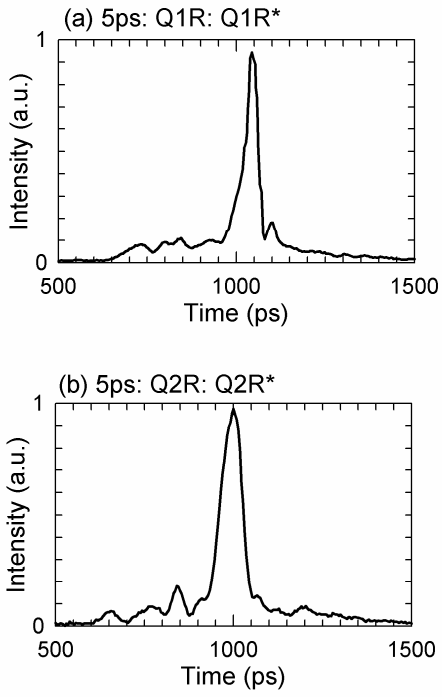

Fig.5.21 Measured autocorrelation pulses when the encoders and decoders are respectively (a) Q1R: Q1R* and (b) Q2R: Q2R* (the input pulse width is ~5ps).

First, the pulse responses (the input pulse width is ~5ps) of encoder Q1R and decoder Q1R* are detected with a 20GHz photodiode and a fast sampling oscilloscope. The

results are shown in Fig.5.20. Then, Q1R (or Q2R) is used as encoder and Q1R* (or Q2R*) is used as decoder. The resultant autocorrelation pulses are measured and shown in Fig.5.21. Note that in this configuration, the phases of reconfigurable-phase encoders and decoders are completely conjugate. In next chapter, we will develop a new fixed-code en/decoder, whose phase profile is designed to match a reconfigurable en/decoder accurately.

5.6 Conclusions

We have made a detailed study on the reconfigurable-phase OCDMA en/decoder based on fibre Bragg gratings and a thermal tuning technique. The distribution of thermally induced phase-shift is characterized using the pulse response method reported in Chapter 3. This characterization provides us the fundamental information to model, analyze and design reconfigurable-phase OCDMA en/decoders.

Based on the characterization result, the diameter of tungsten wires is chosen so that the distribution of the thermally induced phase-shifts is most confined, and the chip length for configurable-phase en/decoders is also determined. New reconfigurable-phase en/decoders are fabricated and tested. The fast-reconfiguration capacity of reconfigurable-phase decoders is experimentally demonstrated. The tuning time between two different phase codes is measured to be less than 2s.

By experiments as well as simulation, an OCDMA system using discrete-phase encoders and reconfigurable-phase decoders is compared with a system using fixed-code discrete-phase encoder and decoders and, although the system using discrete-phase decoders exhibits a shorter output autocorrelation pulse width and lower side-lobes, the system using reconfigurable-phase decoders has advantages of flexibility and a more relaxed requirement on the input pulse width. In the next Chapter, new fixed-code continuous-phase OCDMA en/decoders will be developed.

The reconfigurable-phase en/decoders described in this Chapter have already been used to recognize the optical header in an all-optical packet switching system. The relevant experimental results are reported in Ref [154-155].

Chapter 6

Continuous-phase OCDMA en/decoders

6.1 Introduction

In the reconfigurable OCDMA systems, described in Chapter 5, reconfigurable-phase decoders, which inherently have distributed phase-shifts, are used to retrieve the signals from discrete-phase encoders with fixed-codes. In this configuration, although the encoders and decoders are not completely conjugate, the final autocorrelation and cross-correlation performances are still acceptable. However, under equal nominal code sequence, the spatial phase distribution in *a reconfigurable-phase en/decoder* does not completely match that of *a discrete-phase en/decoder*.

In this chapter, we propose and experimentally demonstrate a novel fixed-code and *continuous-phase en/decoder* with a phase profile designed to match a reconfigurable en/decoder accurately. Thus, this new continuous-phase device has the inherent advantage to operate together with reconfigurable-phase devices in reconfigurable OCDMA systems.

This chapter is organized as follows. The structure of a continuous-phase en/decoder is introduced in Section 6.2. The device and system performances of continuous-phase en/decoders are simulated and compared with those of discrete-phase devices in Section 6.3. In Section 6.4, 16-chip continuous-phase, discrete-phase, and reconfigurable-phase OCDMA en/decoders are fabricated and OCDMA systems with several different configurations are tested. In Section 6.5, 31-chip devices are built and, by exploiting the narrow-bandwidth characteristics of continuous-phase devices, a 16-channel OCDMA/DWDM system is demonstrated with a WDM channel spacing of only 0.4nm.

6.2 Continuous-phase en/decoders

In a discrete-phase en/decoder, a spatial gap ΔL in the grating structure constitutes a phase-shift $\phi = \frac{4\pi}{\lambda_B} n_{eff} \Delta L$. On the contrary, in a reconfigurable-phase en/decoder, a phase-shift is given by $\phi = \frac{4\pi}{\lambda_B} \int \delta n_{dc}(x) dx$, where $\delta n_{dc}(x)$ is the additional dc effective refractive index change. With the same code sequence, the novel fixed-code continuous-phase en/decoder will have the same dc refractive index distribution as a reconfigurable-phase encoder-decoder.

In Chapter 5, we have, using the pulse response method, characterized the distribution profile of a thermally induced single phase-shift 0.5π, 1.0π or 1.5π. The dc refractive index distribution corresponding to a single phase-shift in a continuous-phase en/decoder will follow that in a reconfigurable-phase en/decoder, which is shown in Fig.6.1.

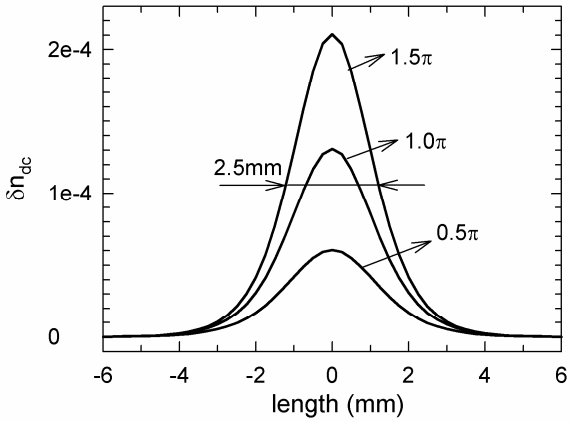

Fig.6.1 dc refractive index distribution corresponding to a single phase-shift.

We choose the same 16-bit quaternary codes Q1 and Q2 from the family *A* sequences as in Chapter 5. Q1C and Q2C are used to designate the continuous-phase encoders with code sequences of Q1 and Q2. As in a reconfigurable-phase encoder, the dc refractive index distribution in a continuous-phase encoder is also obtained by adding the dc refractive index distributions of all the spatially displaced phase-shifts. Based on the single-phase distribution in Fig.6.1, the dc refractive index distributions in Q1C and Q2C are calculated and shown in Fig.6.2.

Reconfigurable-phase encoders Q1R and Q2R have already been described in Chapter 5. Their dc refractive index distributions are shown in Fig.5.6. It can be seen that, with the same code sequences, the continuous-phase en/decoders have the same dc refractive

index distributions as the reconfigurable-phase en/decoders.

In this Chapter, we still use Q1D and Q2D to designate the discrete-phase encoders with code sequences of Q1 and Q2, whose spatial phase distributions have been given in Fig.5.7.

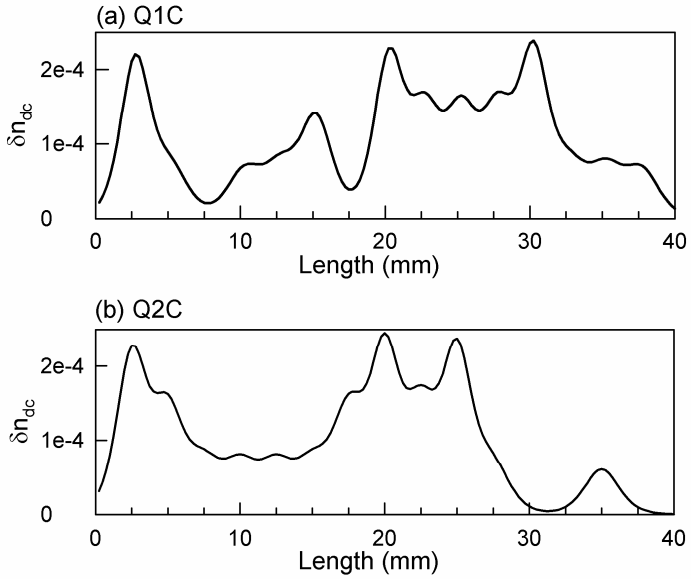

Fig.6.2 dc refractive index distributions of continuous-phase encoders (a) Q1C and (b) Q2C.

6.3 OCDMA systems based on continuous-phase en/decoders

6.3.1 Encoding and decoding of continuous-phase en/decoders

In this section, we will show the reflection spectra, encoding pulses and decoding pulses of continuous-phase en/decoders Q1C, Q2C, Q1C*, and Q2C* by simulation. Chip number, chip length, and effective index modulation of all these en/decoders are respectively 16, 2.5mm, and 1.0×10^{-5}. The peak reflectivity of all the FBGs for simulation is less than 20%.

The simulated reflection spectra of continuous-phase encoder Q1C and discrete-phase encoder Q1D are shown in Fig.6.3 (a) and (b) respectively. For the same nominal address code, a continuous-phase en/decoder has the same simulated reflected spectrum as a reconfigurable-phase en/decoder since they have the same spatial phase distribution, while a continuous-phase en/decoder has a narrower reflection spectrum than a discrete-phase en/decoder.

The simulated pulse responses (intensities and phases) of continuous-phase encoder Q1C and decoder Q1C* are shown in Fig.6.4 (a) and (b) when the input pulse width is 5ps. The central wavelength of input optical pulses is tuned to the central wavelength of

en/decoders. For both Q1C and Q1C*, temporal phases of the reflected pulses follow the spatial phases of corresponding gratings. The spatial phases of Q1C* and Q1C are conjugate, therefore, the pulse responses of Q1C* and Q1C are also conjugate as the FBGs are weak.

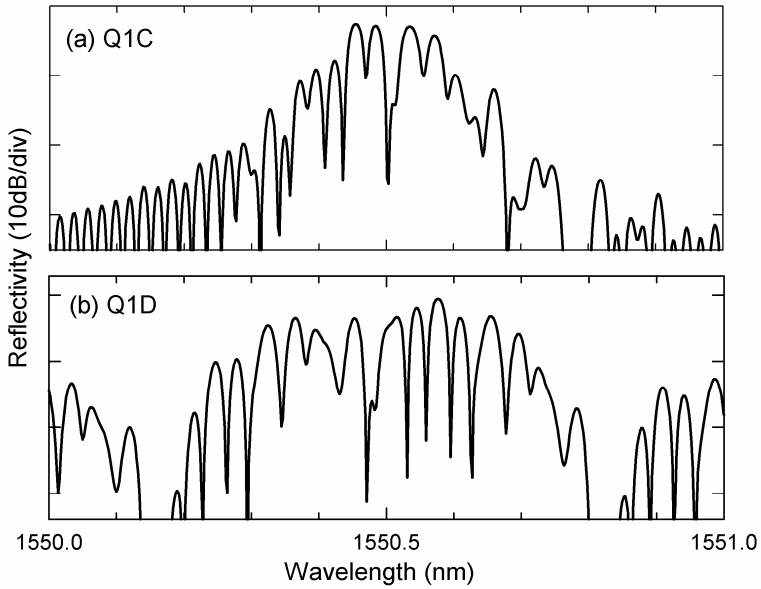

Fig.6.3 Simulated reflection spectra of (a) continuous-phase encoders Q1C and (b) discrete-phase encoder Q1D.

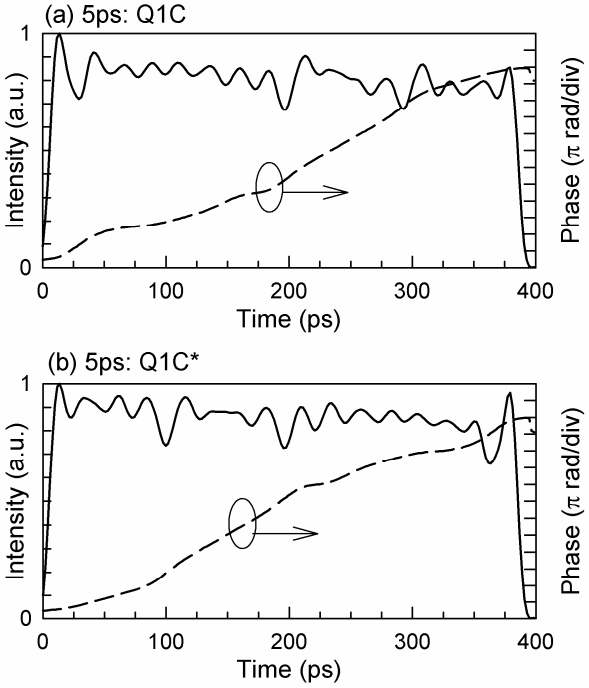

Fig.6.4 Simulated intensities (solid lines) and phases (dashed lines) of pulse responses of continuous-phase (a) encoder Q1C and (b) decoder Q1C* (the input pulse width is 5ps).

Shown in Fig.6.5 are the simulated decoding pulses as the encoder is Q1C or Q2C, and the decoder is Q1C* or Q2C*, when the input pulse width is 5ps. The central wavelength of input optical pulses is tuned to the central wavelength of en/decoding FBGs in the simulation.

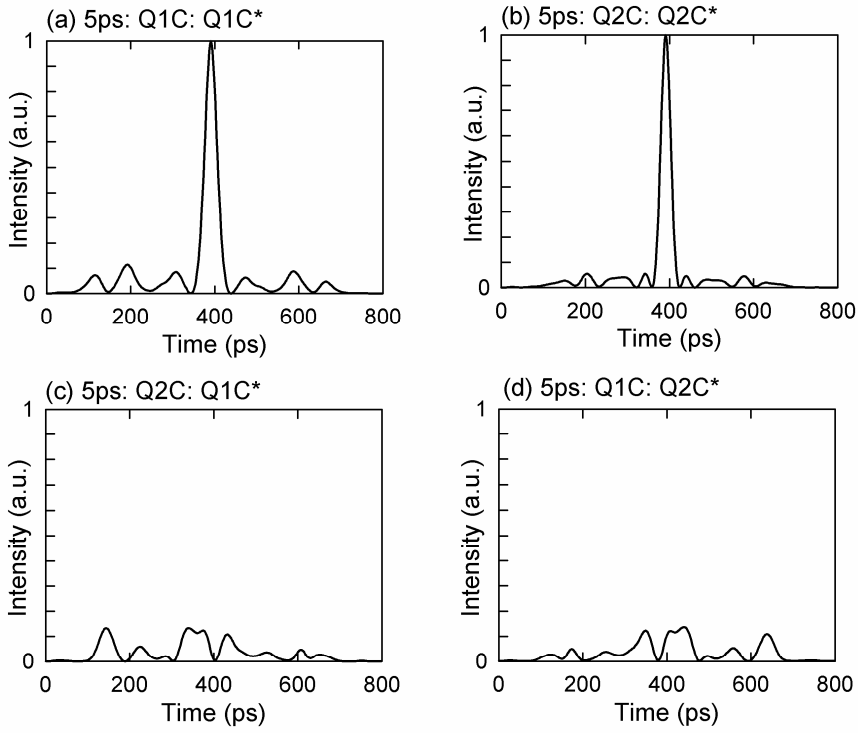

Fig.6.5 Simulated autocorrelation (a) Q1C: Q1C*, (b) Q2C: Q2C*, and crosscorrelation (c) Q2C: Q1C*, (d) Q1C: Q2C* (the input pulse width is 5ps).

6.3.2 Comparing three system configurations

To evaluate the performances of continuous-phase en/decoders, we compare the following three OCDMA systems: (a) discrete-phase encoders and decoders, (b) discrete-phase encoders and continuous-phase decoders, or (c) continuous-phase encoders and decoders. In these systems, Q1C, Q2C, Q1C* and Q2C* are used as continuous-phase en/decoders, and Q1D, Q2D, Q1D* and Q2D* are used as discrete-phase en/decoders. Chip number, chip length, and effective index modulation of all these en/decoders are respectively 16, 2.5mm, and 1.0×10^{-5}. The input pulse width is 5-ps.

The auto and cross correlation pulses were simulated, and are shown in Fig. 6.6. Based on comparing the ratio between the peak of cross and auto correlation (RPCA), we find that configuration (a) has the best performance, although only marginally better when compared with (c). The better performance of configuration (c) over (b) is due to the fact

that the spatial phases of encoders and decoders in (c) are both continuous and can therefore match completely. A special advantage of configuration (c) over (a) is that the continuous-phase devices can be achieved with the capacity of dynamic reconfiguration considering that the reconfigurable-phase devices have the same spatial phase distribution as continuous-phase device.

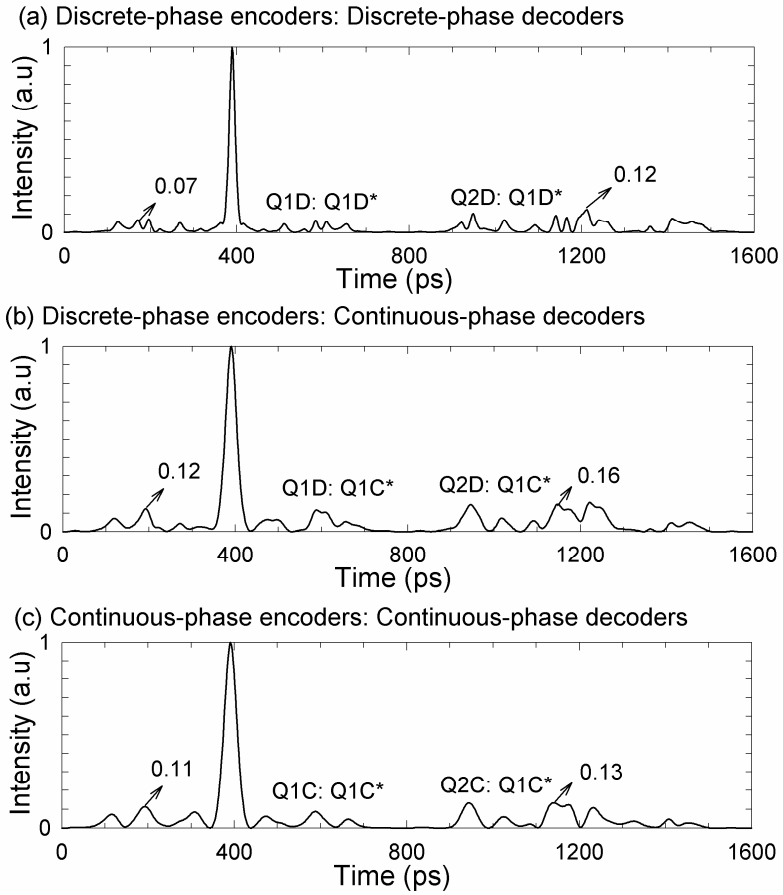

Fig.6.6 Simulated auto and cross correlation pulses for configuration (a) discrete-phase encoders and decoders, (b) discrete-phase encoders and continuous-phase decoders, and (c) continuous-phase encoders and decoders.

The relatively low RPCA value for all these systems, while not acceptable in a real system, is because of the small chip number we choose in the simulation. As shown in Chapter 4, it can be improved significantly by using a larger chip number.

6.3.3 Tolerance to the input pulse width

For further comparisons, the system performances of configurations (a) and (c) are simulated under different input pulse-widths. The resultant RPCA's are summarized in Fig.6.7. We can see that the systems using the continuous-phase encoders and decoders

are more tolerant to longer pulse-widths. This can be explained by the fact that the reflection spectrum of the continuous-phase device is narrower than that of the discrete-phase device, which has been shown in Fig. 6.3. This also suggests the potential of bandwidth saving, and this could facilitate the combination of an OCDMA system with WDM techniques.

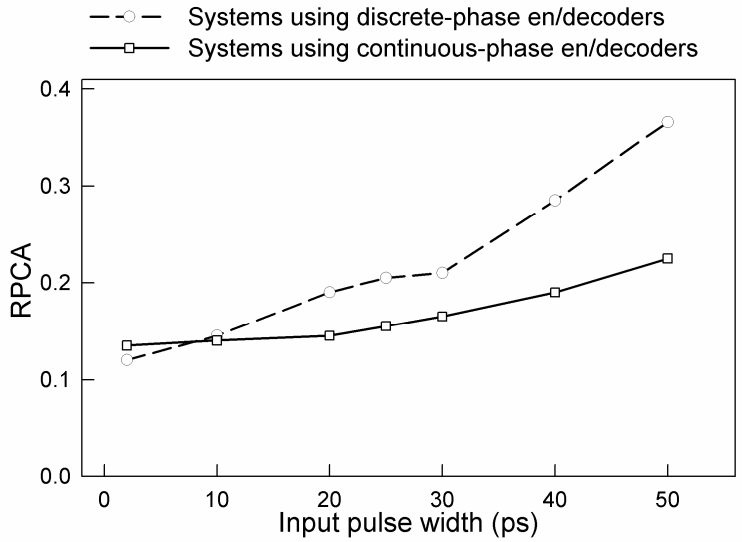

Fig.6.7 Simulated RPCA's for systems using continuous or discrete-phase en/decoders for different input pulse widths.

6.4 Experiments and results

6.4.1 Device fabrication and characterization

In the following experiments, we will use discrete-phase en/decoders (Q1D, Q2D, Q1D* and Q2D*), reconfigurable-phase en/decoders (Q1R, Q2R, Q1R* and Q2R*), and continuous-phase en/decoders (Q1C, Q2C, Q1C* and Q2C*). The designations and parameters of discrete-phase en/decoders and reconfigurable-phase en/decoders are the same as those described in Section 5.5.

The Bragg wavelength, index modulation, chip length, and total length of continuous-phase en/decoders (Q1C, Q2C, Q1C* and Q2C*) are respectively 1550.5nm, 2.2×10^{-5}, 2.5mm and 40mm, which are the same as the parameters of discrete-phase en/decoders and reconfigurable-phase en/decoders shown in Section 5.5.

The continuous-phase en/decoders are also fabricated using the continuous grating writing technique [36], which uses a phase mask with a uniform pitch and relies on precise control of the position of the fibre relative to the phase mask to achieve gratings with complex profiles. The effective dc refractive index variation, δn_{dc}, in the continuous-

phase en/decoders is achieved by chirping the Bragg wavelength, λ_B, (according to the equation $\delta n_{dc} = \frac{\delta\lambda_B}{\lambda_B} n_{dc}$). From the dc refractive index distribution in continuous-phase encoders Q1C and Q2C (shown in Fig.6.2), the Bragg wavelength variations along them are calculated and shown in Fig. 6.8.

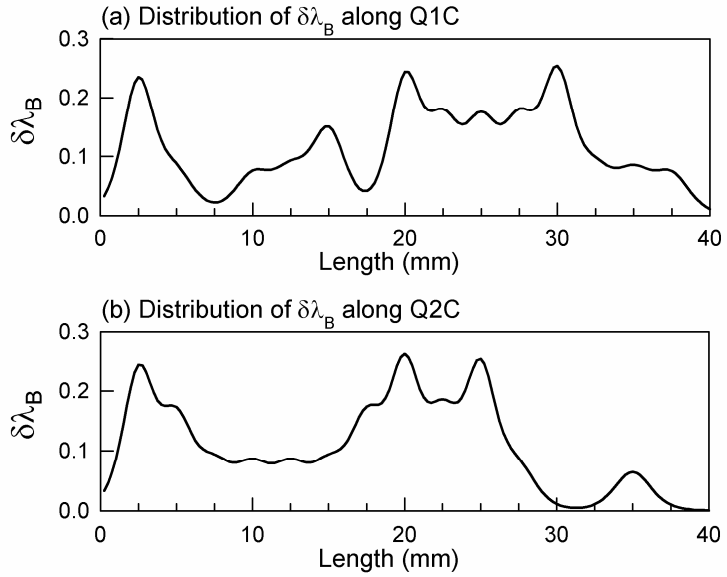

Fig.6.8 Bragg wavelength variations of (a) Q1C and (b) Q2C.

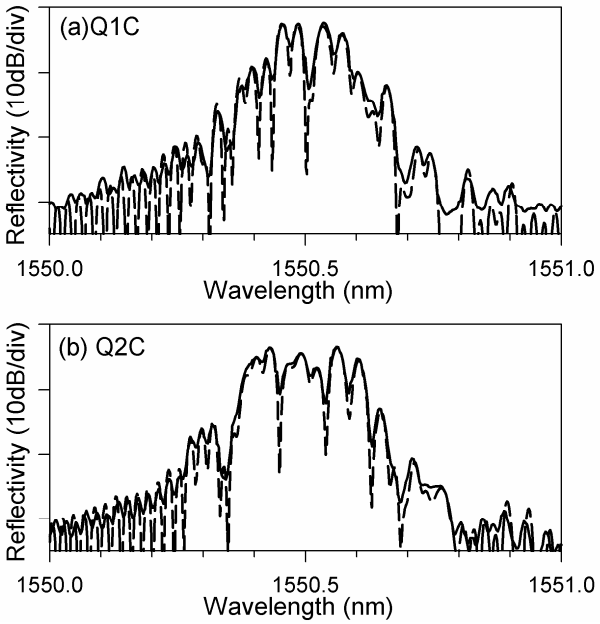

Fig.6.9 Measured (solid lines) and simulated (dashed lines) reflection spectra of continuous-phase encoders (a) Q1C and (b) Q2C.

Shown in Fig. 6.9 are the measured (solid lines) and simulated (dashed lines) reflection spectra of continuous-phase-encoders Q1C and Q2C. There is clearly good agreement

between the measurement and simulation results although the grating structures are very complex. Note that the reflection spectra of continuous-phase-encoders Q1C and Q2C are almost the same as those of reconfigurable-phase-encoders Q1R and Q2R (shown in Fig.5.15). This is due to the fact that they are designed to have the same spatial phase distributions. If we compare the reflection spectrum of Q1C (or Q2C) and Q1D (or Q2D), it is evident that, for the same nominal address code, the reflection spectrum of a continuous-phase-encoder (or reconfigurable-phase-encoder) has narrower bandwidth than that of a discrete-phase-encoder and that it has much lower spectral features away from the main band, which could assist its use in a WDM configuration.

6.4.2 Systems using continuous-phase encoders and decoders

In the first system test, we use continuous-phase devices as both encoders (Q1C and Q2C) and decoders (Q1C* and Q2C*). The experimental setup is similar to that shown in Fig.5.16. A gain-switched semiconductor laser diode, operating at 1550.5 nm, generates ~5 ps pulse sequences with a repetition rate of 311 MHz. This pulse train is split by a 3dB coupler into two parts, each reflected from the continuous-phase encoders Q1C and Q2C respectively, and then combined by another 3dB coupler. A fibre delay line controls the timing of the signals from the two encoding gratings. Then the combined signal is reflected from the continuous-phase decoders Q1C* or Q2C*. The decoded pulses are detected using a 20GHz photodiode and fed into a fast sampling oscilloscope.

The measured encoding pulses by Q1C and Q2C are shown in Fig.6.10. The measured decoding pulses (auto- and cross correlation), for the decoders Q1C* or Q2C*, are shown in Fig. 6.11. The measured RPCA is ~20%.

We also measure the system using the discrete-phase encoders (Q1D, Q2D) and decoders (Q1D*, Q2D*) and the results are shown in Fig.6.12. In this case, the measured RPCA is also ~20%. By comparing the RPCA, we can see that the systems using the continuous-phase encoders and decoders exhibit a similar performance as that using the discrete-phase encoders and decoders. The advantages of continuous-phase devices are that they have a more relaxed requirement in the encoding input pulse width and therefore will occupy a narrower bandwidth. This has already been analysed in Section 6.3.3.

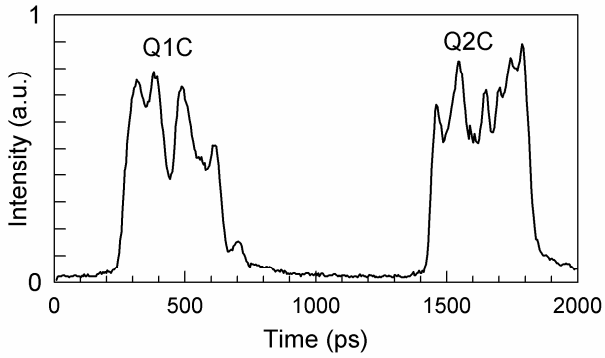

Fig.6.10 Measured encoding pulses by Q1C and Q2C.

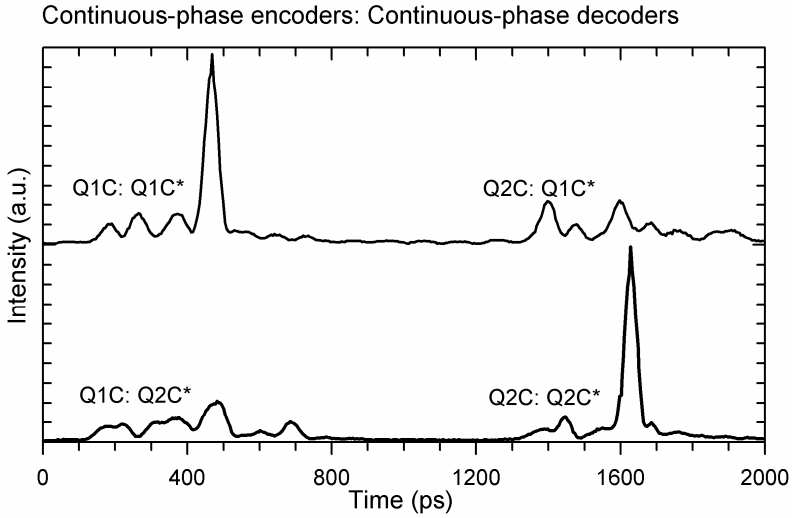

Fig.6.11 Measured decoding pulses (auto- and cross correlation) when the encoders are Q1C and Q2C, the decoder is Q1C* or Q2C*.

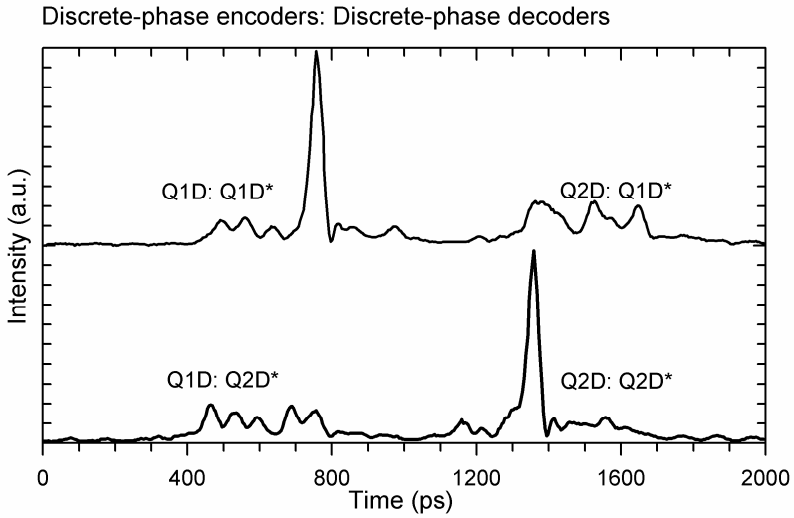

Fig.6.12 Measured decoding pulses (auto- and cross correlation) when the encoders are Q1D and Q2D, the decoder is Q1D* or Q2D*.

6.4.3 Systems using continuous-phase encoders and reconfigurable-phase decoders

The continuous-phase devices are designed to match the phase profiles of reconfigurable-phase devices. Here, we measure the system using the continuous-phase devices as encoders (Q1C, Q2C) and reconfigurable-phase devices as decoders (Q1R*, Q2R*), (Fig.6.13). The input pulse width is also ~5ps. The measured RPCA is ~23%. In Section 6.3.2, we have demonstrated by simulation that continuous-phase encoders can match better with reconfigurable decoders compared with the discrete-phase encoders.

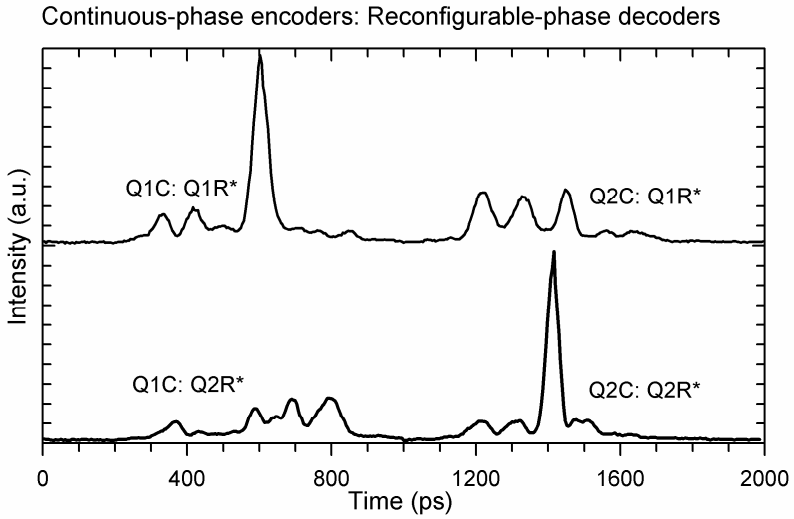

Fig.6.13 Measured decoding pulses (auto- and cross correlation) when the continuous-phase encoders (Q1D and Q2D) and reconfigurable-phase decoder (Q1D* or Q2D*) are used.

6.5 31-chip, continuous-phase OCDMA en/decoders

6.5.1 Device parameters and characterization

From the family *A* sequences, four 31-bit quaternary codes P1, P2, P3 and P4 are chosen, as shown in Fig.6.14. With these code sequences, four continuous-phase encoders are designed based on the single-phase distribution shown in Fig.6.1. The chip length is still 2.5mm, and therefore, the total length of FBG en/decoders is 77.5mm. The resultant dc refractive index variations of 31-chip continuous-phase encoders P1, P2, P3 and P4 are shown in Fig.6.15.

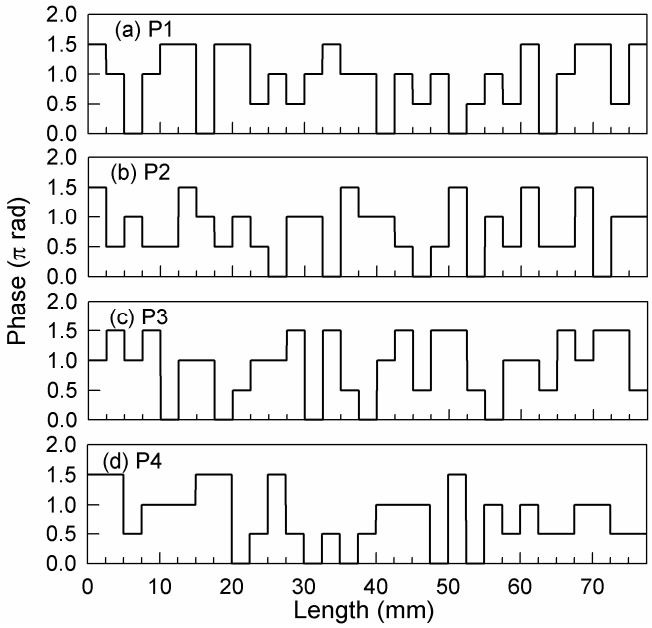

Fig.6.14 Quaternary code sequences (a) P1, (b) P2, (c) P3 and (d) P4.

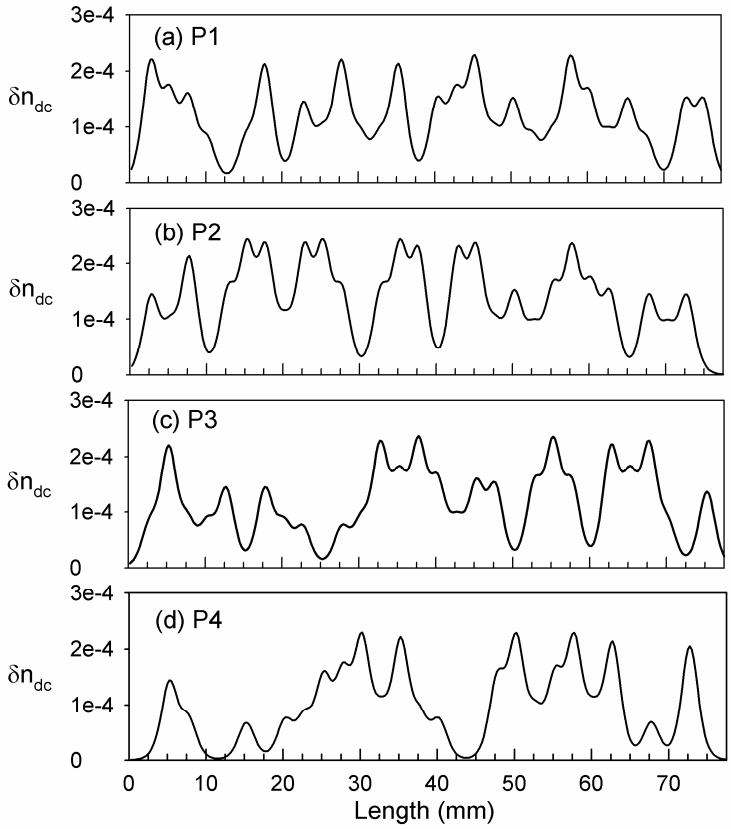

Fig.6.15 dc refractive index variations of continuous-phase encoders (a) P1, (b) P2, (c) P3 and (d) P4.

The continuous-phase en/decoders P1, P2, P3, P4, P1*, P2*, P3*, and P4* are fabricated using continuous grating writing techniques. The effective dc refractive index

variation, δn_{dc}, is also achieved by chirping the Bragg wavelength. By annealing the FBGs after fabrication, the index modulation of all these FBGs are controlled to be ~1.0×10^{-5}, and their peak reflectivity is less than 50%.

Shown in Fig. 6.16 are the measured (solid lines) and simulated (dashed lines) reflection spectra of continuous-phase-encoders P1, P2, P3 and P4. The measurement roughly agrees with the simulation result, although the grating structures are very complex. As shown before, the reflection spectra of the continuous-phase encoders (or reconfigurable-phase-encoders) are narrower than those of the discrete-phase encoders with same nominal code sequences. The 20dB bandwidth of the reflection spectra of the 31-chip en/decoders is less than 0.4nm.

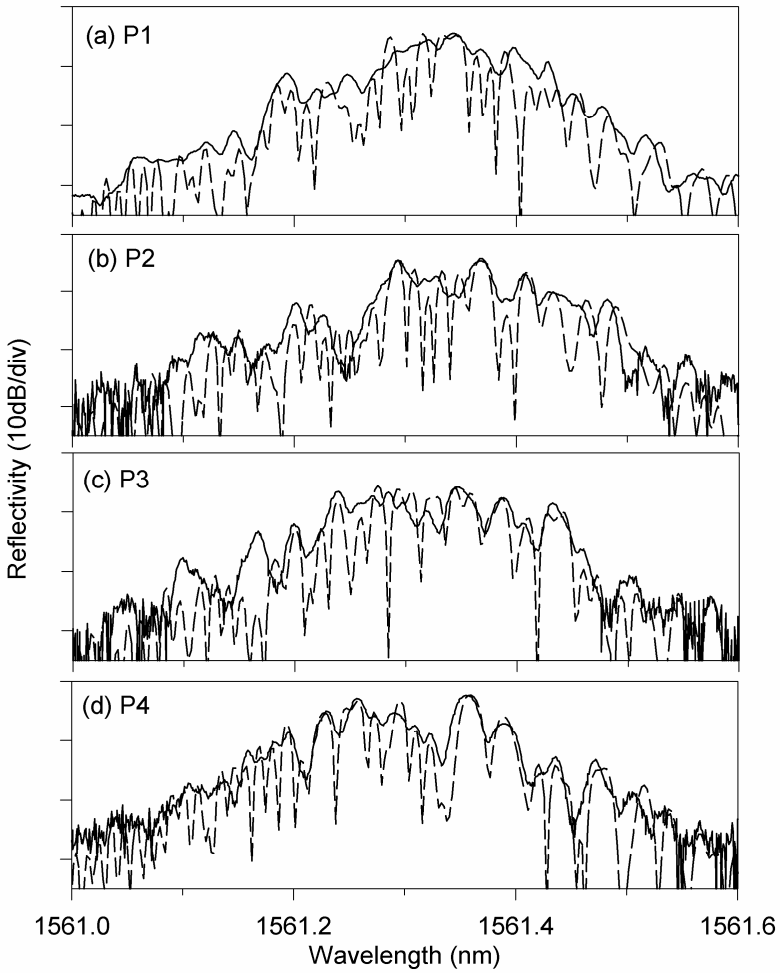

Fig.6.16 Measured (solid lines) and simulated (dashed lines) reflection spectra of continuous-phase-encoders (a) P1, (b) P2, (c) P3 and (d) P4.

We also fabricate 31-chip reconfigurable-phase decoders by putting 30 tungsten wires 2.5mm apart along a uniform FBG with a length of 77.5mm. The diameter of tungsten wires is 50μm. By varying the electrical currents passing through the tungsten wires, the

phase codes on the FBG could be controlled. The phase distribution in a reconfigurable-phase en/decoder is the same as that in a continuous-phase en/decoder for the same nominal code sequence. P1R, P2R, P3R and P4R are used to designate the reconfigurable-phase encoders with code sequences of P1, P2, P3, and P4 respectively.

6.5.2 Device performances

Correlation performances of the 31-chip continuous-phase OCDMA en/decoders are measured using a 50ps optical pulse train as the input. In the measurement, the central wavelength of input optical pulses is tuned to the central wavelength of the en/decoders. Shown in Fig. 6.17 are the measured autocorrelation (P2: P2*, P3: P3*) and cross-correlation pulses (P2: P3*, P4: P3*) when both the encoders and decoders are fixed-code continuous-phase devices. Shown in Fig. 6.18 are the measured autocorrelation (P2: P2R*, P3:P3R*) eye diagrams when the fixed-code continuous-phase encoders and reconfigurable-phase decoders are used.

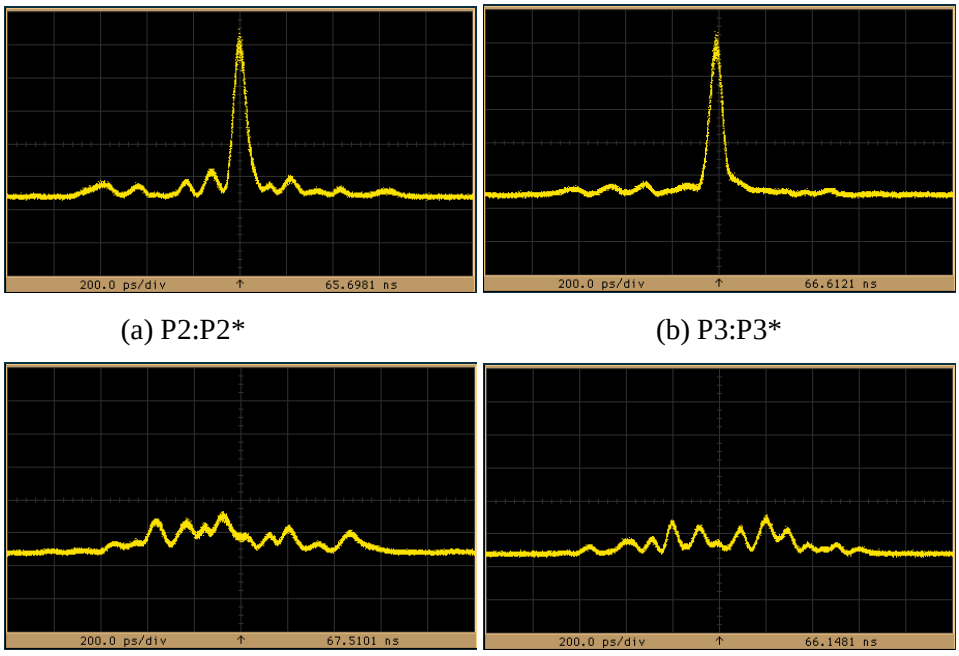

(a) P2:P2* (b) P3:P3*

(c) P2: P3* (d) P4:P3*

Fig.6.17 Measured autocorrelation pulses (a) P2: P2*, (b) P3:P3* and cross-correlation pulses (c) P2: P3*, (d) P4: P3*.

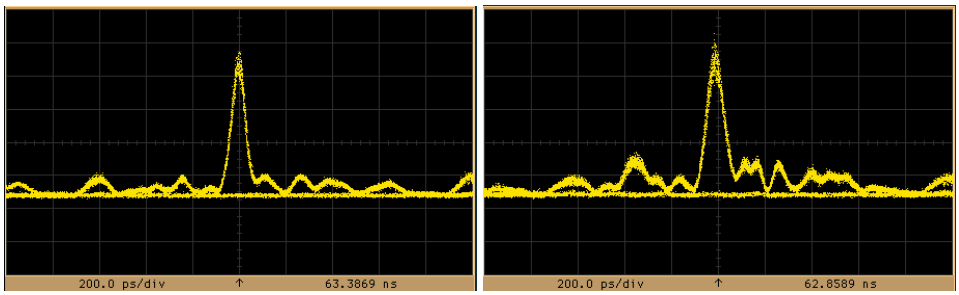

(a) P2: P2R* (b) P3:P3R*

Fig.6.18 Measured eye diagrams for (a) P2: P2R*, and (b) P3:P3R*.

6.5.3 A 16-channel OCDMA/DWDM system

Based on the 31-chip continuous-phase and reconfigurable-phase OCDMA en/decoders described above, a 16-channel OCDMA/DWDM system has been demonstrated. The setup is shown in Fig.6.19. Four cw lasers with a channel spacing of 0.4nm are combined and fed into an electro-absorption modulator driven at 5GHz, generating four 5GHz, 50ps WDM pulse trains. The pulse trains are modulated using a $LiNbO_3$ intensity modulator to obtain a data with a bit rate of 625Mbit/s. The modulated pulses are then reflected from an array of 16 continuous-phase encoders to generate encoding data from an effective 16 users. The encoders array is composed of four different codes (P1-P4), each code being repeated on each of four different central wavelengths ($\lambda 1$ to $\lambda 4$). All 16 coded channels are combined together prior to transmission, amplification and detection. At the receiver end, a fixed-code continuous-phase or a reconfigurable-phase decoder is used.

For each single OCDMA decoder, twelve out-of-band channels are filtered out due to the inherent wavelength selectivity of the decoding grating. Of the remaining four in-band channels, only the code matched to the decoding grating generates a distinct autocorrelation peak, while the other three unmatched channels produce cross correlation signals. Error-free performance is achieved for all these channels using the 31-chip continuous-phase or reconfigurable-phase OCDMA decoders. The details of the system performance are reported in [156].

This system exploits the narrow-bandwidth characteristics of continuous-phase en/decoders. For the same nominal address codes, the reflection spectra of continuous-phase en/decoders (or reconfigurable-phase en/decoders) are narrower than those of discrete-phase en/decoders. If discrete-phase en/decoders are used [157], WDM with 0.4

nm wavelength spacing is impossible because the bandwidth for the discrete-phase en/decoders with the same code sequences is much more than 0.4nm.

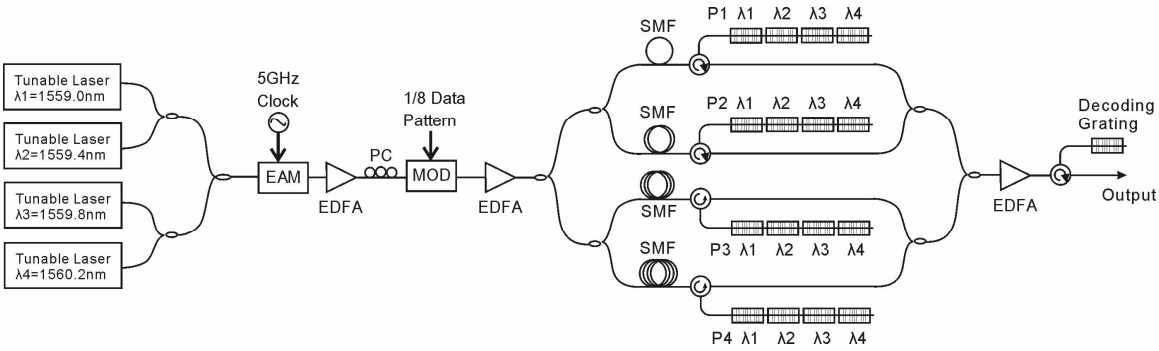

Fig.6.19 Experimental setup for the 16-channel OCDMA/DWDM system [156].

6.6 Conclusions

We have proposed and demonstrated a novel OCDMA en/decoder with a continuous phase-distribution based on FBGs. The phase profile of this device is designed to match that of a reconfigurable-phase en/decoder accurately, so it inherently suits the application in reconfigurable OCDMA systems.

We compare OCDMA systems with three different configurations: (a) discrete-phase encoders and decoders, (b) discrete-phase encoders and continuous-phase decoders, or (c) continuous-phase encoders and decoders. Configuration (a) has the best performance, although only marginally when compared with (c), while configuration (c) has a far better performance over (b) due to the complete phase-matching. Configuration (c) can also be achieved with the capacity of dynamic reconfiguration since the reconfigurable-phase devices have the same phase distribution as continuous-phase devices. Furthermore**,** the continuous-phase en/decoders have a narrower bandwidth compared with conventional discrete-phase devices with the same nominal code sequences. Therefore, they are more tolerant to input pulse-width and have the advantage of bandwidth saving.

Continuous-phase, reconfigurable-phase, and discrete-phase en/decoders are fabricated and their performances are tested and compared in a 16-chip OCDMA system. In addition, we built 31-chip continuous-phase and reconfigurable-phase OCDMA en/decoders, through which a 16-channel OCDMA/DWDM system with a WDM channel spacing of only 0.4nm was demonstrated. This system exploits the narrow-bandwidth characteristics of the new continuous-phase en/decoders.

Chapter 7

Dispersion tuning of fibre Bragg gratings using the S-bending technique

7.1 Introduction

Compensating chromatic dispersion in fibre systems using chirped fibre Bragg gratings (CFBG) is one of the most important applications of FBGs [71]. Compared with dispersion compensating fibre (DCF), a short CFBG could provide a large amount of dispersion. Another advantage of CFBGs is their tunability, because the Bragg wavelengths of FBGs are sensitive to, and can be controlled by temperature or strain.

If a variable linear temperature or strain field is applied along a linearly chirped FBG, the FBG will still have a linear chirp in its pitch, but its bandwidth and therefore dispersion can be controlled by the applied temperature or strain gradient. A variable linear temperature field along a grating can be achieved by controlling the temperature at both ends of the grating [158], and a variable linear strain field can be produced by using the S-bending technique [159], which is the topic of this Chapter. By embedding a chirped FBG in a uniform beam and bending the beam in an S-shape, a variable linear strain gradient is produced and applied along the FBG, and the grating dispersion can then be controlled.

This Chapter is organized as follows. In Section 7.2, dispersion in fibres, dispersion compensation and dynamic dispersion compensation techniques based on chirped FBGs are reviewed. In Section 7.3, the S-bending technique is analyzed and dispersion tuning devices based on S-bending are described. Based on S-bending techniques, two novel devices, including a tunable dispersion compensator with an enhanced dispersion tuning range and a tunable pure dispersion slope compensator, are reported in Section 7.4 and

7.5 respectively. Applications of tunable dispersion in controlling the pulse width of a soliton fibre laser are demonstrated in Section 7.6.

7.2 Dispersion, dispersion compensation and dynamic dispersion compensation

7.2.1 Dispersion in optical fibres

The variation of refractive index with frequency constitutes the phenomenon of dispersion [160]. For a single mode fibre waveguide, the propagation characteristics are determined by the mode propagation constant, so the dispersion of the fibre can be defined to be the variation of propagation constant with frequency.

The total dispersion of single mode fibres arises from two mechanisms [161]: material dispersion and waveguide dispersion. Material dispersion occurs because the mode propagation constant is related to the refractive indices of the core and cladding materials, which are dependent on frequency. Waveguide dispersion is due to the fact that the mode confinement in a waveguide causes its mode propagation constant to depend on frequency.

In mathematics, the mode propagation constant $\beta(\omega)$ can be expanded into a Taylor series at the central frequency ω_0 [162],

$$\beta(\omega) = n(\omega)\frac{\omega}{c} = \beta_0 + \beta_1(\omega-\omega_0) + \frac{1}{2}\beta_2(\omega-\omega_0)^2 + \frac{1}{6}\beta_3(\omega-\omega_0)^3 + \cdots \tag{7.1}$$

where

$$\beta_m = \left(\frac{d^m\beta}{d\omega^m}\right)_{\omega=\omega_0} \qquad \text{(m = 0, 1, 2, 3, …)} \tag{7.2}$$

The first three parameters β_1, β_2 and β_3 are respectively group delay parameter, group delay dispersion (GVD) parameter, and third order dispersion (TOD) parameter. Their units are ps·km^{-1}, ps^2·km^{-1}, and ps^3·km^{-1} respectively.

The group delay τ_g for a light pulse propagating along a unit length of fibre is the inverse of the group velocity v_g. Hence [161],

$$\tau_g = \frac{1}{v_g} = \frac{1}{d\omega/d\beta} = \frac{d\beta}{d\omega} = \beta_1 . \tag{7.3}$$

The unit of group delay τ_g is ps·km^{-1}.

The group delay dispersion or second order dispersion, D, is given by the derivative of the group delay with respect to the vacuum wavelength λ as:

$$D = \frac{d\tau_g}{d\lambda} = -\frac{\omega}{\lambda}\frac{d^2\beta}{d\omega^2} = -\frac{2\pi c}{\lambda^2}\beta_2 . \tag{7.4}$$

In the second equality, Eq. (7.3) and the relation $d\lambda = -\frac{\lambda^2}{2\pi c}d\omega$ are used. The unit of second order dispersion D is ps·nm^{-1}·km^{-1}.

The third order dispersion or dispersion slope, S, is used to characterize the variation of the second order dispersion with wavelength and may be written as,

$$S = \frac{dD}{d\lambda} = \frac{(2\pi c)^2}{\lambda^4}\frac{d^3\beta}{d\omega^3} + \frac{4\pi c}{\lambda^3}\frac{d^2\beta}{d\omega^2} = \frac{(2\pi c)^2}{\lambda^4}\beta_3 + \frac{4\pi c}{\lambda^3}\beta_2 . \tag{7.5}$$

In the second equality, Eq. (7.4) and the relation $d\lambda = -\frac{\lambda^2}{2\pi c}d\omega$ are used. The unit of third order dispersion S is ps·nm^{-2}·km^{-1}.

Usually, if the group velocity of the propagating light is an increasing function of the wavelength, the dispersion is said to be normal [160]. Conversely, if the group velocity is a decreasing function of the wavelength, the dispersion is said to be anomalous dispersion. So, if $D < 0$ ($\beta_2 > 0$), we say that the fibre operates in the normal dispersion region, and if $D > 0$ ($\beta_2 < 0$), we say that the fibre operates in the anomalous dispersion region.

In fibres, RDS is defined as the ratio of dispersion slope to second order dispersion at any given wavelength. The dispersion-related parameters of some commercial transmission fibres are shown in Table 7.1 [163].

Table 7.1 Dispersion parameters of common transmission fibres

	Dispersion (ps·nm^{-1}·km^{-1}) @ 1550nm	Dispersion slope (ps·nm^{-2}·km^{-1}) @ 1550nm	RDS
Standard SMF	17	0.058	0.0034
LEAF	4.2	0.085	0.0202
True Wave-RS	4.5	0.045	0.0100

7.2.2 Dispersion effects and compensation techniques

When an optical pulse transmits in fibres, due to dispersion, different spectral components of the pulse will transmit at a different velocity and, as a result, the final pulse shape will be different from the original one.

Neglecting the fibre loss and nonlinear effects, and considering the second and third order dispersion, the transmission equation of the optical pulse in a single mode fibre can be derived to be [162],

$$i\frac{\partial U(z,T)}{\partial z}=\frac{\beta_2}{2}\frac{\partial^2 U(z,T)}{\partial T^2}+\frac{i}{6}\beta_3\frac{\partial^3 U(z,T)}{\partial T^3} \tag{7.6}$$

where, $U(z,T)$ is the normalized amplitude of the optical pulse. By the Fourier theory, this equation can be transformed into the frequency domain,

$$\tilde{U}(z,\omega)=\tilde{U}(0,\omega)\exp\left(\frac{i}{2}\beta_2\omega^2 z\right)\exp\left(\frac{i}{6}\beta_3\omega^3 z\right) \tag{7.7}$$

where, $\tilde{U}(z,\omega)$ and $\tilde{U}(0,\omega)$ are the Fourier transform of $U(z,T)$ and $U(0,T)$ respectively. According to Eq. (7.7), we can regard $\exp\left(\frac{i}{2}\beta_2\omega^2 z\right)$ and $\exp\left(\frac{i}{6}\beta_3\omega^3 z\right)$ respectively as the transfer function of second order and third order dispersion of single mode fibres.

In a high-bit-rate transmission system, the broadening of optical pulses due to second and third order dispersion is a limiting factor. This is due to the fact that the broadening of the optical pulses makes reconstruction of the ‘ones’ and ‘zeros’ in the data sequence less certain, leading to errors. From Eq. (7-7), we can see that the dispersion tolerance is roughly proportional to the inverse of the square of the bit-rate. Usually, the amount of residual dispersion one can accommodate is of the order of 1000ps/nm for 10 Gbit/s systems, and only of the order of 60ps/nm and 4ps/nm for 40Gbit/s and 160Gbit/s systems respectively [164]. Practical transmission fibres have a small, but nonzero, dispersion slope. In high-bit-rate, multiple-channel, or long-haul transmission systems, the third-order-dispersion must also be considered and compensated.

Single mode dispersion compensating fibres (SM-DCF) are widely used to compensate the dispersion in fibres. Transmission fibres usually have a positive dispersion $(D>0)$, so, SM-DCFs, which exhibit a negative dispersion through their special waveguide structure, are widely used to cancel the positive dispersion. As an all-fibre device, SM-DCF is inherently broadband, and has low loss and low non-uniformity. The RDS value can also

be designed to cancel the dispersion slope of the transmission fibre simultaneously. However, SM-DCF has some disadvantages. Firstly, SM-DCF with a length of 1km can only compensate the dispersion of 8~10 km standard SMF. Secondly, the loss of SM-DCF is relatively high ($\alpha \approx 0.5dB/km$). Thirdly, the SM-DCFs, especially those with a high RDS value, have very small effective areas, which will decrease the input power threshold for nonlinear effects.

Various other techniques have been developed to achieve dispersion and dispersion slope compensation. They include higher-order-mode dispersion compensation fibres (HOM-DCF) [165-166], virtually imaged phased arrays (VIPA) [167-168], planar waveguide Mach-Zehnder lattice filters [169-171], planar waveguide ring resonator all-pass filters [172-174], and Gires-Tournois etalon all-pass filters [175-176].

7.2.3 Chirped fibre Bragg gratings as dispersion compensators

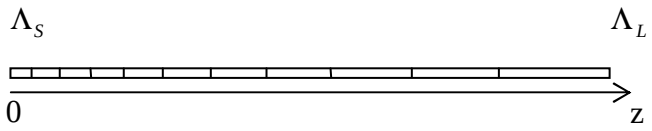

Fig.7.1 Schematic of a chirped FBG.

Chirped FBGs, with an increasing or decreasing Bragg wavelength along the length, are also very useful for dispersion compensation. Fig.7.1 shows a schematic of a chirped FBG with a length of L, and the shortest and longest grating period Λ_S and Λ_L correspond to the Bragg wavelength λ_S and λ_L respectively. The chirp bandwidth is $\Delta\lambda = \lambda_L - \lambda_S$.

The reflection time delay from a chirped grating is a function of wavelength. Light entering into a linearly chirped FBG (LCFBG) suffers a time delay

$$\tau(\lambda) = \frac{(\lambda - \lambda_S)}{(\lambda_L - \lambda_S)} \frac{2n_{eff} L}{c} \qquad (\lambda_S < \lambda < \lambda_L) \tag{7.8}$$

where c is the light speed in the vacuum. The dispersion of the linearly chirped grating is

$$D(\lambda) = \frac{d\tau(\lambda)}{d\lambda} = \frac{1}{(\lambda_L - \lambda_S)} \frac{2n_{eff} L}{c} \qquad (\lambda_S < \lambda < \lambda_L) \tag{7.9}$$

For a second-order nonlinearly chirped grating, the time delay is,

$$\tau(\lambda) = \frac{(\lambda - \lambda_S)^2}{(\lambda_L - \lambda_S)^2} \frac{2n_{eff} L}{c} \qquad (\lambda_S < \lambda < \lambda_L) \tag{7.10}$$

and the resultant dispersion is,

$$D(\lambda)=\frac{d\tau(\lambda)}{d\lambda}=\frac{2(\lambda-\lambda_S)}{(\lambda_L-\lambda_S)^2}\frac{2n_{eff}L}{c} \qquad (\lambda_S<\lambda<\lambda_L) \tag{7.11}$$

The time-delay characteristic of a linearly or second-order nonlinearly chirped FBG is shown in Fig 7.2. Chirped FBGs have the following characteristics as dispersion compensators. Firstly, the time delay, and dispersion of a chirped FBG scale with the grating length. Therefore, a long grating is needed to compensate a large dispersion. Secondly, a chirped FBG can compensate positive or negative dispersion, depending on which end the light is incident from. Thirdly, a chirped FBG with a higher-order chirp can compensate higher-order dispersion, but it will also exhibit lower-order dispersion. For example, the FBG with a second-order nonlinear chirp will exhibit third order and second order dispersion simultaneously. This is because the time delay of any chirped gratings can only change monotonically with respect to the wavelength [177]. However, it is still possible to obtain pure higher order dispersion by cascading several FBGs or by using an SSFBG [76].

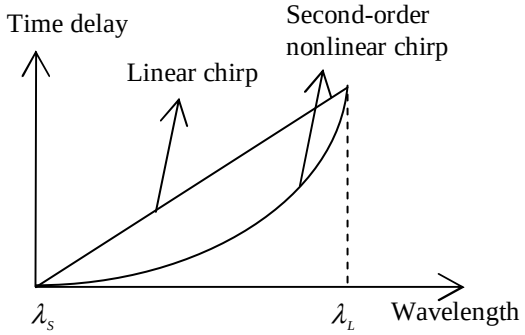

Fig.7.2 Time delay characteristics of FBG with a linear or second-order nonlinear chirp.

7.2.4 Dynamic dispersion or dispersion slope compensation using fibre Bragg gratings

In a high-bit-rate transmission system, the dispersion tolerance becomes so small that even a tiny variation in dispersion can severely influence the network performance. In such a system, the amount of dispersion may vary in time because of several potential impairments [178]. Firstly, small variations in optical power can result in an additional phase-shift, which can modify the optimal dispersion map of the system. Secondly, a dynamic reconfiguration of the network can change the total accumulated dispersion. Thirdly, transmission conditions may change simply because of environmental variations,

such as changes in ambient temperature [179]. Therefore, systems operating at a high bit-rate, such as 40Gbit/s or 160Gbit/s, will require dynamic dispersion compensation.

FBGs have the unique capacity for dynamic dispersion management in contrast to conventional dispersion compensation fibres. The tunability of dispersion arises from the grating response to temperature or strain, which has been reviewed in Section 2.5.3.

In principle, there are two ways to implement a tunable dispersion compensator using a fibre Bragg grating: (a) a second-order nonlinearly-chirped FBG (NCFBG) plus a variable uniform strain or temperature field [180], or (b) a linearly-chirped FBG (LCFBG) or a uniform FBG plus a variable linear strain or temperature field [159] [178][181-185]. The conceptual diagrams for these two configurations are shown in Fig.7.3.

Similarly, there are three ways to implement a tunable dispersion slope compensator using a fibre Bragg grating: (a) a third-order nonlinearly-chirped FBG plus a variable uniform strain or temperature field [186-187], (b) a second-order nonlinearly-chirped FBG plus a variable linear strain or temperature field, or (c) a linearly-chirped FBG or a uniform FBG plus a variable high-order nonlinear gradient strain or temperature field [188-193]. The conceptual diagrams for configurations (a) and (b) are shown in Fig.7.4, and the conceptual diagram for configuration (c) is similar to configuration (b).

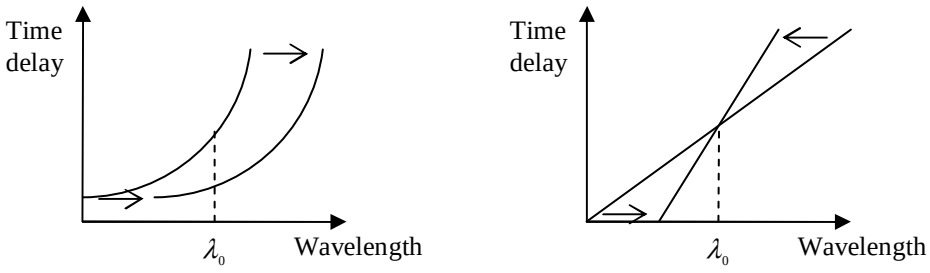

(a) A second-order nonlinearly chirped FBG plus a uniform field

(b) A linearly chirped FBG plus a linear field

Fig.7.3 Conceptual diagram of a dynamic dispersion compensator.

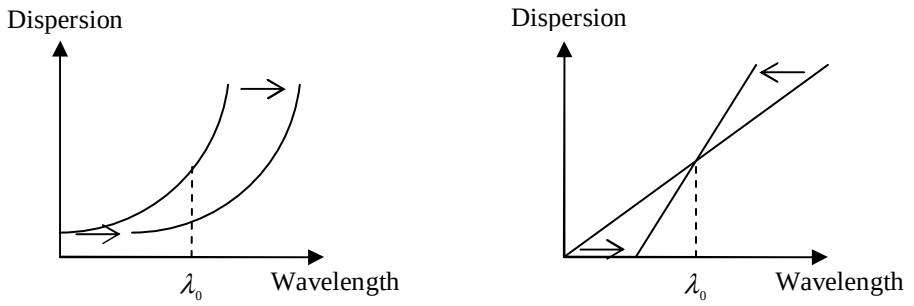

(a) A third-order nonlinearly chirped FBG plus a uniform field

(b) A second-order nonlinearly chirped FBG plus a linear field

Fig.7.4 Conceptual diagram of a dynamic TOD compensator.

A variable uniform strain or temperature field could be easily achieved, usually by means of a uniform stretch/compression or a temperature controller. But devices based on a uniform field are always accompanied by a central wavelength shift during tuning (as shown in Fig.7.3 (a) and Fig.7.4 (a)), which is undesirable for practical applications.

A variable linear strain or temperature field is relatively easy to implement and its advantage is that the central wavelength of FBGs does not shift while tuning, as shown in Fig.7.3 (b) and Fig.7.4 (b). A variable linear temperature field can be achieved by using two separate temperature controllers, each on one side of the grating. A variable strain field can be achieved using an S-bending tuning technique, the details of which will be described in next section.

A high-order nonlinear strain gradient can be obtained by bending a linearly tapered beam and, a high-order temperature gradient can be achieved through a series of divided heaters. Both of these solutions are rather complicated.

7.3 Dispersion tuning of fibre Bragg gratings by the S-bending technique

7.3.1 Basics of bending techniques

To introduce the S-bending technique, basics of bending [194] are described in this sub-section.

A. Stress-strain relationship

The internal force acted per unit area is called the *stress* and is given by:

$$\sigma = \frac{dF}{dA} \tag{7.12}$$

where σ is the stress, A is the cross-sectional area and F is the longitudinal force acting on the cross section.

Strain is defined as the change in length of a stressed structural element divided by the original length of the unstressed element. If the material behaves elastically, there is a linear relationship between strain and stress,

$$\varepsilon = \frac{\sigma}{E} \tag{7.13}$$

where ε is the strain and E is called the material modulus of elasticity (or Young's modulus).

B. Deformation in pure bending

Consideration of the beam subjected to pure bending, shown in Fig.7.5, indicates that the lower surface stretches and is therefore in tension and the upper surface shortens and thus is in compression. There is also a line or plane of zero stress, called the neutral axis or neutral plane. In Fig.7.5, the dot-dashed line represents the neutral axis. *R* is the radius of the bending beam, which is defined as the distance between the neutral axis and its centre. The longitudinal strain in the beam is [194]

$$\varepsilon = \frac{(R+y)\cdot d\theta - R\cdot d\theta}{R\cdot d\theta} = \frac{y}{R} \tag{7.14}$$

where *y* is the distance between a segmental plane and the neutral plane. When *y* is zero, the strain ε will be zero because it refers to the neutral plane; when *y* is positive, ε is positive, which represents tension (tensile strain) ; when *y* is negative, ε is negative, which represents compression (compressive strain).

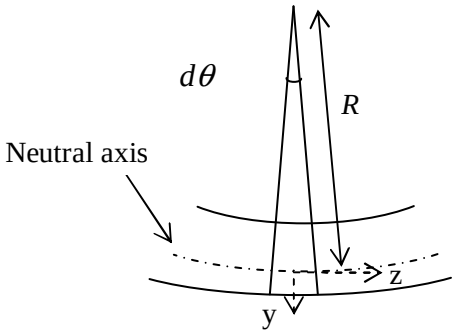

Fig.7.5 A beam subjected to pure bending.

C. Internal resisting moment

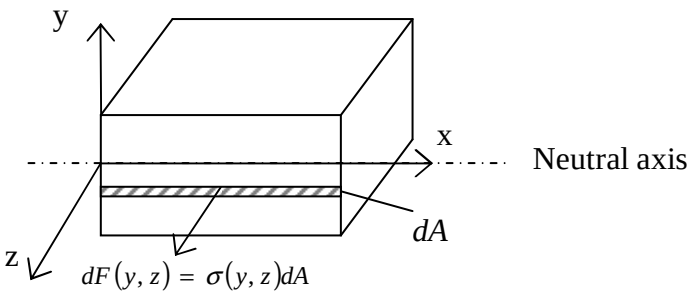

Fig.7.6 Internal resisting moment.

As shown in Fig.7.6, the total internal moment is [194]

$$M = \int_A y dF(y,z) = \int_A y\sigma(y,z) dA \tag{7.15}$$

Using Eq. (7.13) and (7.14), we can obtain

$$M = \frac{E}{R(z)} \int_A y^2 dA = \frac{EI}{R(z)} \tag{7.16}$$

where $I = \int_A y^2 dA$ is the second moment of area of the cross-section about the neutral axis.

D. The curvature-bending-moment relationship

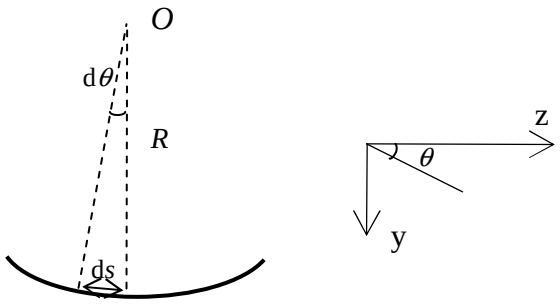

Fig.7.7 A deflected curve.

As shown in Fig.7.7, the instantaneous radius *R(z)* of a curvature is defined as

$$R(z) = -\frac{ds}{d\theta} \tag{7.17}$$

where *ds* is the differential length of a circular arc *s* and $d\theta$ is the differential circular angle. The differential length of a circular arc is

$$ds = \sqrt{1 + \left(\frac{dy}{dz}\right)^2}\, dz \approx dz \tag{7.18}$$

The approximation holds when $dy << dz$, which means that the shift in y direction is far shorter than the beam length L_z. Furthermore, as the shift in y direction is short, the differential angle is

$$d\theta \approx \tan\theta = \frac{dy}{dz} \tag{7.19}$$

Eq. (7.17) can the be rewritten as [194],

$$\frac{1}{R(z)} = -\frac{d^2 y}{dz^2} \tag{7.20}$$

or

$$\frac{d^2 y}{dz^2} = -\frac{M}{EI} \tag{7.21}$$

This is the differential equation of the deflection curve. If the variation of M with z is known, then this equation can be integrated twice to give the deflection z.

7.3.2 Stress distribution on an S-bending beam

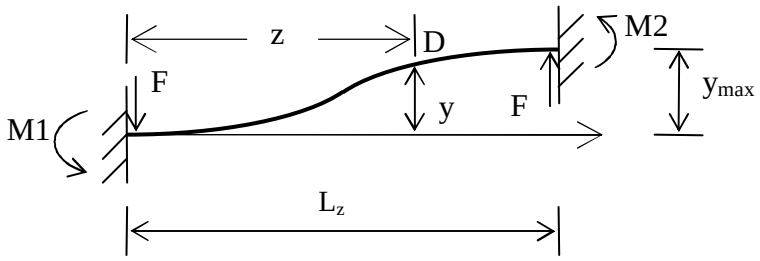

Fig.7.8 The diagram of S-bending.

Shown in Fig.7.8 is the diagram of S-bending, in which two fixed ends could be displaced vertically. The bending moment at point D is given by:

$$M = -F \cdot (L_z - z) + F \cdot z = -F \cdot (L_z - 2z) \tag{7.22}$$

where L_z is the beam length along the z-direction. Using momentum equilibrium and Eq. (7.21), the following second-order differential equation is obtained,

$$\frac{d^2 y}{dz^2} = \frac{2F}{EI} \cdot \left(\frac{L_z}{2} - z \right) \tag{7.23}$$

The slope of the beam curvature at the supported end must be zero and this point is taken as reference for the vertical displacement. Mathematically, they are $\frac{dy}{dz} = 0$ and $y = 0$ at $z = 0$. Applying this boundary condition to Eq.(7.23) yields:

$$y(z) = \frac{2F}{EI} \cdot \left(\frac{L_z}{4} z^2 - \frac{1}{6} z^3 \right) \tag{7.24}$$

The vertical displacement between two ends of the beam, y_{max}, can be obtained by applying $z=L_z$ in the above equation, which gives,

$$y_{\max} = \frac{2F}{EI} \cdot \frac{L_z^3}{12} \tag{7.25}$$

Subsequently, the curvature equation of the deflected structure is expressed as follows,

$$y(z) = \frac{y_{\max}}{L_z^3} \cdot (3L_z z^2 - 2z^3) \tag{7.26}$$

Using Eq. (7.14) and (7.20), the stress along the beam is obtained as:

$$\varepsilon(z) = h \cdot \frac{12 y_{\max}}{L_z^3} \cdot \left(\frac{L_z}{2} - z \right) \tag{7.27}$$

where *h* is the distance between a segmental plane and the neutral plane. It clearly shows that the stress is linear along the beam and, at the centre of the beam, the stress is zero.

7.3.3 Description of dispersion tuning devices

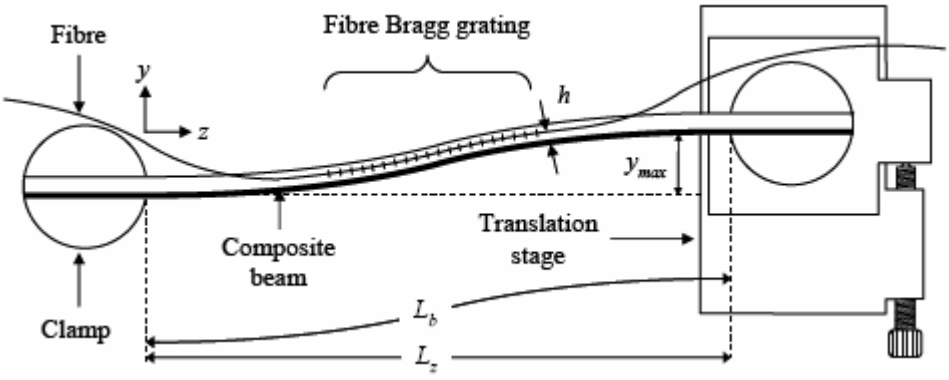

Fig.7.9 Schematic diagram of the S-bending dispersion-tuning device.

Fig.7.9 shows the schematic diagram for the dispersion-tuning FBG based on S-bending [153]. The S-bending structure is composed of a composite beam, a pair of clamps and a translation stage. The composite beam is made of two types of materials with a massive difference in their Young's modulus (~50:1), and the two materials are bonded together using a strong adhesive solution. Thus, the material with a larger Young's modulus essentially defines the neutral axis, while that with a lower Young's modulus embeds the fibre Bragg grating and roughly specifies *h*. The two materials we use here are, respectively, a hardened steel and plastic. The plastic should be flexible but it needs to show sufficient hardness to resist indentation caused by a moderate load. The beam is firmly supported by a pair of clamps in a perfectly straight position and at equal levels. Both of the clamps must be frictionless to ensure that no axial forces will act on the beam. One clamp is mounted on a linear translation stage that is oriented in a perpendicular direction. The stage is driven mechanically by a high resolution screw and can be moved in either a forward or backward direction.

By embedding a fibre Bragg grating into the beam for S-bending, with a distance of *h* from the neutral axis of the beam, the linear stress can be used to control the chirp and therefore the dispersion of the FBG. A linearly chirped FBG, whose maximum and

minimum Bragg wavelengths are respectively λ_L and λ_S , with a length of *L*, is embedded into the beam. At the idle state, the Bragg wavelength distribution along the FBG is,

$$\lambda_{B,idle} = \lambda_S + (\lambda_L - \lambda_S)\cdot\frac{z}{L} \qquad 0 < z < L \tag{7.28}$$

Its central wavelength and bandwidth are $\frac{\lambda_L + \lambda_S}{2}$ and $\lambda_L - \lambda_S$, respectively.

As the beam is bent in an S-shape, according to the stress distribution described by Eq. (7.27), the Bragg wavelength distribution along the FBG will be,

$$\lambda_B(z) = \left[\lambda_S + (\lambda_L - \lambda_S)\frac{z}{L}\right]\cdot\left[1+\alpha\frac{(2z-L)}{L}\right]$$

$$= (1-\alpha)\lambda_S + (\lambda_L - \lambda_S - \alpha\lambda_L + 3\alpha\lambda_S)\frac{z}{L} + 2\alpha(\lambda_L - \lambda_S)\left(\frac{z}{L}\right)^2 \quad 0 < z < L \tag{7.29}$$

where,

$$\alpha = (1-\rho_e)\frac{6\cdot h\cdot L\cdot y_{\max}}{L_z^3} \tag{7.30}$$

ρ_e is the photo-elastic constant, and L_z is the beam length.

If $\alpha << 1$ and $\lambda_L - \lambda_S << \lambda_S$, the item concerning z^2 can be neglected. Hence,

$$\lambda_B(z) = (1-\alpha)\lambda_S + (\lambda_L - \lambda_S - \alpha\lambda_L + 3\alpha\lambda_S)\frac{z}{L} \tag{7.31}$$

Therefore, the FBG is still a linearly chirped FBG after the S-bending, and the minimum and maximum Bragg wavelengths of the FBG are respectively,

$$\lambda_{B,\min} = \lambda_B(0) = \lambda_S - \alpha\lambda_S \tag{7.32}$$

$$\lambda_{B,\max} = \lambda_B(L) = \lambda_L + \alpha\lambda_S \tag{7.33}$$

Consequently, its central wavelength, bandwidth and dispersion are respectively,

$$\lambda_{Center} = \frac{\lambda_{B,\max} + \lambda_{B,\min}}{2} = \frac{\lambda_L + \lambda_S}{2} \tag{7.34}$$

$$BW = \lambda_{B,\max} - \lambda_{B,\min} = \lambda_L - \lambda_S + 2\alpha\lambda_S \tag{7.35}$$

$$D = \frac{2n_{eff}L}{c\cdot BW} \tag{7.36}$$

In conclusion, by changing $y_{\max}$ in the S-bending structure, the FBG is still a linearly chirped grating (as shown in Eq. (7.31)), with a constant central wavelength (as shown in Eq. (7.34)), while the bandwidth and dispersion could be altered (as shown in Eq. (7.35) and (7.36)).

7.4 Tunable dispersion compensators with a wide tuning range

7.4.1 Device principle

Tunable dispersion compensators with a fixed central wavelength are highly desirable for optical communication systems. For temperature tuning, by applying a linear temperature gradient along a linearly chirped FBG with a fixed temperature value in the centre of the grating, the reflection bandwidth varies linearly with the temperature difference between both ends, while keeping the central wavelength fixed [158]. To achieve dispersion-tuning using strain, while keep a fixed central wavelength, the S-bending tuning structure [159] is a good choice compared with other complicated techniques [181-185].

As described in Section 7.3, using the S-bending technique, the dispersion of a linearly chirped FBG can be tuned while its central wavelength is fixed. At the idle state, the dispersion sign is dependent on the light input directions. Although it is possible to invert the dispersion sign or approach zero dispersion by the S-bending tuning, it is not practical because this requires a huge variation in the Bragg wavelength of the FBG [159].

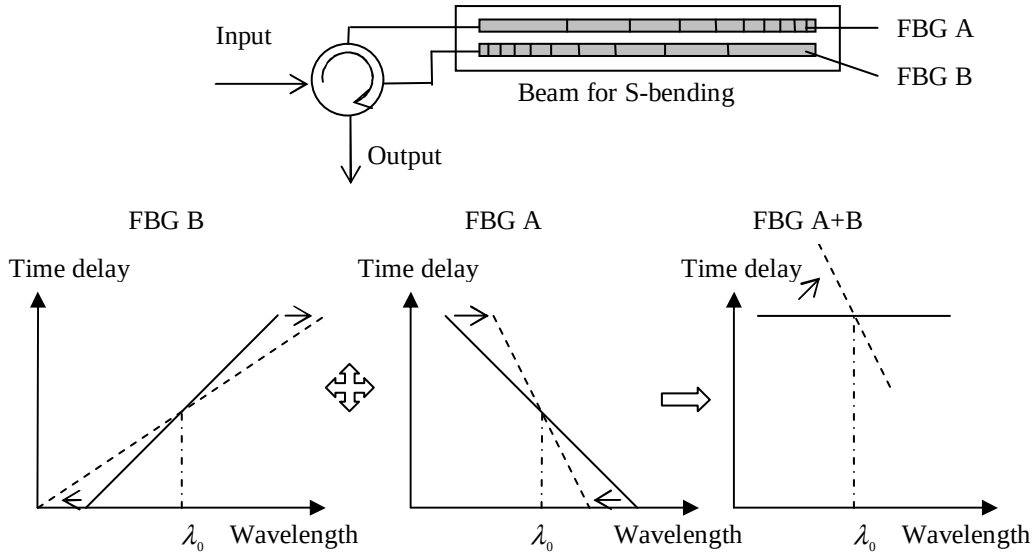

Fig.7.10 Schematic diagram of a tunable dispersion compensator.

To obtain a dispersion compensator with a tuning range covering positive, negative and zero dispersion altogether, we propose a new configuration based on the S-bending technique. As shown in Fig.7.10, it consists of cascading two identical linearly chirped FBGs using a four-port circulator. At the idle state, it produces zero dispersion because

the dispersion sign of a chirped FBG changes with respect to the input direction. Both gratings are embedded parallel in one beam, with opposite chirp directions in relation to the stress gradient for a simultaneous S-bending tuning, and thus a stress gradient induces opposite bandwidth variations for each grating (as shown in Fig.7.10). The sign of the combined dispersion is dependent on the displacement direction (i.e., the sign of y_{max}) of the S-bending.

A similar design has already been demonstrated using a thermal tuning technique [195]. The advantages of using strain tuning include that it consumes no power and it has the potential to achieve a larger bandwidth tuning range.

7.4.2 Simulation of device performance

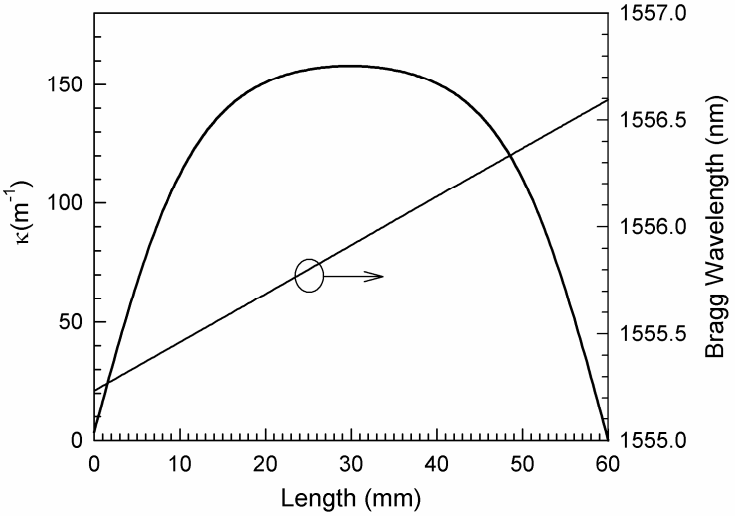

Fig.7.11 Parameters of the linearly chirped FBG for simulation.

In this section, a tunable dispersion compensator with a wide tuning range is simulated based on the structure shown in Fig.7.10. Parameters of the FBG for simulation are shown in Fig.7.11. To alleviate the ripple in its reflection time delay spectrum, the 60-mm-long linearly chirped FBG is apodized by a hyperbolic tangent function [1]. Two identical FBGs are embedded with opposite chirp directions in one uniform beam for S-bending tuning, as the configuration shown in Fig.7.10.

The overall reflection and time delay spectrum of the dual-FBGs configuration are calculated and are shown in Fig.7.12. At the idle state, zero dispersion is obtained with a 3dB bandwidth of ~0.8nm. As the dispersion is +400 ps/nm or -400 ps/nm, the 3dB bandwidth is ~0.6nm. Over the whole tuning range (from +400 ps/nm to -400 ps/nm), its

3dB bandwidth is more than 0.6nm, which is needed for its application in a 40Gbit/s system.

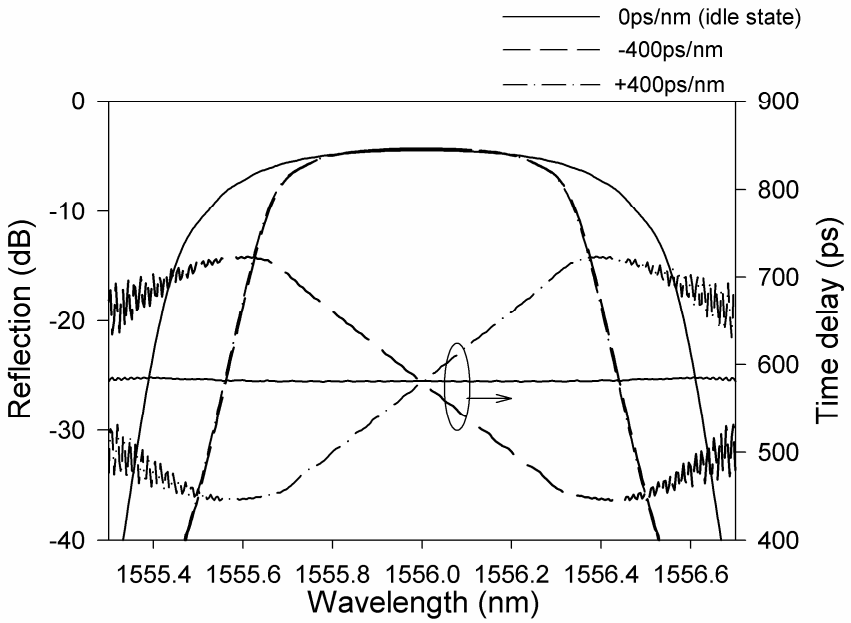

Fig.7.12 Simulated reflection and time delay spectra of the dual-FBGs configuration.

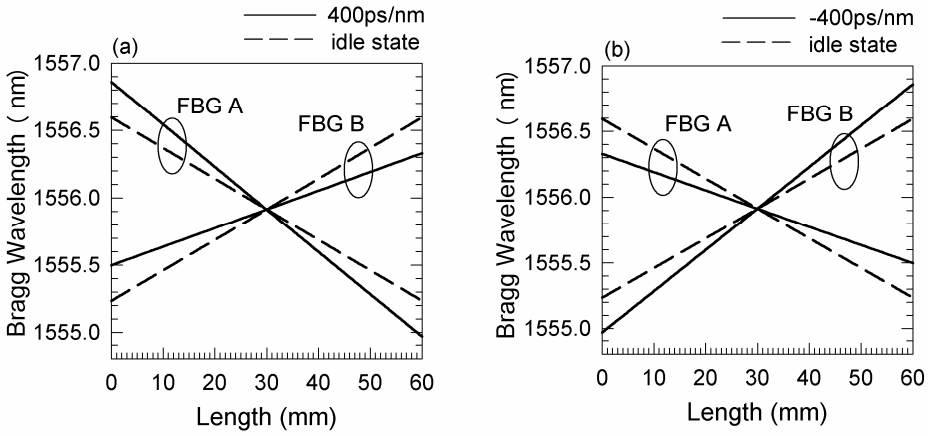

Fig.7.13 Bragg wavelength distribution along the FBGs under tuning.

Bragg wavelength distributions along the two FBGs under tuning (solid lines) are calculated (as shown in Fig.7.13) and compared with those at the idle state (dashed lines). As the S-bending is applied, each grating experiences a linear stress gradient and therefore a bandwidth variation, while the Bragg wavelength at the centre is fixed. In addition, both FBGs have identical Bragg wavelength variations along the beam because the same stress field is applied along the two gratings.

Shown in Fig.7.14 are the variations of dispersion and 3-dB bandwidth of the device with a dual-FBG configuration during tuning. The amount of tuning is denoted by the

Bragg wavelength shift at one end of the FBG. Over the whole tuning range, the 3dB bandwidth is more than 0.6nm. The dispersion of the device with a dual-FBG configuration is tuned from -400 to +400ps/nm, and the corresponding 3-dB bandwidth varies between 0.6nm and 0.8nm.

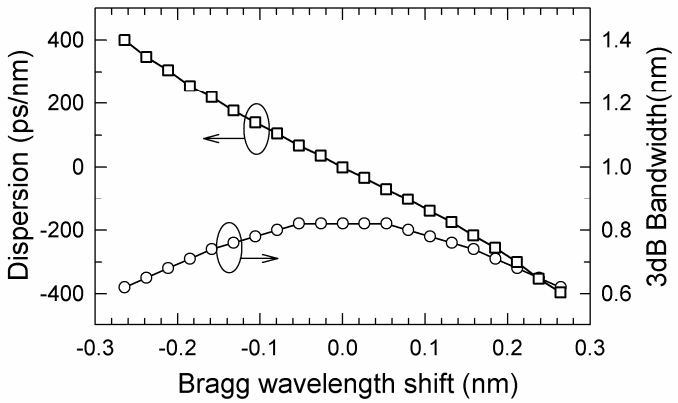

Fig.7.14 Variations of the dispersion and 3-dB bandwidth of the device with a dual-FBG configuration.

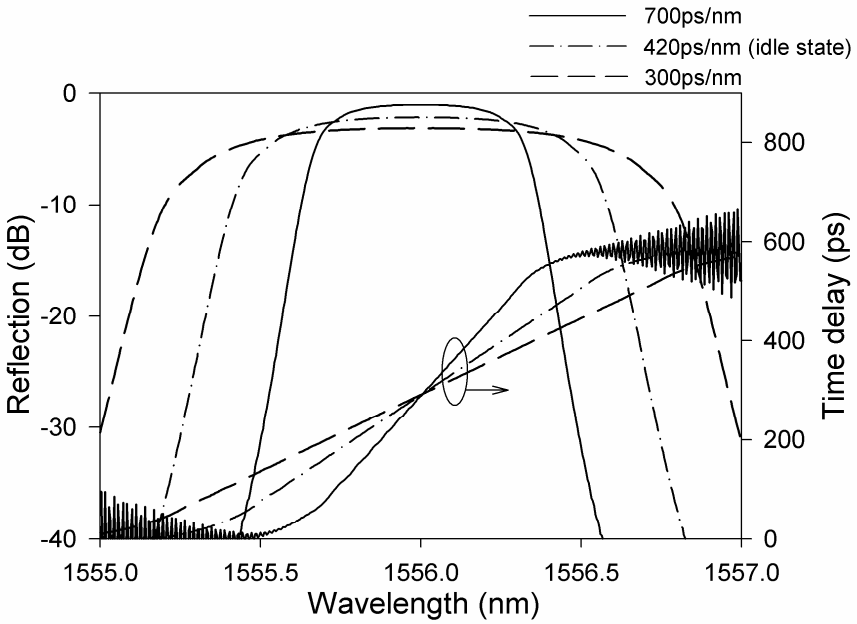

Fig.7.15 Simulated reflection and time delay spectra of the single-FBG configuration.

For comparison, the reflection and time delay spectra of the single-FBG configuration are calculated and are shown in Fig.7.15. At the idle state, the dispersion value is 420ps/nm with a 3dB bandwidth of ~1.2nm. The dispersion is tuned from 300ps/nm to 700ps/nm. For this single-FBG configuration, although it is possible to achieve an even lower value of dispersion, a very large bandwidth variation is required. Moreover, the

insertion loss of the tunable dispersion compensator will increase with the decrease of dispersion, which is undesirable for practical applications.

Shown in Fig.7.16 are the variations of the dispersion and 3dB bandwidth of the device with a single-FBG configuration during tuning. Over the whole tuning range, the 3dB bandwidth is more than 0.6nm. The dispersion tuning range is from 700ps/nm to 300ps/nm, while the corresponding 3-dB bandwidth varies from 0.6nm to 1.3nm. Comparing Fig.7.14 and Fig.7.16, we can find that the dispersion tuning range of the dual-FBG configuration is twice as wide as that of the single-FBG configuration. Another advantage for a dual-FBG configuration is that its tuning range covers positive, negative and zero dispersion.

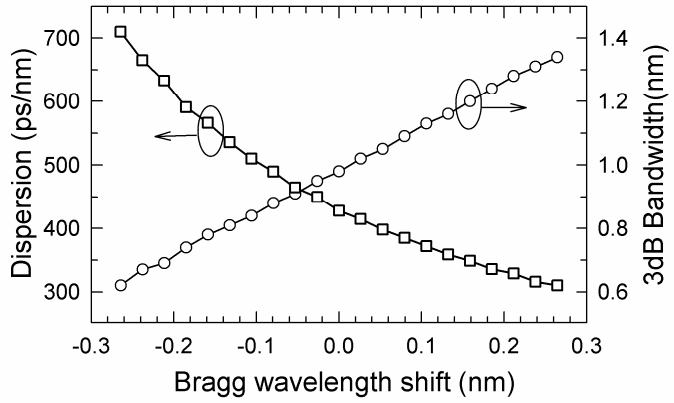

Fig.7.16 Variations of dispersion and 3-dB bandwidth of the device with a single-FBG configuration.

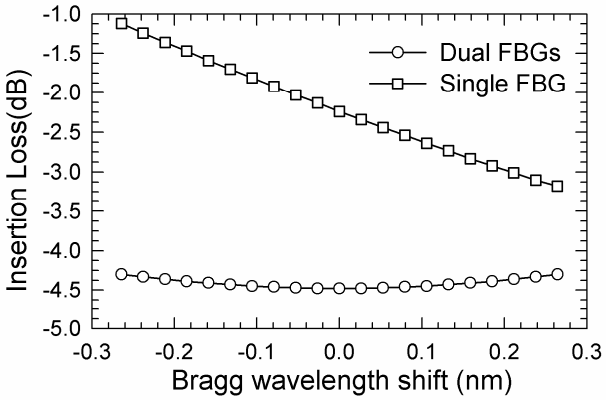

Fig.7.17 Variations of insertion loss for the single-FBG (□) and dual-FBG (○) configuration.

Shown in Fig.7.17 are the variations of insertion loss of the two configurations of dispersion compensators. Over the whole tuning range, for the single-FBG configuration, the insertion loss varies linearly with respect to the maximum Bragg wavelength shift, while for the dual-FBG configuration, it is almost constant.

In summary, based on the S-bending tuning technique, we propose a new configuration of a dispersion compensator. Its advantages include a wider tuning range around zero dispersion and a reduced insertion loss variation in the whole tuning range.

7.5 Tunable pure dispersion slope compensators

7.5.1 Device principle

Transmission fibres have a small but nonzero dispersion slope (DS) (as shown in Table 7.1). In the next-generation ultra-high-speed optical transmission systems, for example at a data bit rate of 160 Gbit/s, the dispersion slope will pose limitations to transmission, and therefore must be accurately compensated [196]. Although most of the dispersion slope can be compensated by using dispersion compensating fibres with a carefully designed dispersion slope, dynamic compensation is still necessary to compensate the residual dispersion slope because the tolerance is so tight.

Tunable dispersion slope compensators could be achieved by using a third-order nonlinearly-chirped FBG plus a variable uniform strain or temperature field [186-187], but for devices with this configuration, tuning the dispersion slope is always accompanied by an apparent central wavelength shift, and therefore it is difficult for them to dynamically compensate dispersion-slope in a broadband transmission system.

Tunable dispersion slope compensators could also be achieved by using a linearly chirped FBG plus a variable quadratic nonlinear strain or temperature field [188-193]. For devices with this configuration, because the dispersion (second-order) will also be changed as the dispersion slope is altered, an additional separate control of dispersion is required to obtain a pure dispersion slope compensation. In [190-193], the dispersion slope is tuned by controlling a quadratic temperature distribution along a linearly chirped FBG. An additional linear temperature distribution is also applied and controlled to keep the dispersion constant as the dispersion slope is changed. Moreover, to obtain pure dispersion slope compensation, a fixed and linearly chirped FBG or a DCF is cascaded compensating the residual constant dispersion in the tuned FBG. In [189], the quadratic strain field applied to a linearly chirped FBG is produced and controlled by bending a linearly tapered beam in an S-shape. Because the dispersion is also changed as dispersion slope is tuned, another FBG with a tunable dispersion is cascaded to obtain pure dispersion slope compensation.

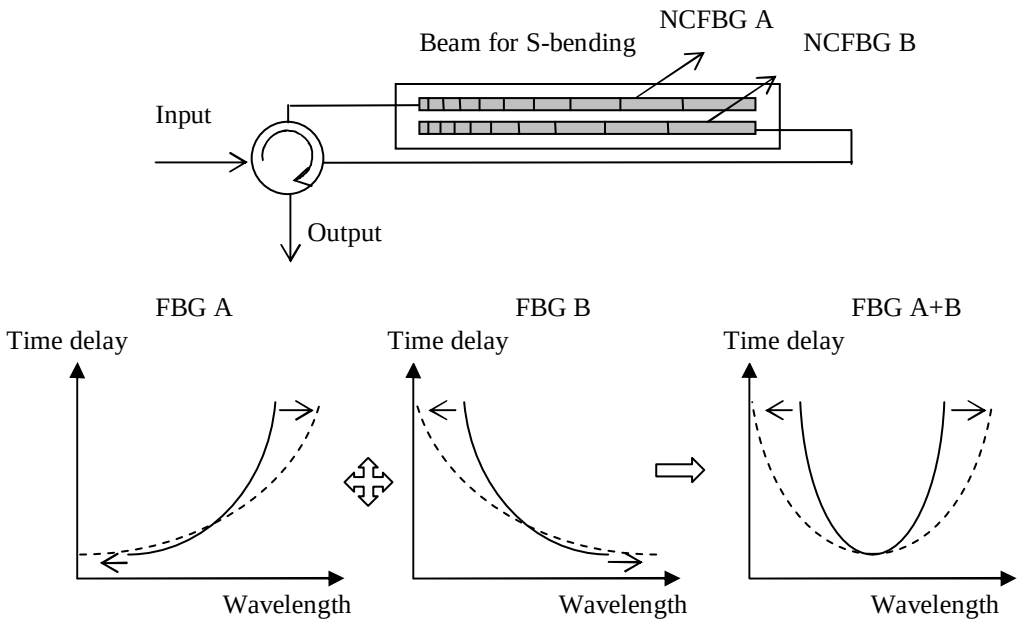

Fig.7.18 Schematic diagram of a tunable dispersion slope compensator.

In this section, we will propose and demonstrate a new tunable pure dispersion slope compensator. It consists of two cascaded nonlinearly-chirped FBGs of different types. As shown in Fig.7.18, the two FBGs are embedded parallel, with identical chirp directions, in a uniform beam for S-bending. The light is first reflected from the short Bragg wavelength end of FBG A, and then reflected from the long Bragg wavelength end of FBG B. Finally, as the effects of FBG A and B are combined, a pure DS is produced, since the second-order dispersion for the two FBGs is completely cancelled. As FBG A and B are tuned together, both DS and dispersion (second-order) are altered on each single grating, but for the combined effects of the two FBGs, only the DS is varied, since the second-order dispersion from the two FBGs will always be completely cancelled. Therefore, one tuning structure is enough for a tunable pure DS compensation. Another advantage is that, as the dispersion slope is tuned, the central wavelength is invariant, which is due to the use of the S-bending technique.

Pure dispersion slope compensators, operating based on this principle, have been reported before [197-198], but their tuning capacity has not been demonstrated.

At the idle state, the Bragg wavelength distributions of the nonlinearly chirped FBG A and B are respectively,

$$\lambda_{A,idle}(z) = \lambda_S + (\lambda_L - \lambda_S)\sqrt{\frac{z}{L}} \tag{7.37}$$

$$\lambda_{B,idle}(z) = \lambda_L - (\lambda_L - \lambda_S)\sqrt{\frac{z}{L}} \tag{7.38}$$

where, λ_L and λ_S are, respectively, the maximum and minimum Bragg wavelengths along the FBGs, and L is the grating length. As shown in Fig.7.18, in the cascading configuration, the light is reflected from the short Bragg wavelength end of FBG A and the long Bragg wavelength end of FBG B. At the idle state, the dispersion (D) and dispersion slope (DS) of FBG A and B are respectively,

$$D_{A,idle} = \frac{4n_{eff}L}{c} \cdot \frac{\lambda - \lambda_S}{\lambda_L - \lambda_S} \tag{7.39}$$

$$D_{B,idle} = \frac{4n_{eff}L}{c} \cdot \frac{\lambda - \lambda_L}{\lambda_L - \lambda_S} \tag{7.40}$$

$$DS_{A,idle} = \frac{4n_{eff}L}{c} \cdot \frac{1}{(\lambda_L - \lambda_S)^2} \tag{7.41}$$

$$DS_{B,idle} = \frac{4n_{eff}L}{c} \cdot \frac{1}{(\lambda_L - \lambda_S)^2} \tag{7.42}$$

and the dispersion (D) and dispersion slope (DS) of the dual-FBG configuration are respectively,

$$D_{idle} = \frac{4n_{eff}L}{c} \cdot \frac{2\lambda - (\lambda_L + \lambda_S)}{\lambda_L - \lambda_S} \tag{7.43}$$

$$DS_{idle} = \frac{8n_{eff}L}{c} \cdot \frac{1}{(\lambda_L - \lambda_S)^2} \tag{7.44}$$

Eq. (7.38) and (7.39) show that at the central wavelength $\frac{\lambda_L + \lambda_S}{2}$, FBG A and B have dispersion with an identical absolute value, but an opposite sign. Therefore, the overall dispersion of the dual-FBG configuration cancels completely at the central wavelength (Eq.(7.42)). Eq. (7.40) and (7.41) show that the dispersion slope of FBG A and B is identical and their overall effect is a larger dispersion slope (Eq.(7.43)).

The FBG A and B are then embedded parallel *with identical chirp directions* in one uniform beam. According to Eq. (7.27), as the FBGs are bent in an S-shape, Bragg wavelength distributions along FBG A and B are respectively,

$$\lambda_A(z) = \left[\lambda_S + (\lambda_L - \lambda_S)\sqrt{\frac{z}{L}}\right] \cdot \left[1 + \alpha\frac{(2z - L)}{L}\right] \tag{7.45}$$

$$\lambda_B(z) = \left[\lambda_L - (\lambda_L - \lambda_S)\sqrt{\frac{z}{L}}\right] \cdot \left[1 - \alpha\frac{(2z-L)}{L}\right] \tag{7.46}$$

where, α is given by Eq. (7.30).

7.5.2 Simulation of device performance

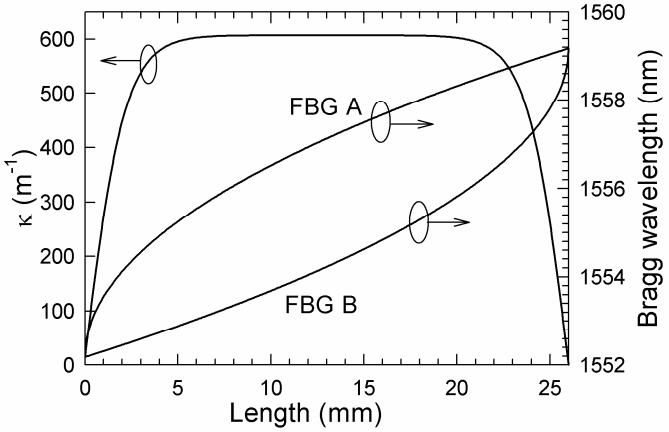

Fig.7.19 Parameters of FBG A and B for the tunable DS compensator.

In this section, a tunable pure DS compensator is simulated based on the schematic shown in Fig.7.18. It is designed for dynamically compensating the DS in a 160Gbit/s transmission system, so an operation bandwidth of more than 3 nm is required through the tuning process. Parameters of FBG A and B used for simulation are shown in Fig.7.19. To alleviate the ripple in its reflection and time delay spectra, both FBG A and B are apodized by a hyperbolic tangent function [1]. The FBG A and B are embedded parallel with identical chirp directions in a uniform beam for S-bending.

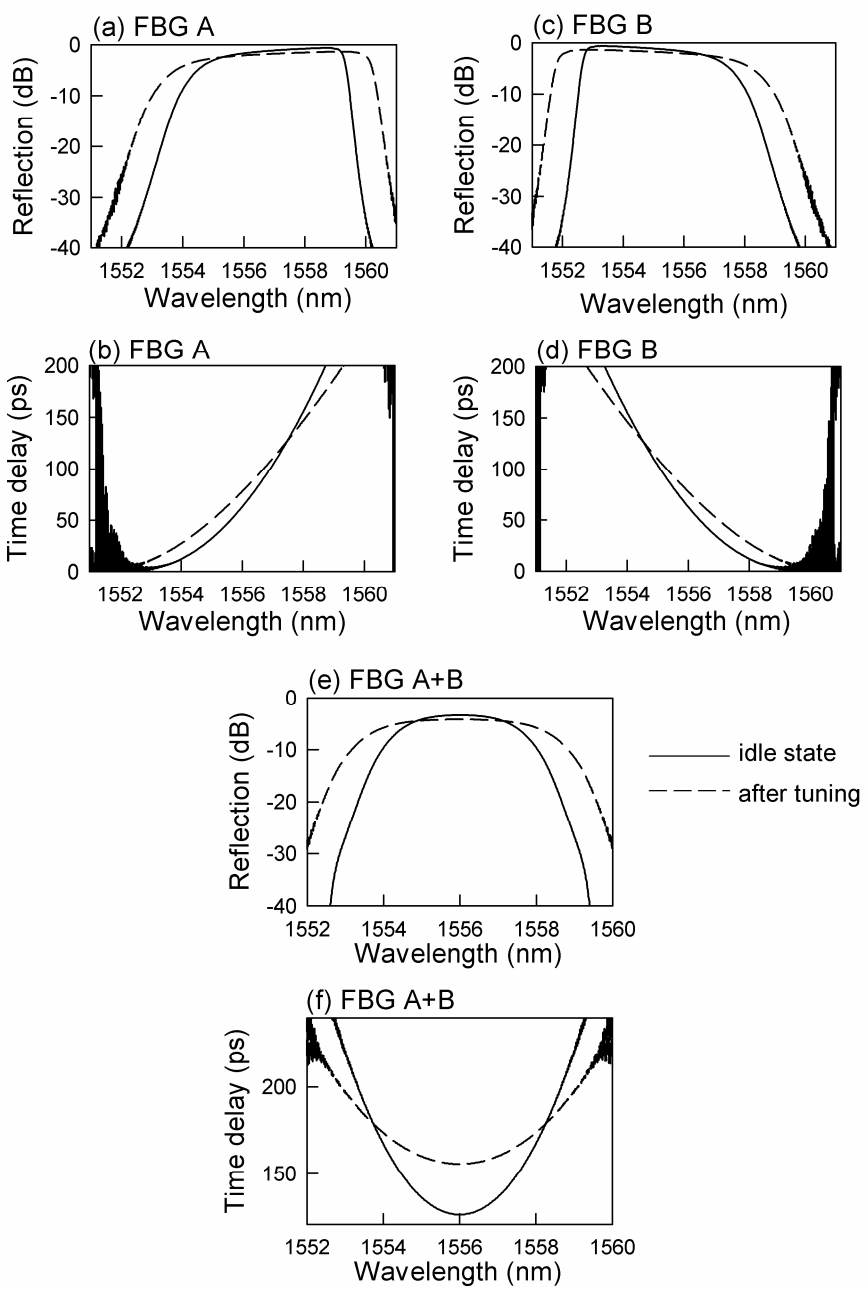

Fig.7.20 Simulated reflection and time delay spectra of FBG A, FBG B and the combination of FBG A and B. (The solid lines are for the idle state, and the dashed lines are for a tuning state).

The reflection and time delay spectra of FBG A, FBG B, and the combination of FBG A and B are calculated and are shown in Fig.7.20. The solid lines are for the idle state, and the dashed lines are results at a tuning state, in which the Bragg wavelength shift at the ends of both gratings are ~1nm (as shown in Fig. 7.20 (a), (c) and (e)). As shown in Fig. 7.20 (b), the light is reflected from the short Bragg wavelength end of FBG A, experiencing positive second-order dispersion and an additional DS. Similarly, as shown in Fig. 7.20 (d), the light is reflected from the long Bragg wavelength end of FBG B, while experiencing negative second-order dispersion and another additional DS. Finally,

as shown in Fig. 7.20 (f), when the effects of FBG A and B are combined, the second-order dispersion is completely cancelled at the central wavelength, and a pure DS is produced. As FBG A and B are tuned together, both the second-order dispersion and DS are altered on each single grating. But for the combined effects of two FBGs, only the DS is varied since the second-order dispersion from the two FBGs can always completely cancel each other. At the idle state, the DS is 11ps/nm^2 with a 3dB bandwidth of ~3.4nm. As the DS is tuned to 4.4ps/nm^2, the 3dB bandwidth is ~4.7nm.

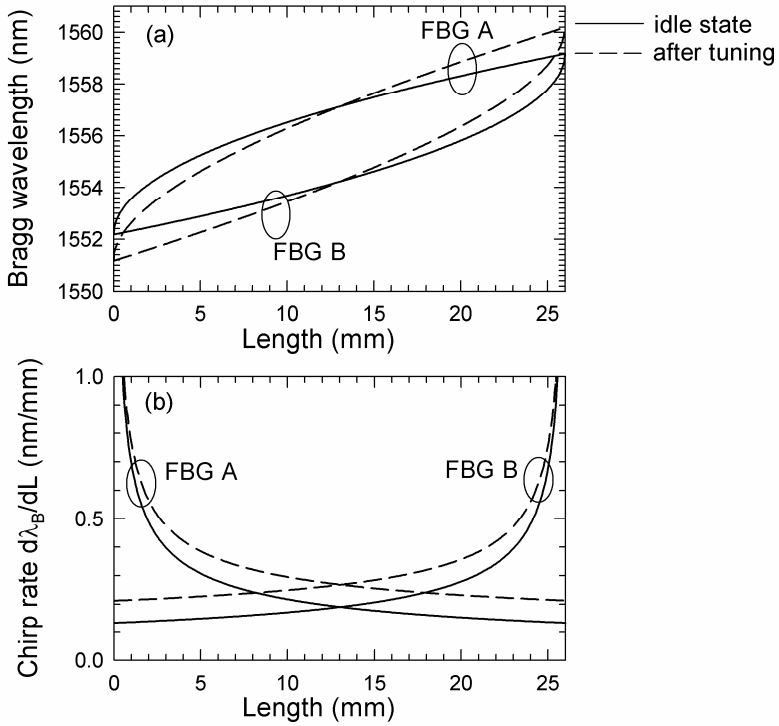

Fig.7.21 (a) Bragg wavelength and (b) chirp rate distributions along the FBGs.

Bragg wavelength and chirp rate distributions along the FBG A and B are shown in Fig.7.21 (a) and (b). The solid lines are for the idle state, and the dashed lines correspond to the same tuning state as in Fig.7.20. As the S-bending is applied, each FBG experiences a linear stress gradient, while the Bragg wavelength at the centre of the FBGs is fixed. In addition, both FBGs have identical Bragg wavelength variations (Fig.7.21 (a)) along the beam because the same stress gradient is applied. As shown in Fig.7.21 (b), at both the idle and tuning state, the chirp rate of FBG A is symmetrical to that of FBG B with respect to the centre of the FBGs.

Shown in Fig.7.22 (a) and (b) are the values of DS, 3-dB bandwidth and insertion loss of the tunable DS compensator. The amount of tuning is denoted by the maximum Bragg

wavelength shift of the FBG. Over the whole tuning range, the 3dB bandwidth is more than 3nm. The DS of the device is tuned from 11ps/nm^2 to 3ps/nm^2. The corresponding 3-dB bandwidth varies between 3.4nm and 5.6nm, and the insertion loss variation is less than 1.5 dB.

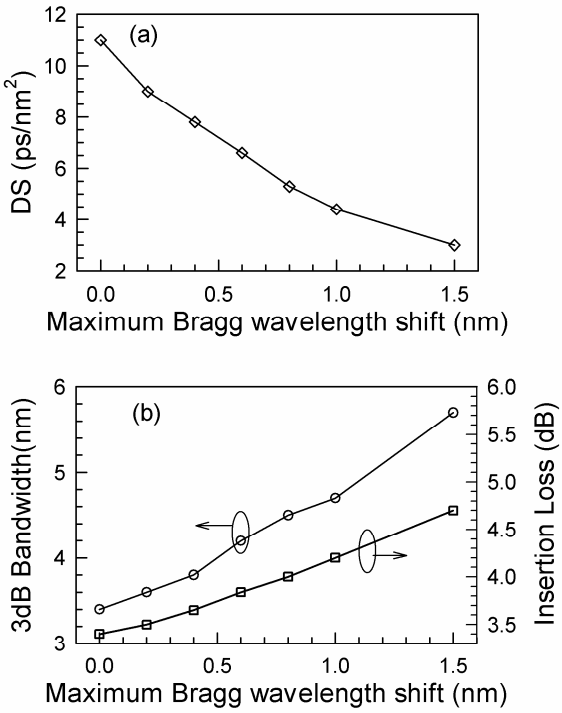

Fig.7.22 Calculated values of (a) DS, (b) 3-dB bandwidth and insertion loss of the tunable DS compensator.

7.5.3 Device fabrication and characterization

FBG A and B are fabricated using the continuous grating writing technique, and their apodization profile and chirp distribution are as shown in Fig.7.19. At the idle state, their reflection spectra are measured and are shown in Fig.7.23. For FBG A, the measurements are taken from the short Bragg wavelength end, and for FBG B, the measurements are taken from the long Bragg wavelength end. This is consistent with the cascading configuration of the tunable TOD compensator (as shown in Fig.7.18).

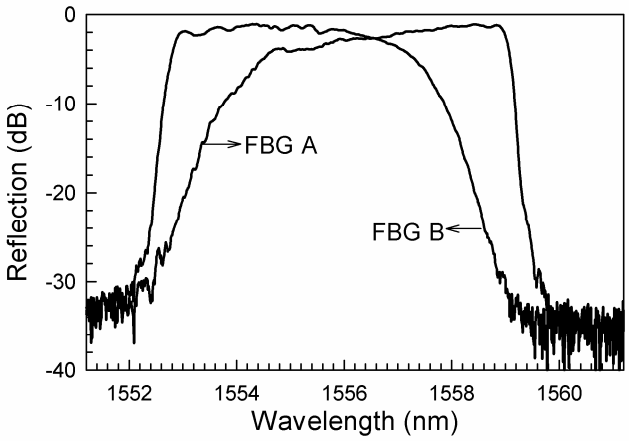

Fig.7.23 Measured reflection spectra of FBG A and B.

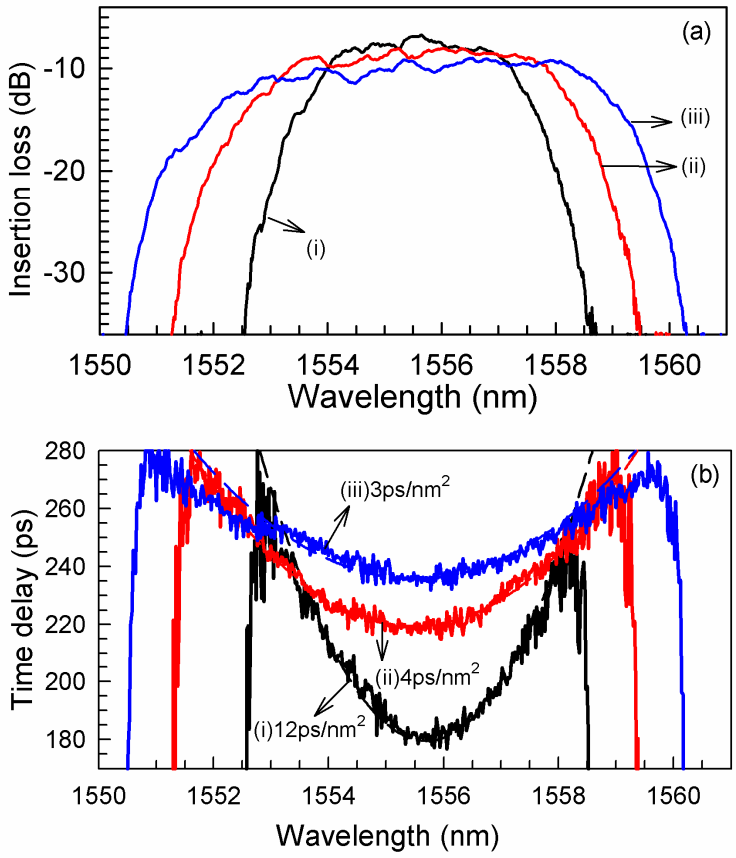

Fig.7.24 Measured reflection and time delay spectra of the tunable DS compensator as the DS is (i) 12ps/nm^2, (ii) 4ps/nm^2, or (iii) 3ps/nm^2.

The FBG A and B are then embedded parallel in a uniform beam for S-bending, as shown in Fig. 7.18. To obtain a tunable pure DS compensator with a fixed central wavelength, it is crucial to ensure that both FBGs are put in the centre of the beam. The reflection and time delay spectra of the tunable DS compensator are measured using the

modulation phase-shift method. The results are shown in Fig.7.24. At the idle state, the DS is measured to be ~12ps/nm^2. Then, it is tuned until a DS of 3ps/nm^2 is achieved. Over the whole tuning range, the central wavelength variation is less than 0.1nm. The peak-to-peak value of the group delay ripple in the operating bandwidth is ~12ps.

Shown in Fig.7.25 are the measured DS and 3-dB bandwidth of the tunable DS compensator. As $y_{max}>0$, the 3 dB bandwidth is more than 3nm. The amount of tuning is denoted by the displacement (y_{max}) perpendicular to the beam for S-bending. The beam length used in the experiment is 90mm.

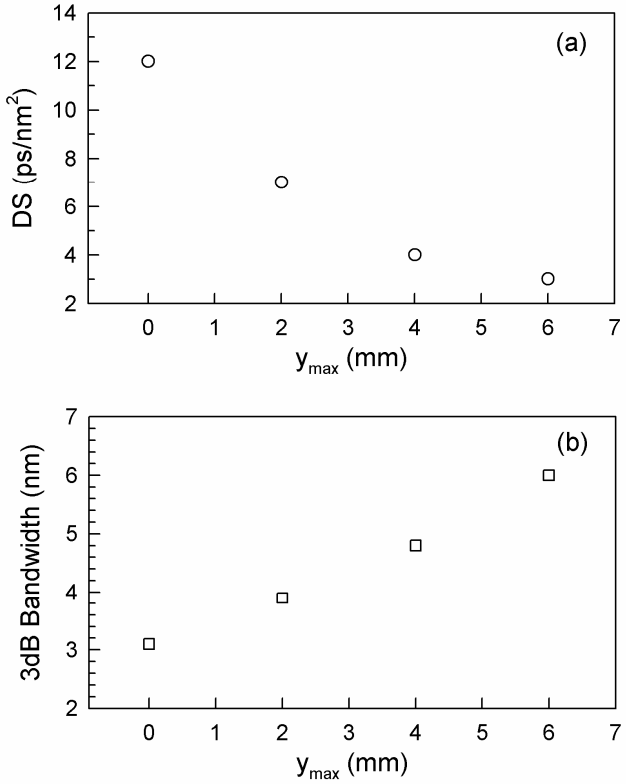

Fig.7.25 Measured values of (a) DS, (b) 3-dB bandwidth of the tunable DS compensator.

To apply this device in a practical high bit-rate transmission system, the polarization related effects need to be further investigated. In Ref [153], the additional polarization mode dispersion (PMD) and polarization dependent loss (PDL) induced by the tuning has been demonstrated to be very small in a wavelength-tuning FBG filter based on the same beam and a similar bending technique.

In summary, based on the S-bending technique and a dual-FBG configuration, a tunable dispersion slope compensator is proposed and demonstrated. Its main advantage is that a tunable pure dispersion slope is achieved with a very simple tuning structure.

7.6 Controlling the output pulse width in a fibre laser using a tunable FBG

7.6.1 Device description and characterization

In this section, a linearly chirped FBG is used in a laser cavity. By tuning the dispersion of the FBG using the S-bending technique, the output pulse width of the fibre laser is controlled.

A linearly chirped FBG, with a length of 20mm, is embedded in a uniform beam for the S-bending tuning. At the idle state, the FBG has a bandwidth of ~6 nm, centred at 1064nm, and the dispersion is ~33ps/nm. To achieve a large dispersion tuning range, the beam length for S-bending is ~65mm. As shown before, when the beam is bent in an S-shape, the FBG still has a linear chirp, but its bandwidth and dispersion will be altered.

Shown in Fig.7.26 is the evolution of the transmission spectrum of the FBG as it is tuned by using the S-bending technique. For a linearly chirped FBG with a particular length and effective index modulation, the absolute value of its dispersion is proportional to its transmission loss in decibels [207]. Therefore, at each state, the value of dispersion could be estimated from the corresponding transmission spectrum. As shown in Fig.7.26, dispersion of the linearly chirped FBG is tuned from ~20ps/nm to ~55ps/nm.

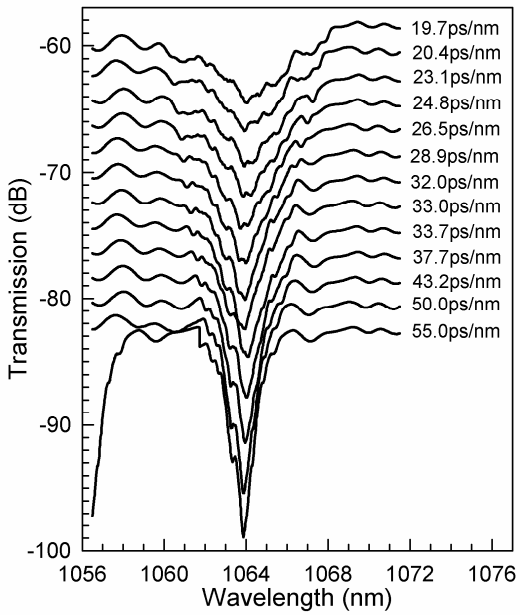

Fig.7.26 Evolution of transmission spectrum of the FBG under tuning.

7.6.2 Controlling the output pulse width of fibre lasers

The configuration of fibre laser is shown in Fig.7.27. Its principle is similar to the laser in Ref [200-202]. A ytterbium-doped fibre is spliced into a standard fibre connecting the chirped FBG with a tunable dispersion. A 980 nm semiconductor laser diode is used as the pump source and a semiconductor saturable-absorber mirror (SESAM) is used to obtain pulsed operation [199]. The fibre laser operates in the soliton-supporting dispersion regime, and is mode-locked by a saturable absorber, resembling a true soliton laser. The length of the laser cavity is ~ 2 metres and therefore the repetition rate of the output pulses is measured to be ~52MHz. The dispersion of the cavity is completely regulated and can be controlled by the dispersion of the chirped FBG because the length of fibre in the cavity is very short.

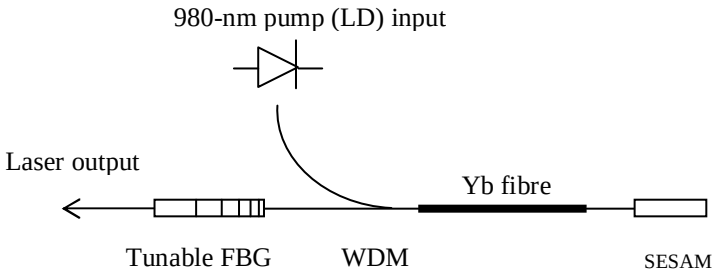

Fig.7.27. Configuration of the fibre laser.

The output pulses are measured using an auto-correlator based on the second harmonic generation (SHG) technique. As the dispersion of the chirped FBG is tuned, the autocorrelation traces of laser output are measured and are shown in Fig.7.28, and the corresponding spectra are also measured and are shown in Fig.7.29. We can see that the central wavelength of the laser shifts only very slightly during tuning. The two obvious shifts in the central wavelength (at 21ps/nm and 14ps/nm) are due to the fact that we changed the beam length during the experiments.

Shown in Fig.7.30 is a fit of the measured autocorrelation curve to the theoretical autocorrelation trace of a hyperbolic secant pulse. It confirms that the generated pulse from the laser is indeed a soliton.

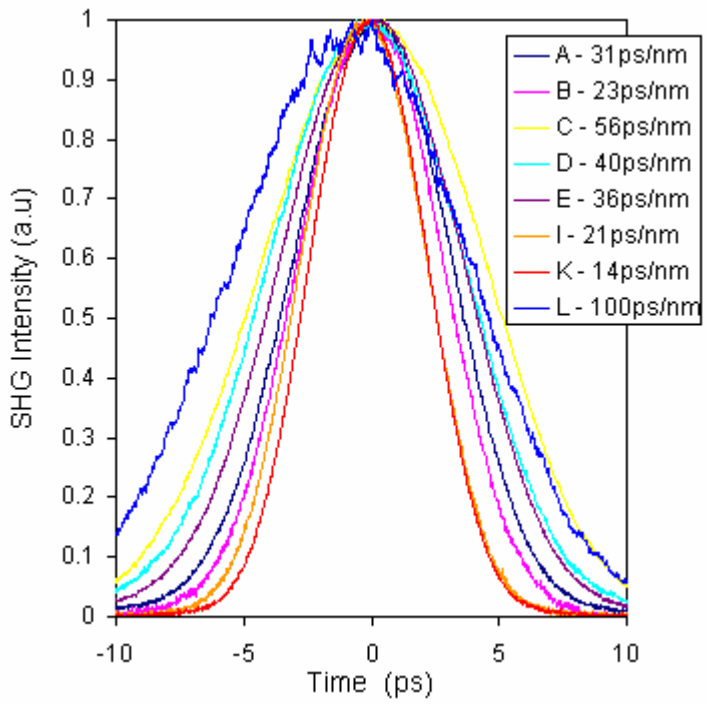

Fig.7.28. Measured SHG autocorrelation trace as the dispersion of the FBG varies.

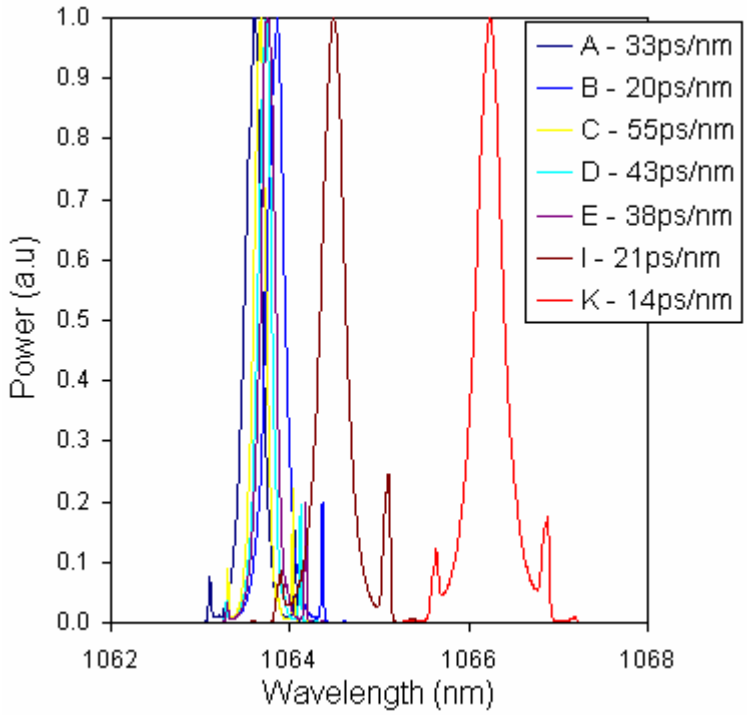

Fig.7.29. Measured spectrum of the laser output as the dispersion of the FBG varies.

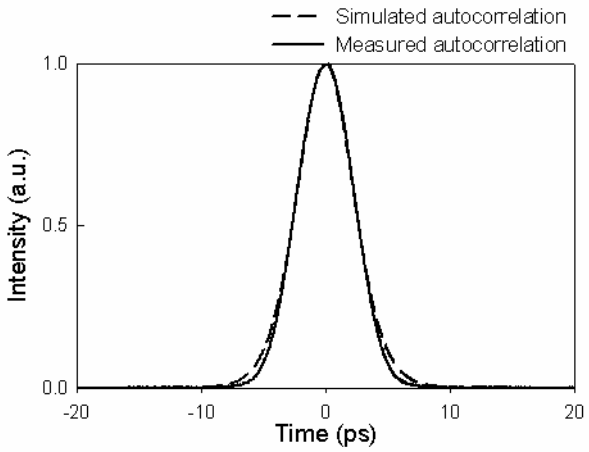

Fig.7.30 Measured (solid line) autocorrelation trace as the FBG dispersion is 14ps/nm. A sech fit (dashed line) to the trace gives a FWHM pulse width of 4.5ps.

From the autocorrelation traces, the output pulse widths of the laser are calculated and summarized in Fig.7.31. It is apparent that the output pulse width of the laser is controlled by tuning the dispersion of the FBG. It is worth noting that, in theory, the pulse width scales with $\sqrt{|D|}$ for this soliton laser [203-204].

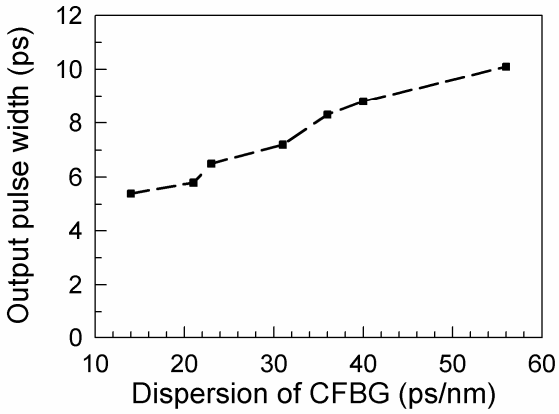

Fig.7.31 Output pulse width of the laser as the dispersion of the FBG varies.

7.7 Conclusions

In this Chapter, we first review the dynamic dispersion and dispersion slope compensation techniques based on a combination of different tuning mechanisms and different FBGs. The topic of this chapter is the S-bending tuning technique, which can effectively provide a variable linear strain field along an FBG. It special advantage is that the central wavelength of the FBG is invariant when the linear strain gradient along the FBG is altered.

The S-bending tuning technique is then used to develop two new devices: a tunable dispersion compensator with a wide tuning range and a pure dispersion slope compensator. Both of them are based on tuning a pair of FBGs embedded in a single uniform beam. The advantage of using a dual-FBG configuration in a tunable dispersion compensator is that it can provide a dispersion tuning around zero dispersion. The advantage of using a dual-FBG configuration, in a tunable dispersion slope compensator, is that it can easily achieve a tuning of pure dispersion slope.

Based on the S-bending technique, we also demonstrate the application of a tunable fibre Bragg grating in controlling the output pulse width of a soliton fibre laser.

Chapter 8

Conclusions and future work

8.1 Summary

This thesis is devoted to the development and applications of new tunable fibre Bragg grating devices. One part concerns the optical phase en/decoders for reconfigurable OCDMA systems, and the other part describes the tunable fibre Bragg gratings based on an S-bending technique.

8.1.1 Optical phase en/decoders for OCDMA systems

Spatial phase-shifts in a fibre Bragg grating include discrete phase-shifts and (or) distributed phase-shifts. If a short optical pulse is reflected from a weak FBG, the spatial phase of the FBG will be inscribed into the temporal phase of the reflection pulse. This is called temporal phase encoding. Therefore, FBGs with a spatial phase distribution following a particular address code could be used as optical phase en/decoders in a temporal-phase-encoding OCDMA system.

In this thesis, we discuss three types of FBGs based OCDMA en/decoders as follows:

(1) *discrete-phase en/decoders*: having discrete phase-distributions with fixed codes,

(2) *reconfigurable-phase en/decoders*: having distributed phase-distributions with reconfigurable codes, and

(3) *continuous-phase en/decoders*: having distributed phase-distributions with fixed codes.

In addition, by simulation and experiments, we also compare OCDMA systems with three different configurations:

(a) discrete-phase encoders and discrete-phase decoders,

(b) discrete-phase encoders and continuous-phase decoders, and

(c) continuous-phase encoders and continuous-phase decoders.

Configuration (a) has the best autocorrelation and cross-correlation performance. However, configuration (c) has special advantages for dynamic reconfiguration and bandwidth saving, considering that for the same nominal code sequence, a reconfigurable-phase device has the same phase distribution as a continuous-phase device and a continuous-phase device has narrower bandwidth compared with a discrete-phase device.

In this thesis, the OCDMA system based on discrete-phase en/decoders is studied from the viewpoint of fibre Bragg gratings, in which the phase matching and mismatch between encoders and decoders are used to explain the autocorrelation, cross-correlation and their evolution under different device or system parameters, including grating strength, input pulse width, wavelength offset, chip number and chip length.

We make three major advancements in the area of the reconfigurable OCDMA system, which is one of the main topics for this thesis. Firstly, the pulse response method is introduced to accurately characterize the thermally induced dc refractive index variation in an FBG. The characterization reveals complete information on the spatial phase distribution of a reconfigurable-phase en/decoder, which is crucial because it is the basis for modelling, analyzing and designing of the reconfigurable OCDMA system. Secondly, the structure of the reconfigurable-phase device is improved so that it has a fast response speed. The reconfiguration is demonstrated to take less than two seconds. Thirdly, a new continuous-phase en/decoder is developed. It has a phase profile that matches the reconfigurable-phase device accurately and, therefore, when used with a reconfigurable-phase device, it provides a better performance than a system using discrete-phase encoders and reconfigurable-phase decoders.

8.1.2 Tunable fibre Bragg gratings based on the S-bending technique

An S-bending structure involves a uniform beam with two supported ends. By introducing a vertical displacement between the two supported ends, a linear strain field is formed, and its gradient is dependent on the amount of vertical displacement. In addition, the strain at the centre of the beam is always zero as the displacement varies. If a linearly chirped fibre Bragg grating is embedded into the uniform beam for S-bending, the variable linear strain field is applied on the FBG and thus the dispersion of the FBG could be altered by controlling the vertical displacement. The special advantage of tuning

an FBG using the S-bending technique is that the central wavelength of the FBG is invariant as the dispersion is altered.

In this thesis, new tunable devices are developed by embedding a pair of FBGs in one beam for S-bending. The FBG pair experiences the same strain field and, by cascading the two FBGs, new tuning functions are achieved. If only one single FBG is used for S-bending, it is difficult to change the sign of dispersion or achieve zero dispersion by tuning. By using a dual-FBG configuration, the combination of the two FBGs will result in a wide tuning range including zero dispersion. If only a single FBG is used for dispersion-slope tuning by S-bending, the dispersion of the FBG will also vary when its dispersion slope is altered. By using a dual-FBG configuration, the dispersion of the two FBGs has opposite signs and will always cancel, while the dispersion slopes of the two FBGs have the same sign and can be added, resulting in a pure dispersion slope compensator. In this thesis, a tunable dispersion compensator with a large tuning range is designed for application in a 40Gbit/s transmission system, and a tunable pure dispersion slope compensator is designed and fabricated for application in a 160Gbit/s transmission system.

The application of an S-bending fibre Bragg grating in controlling the pulse width of a soliton fibre laser is also demonstrated.

8.2 Future work

8.2.1 Thermal tuning techniques

The thermal tuning structure used in the reconfigurable-phase en/decoder is inherently a distributed tuning technique, in the sense that the property of a sub-section of FBG is only locally controlled by the tungsten wire in a direct contact. Owing to its high flexibility, this distributed tuning technique has great potential to provide complex dynamic reflection spectra and therefore can definitely find applications in many other areas, such as tunable dispersion or dispersion slope compensation [191] [205], and programmable pulse shaping [206].

To obtain an arbitrary reflection spectrum from a tunable FBG, a dc refractive index distribution with a complicated structure is required. Sometimes, for example in the reconfigurable-phase en/decoders or programmable pulse shaping, the thermally induced phase-shifts must be highly localized. We have characterized the dc refractive index

distribution as the diameter of wires is different. More work is required to achieve a localized thermal response for the FBGs. One possibility is to plate many minute metal wires, using the micro-fabrication technique, on the FBG, since this will ensure a compact contact and a good thermal conduction between the wire and the FBG. Another possibility is to use a series of miniature temperature controllers instead of the simple heaters on the FBG, so that the temperature is directly controlled at each point of the FBG [192].

8.2.2 Strain-tuning techniques

The S-bending tuning of fibre Bragg gratings is a simple but powerful technique, which can easily provide bandwidth tuning, dispersion tuning or dispersion-slope tuning. New devices and functions have been developed. Future work should be mainly focused on demonstrating their applications in optical systems. The application in an optical transmission system to dynamically compensate dispersion or dispersion slope is straightforward. An example of application in laser systems has been demonstrated in this thesis. The tunable grating is a fibre based device, which has a simple structure but can achieve flexible and complex functions. These apparent advantages imply that in any fibre system, if a dynamic bandwidth, dispersion or dispersion slope is required, this S-bending FBG device will always be the possible solution.

List of Publications

Journal Papers

[1] **Z. Zhang**, C. Tian, M. A. F. Roelens, M. R. Mokhtar, P. Petropoulos, D. J. Richardson, and M. Ibsen, " Direct characterization of the spatial effective refractive index profile in Bragg gratings ," *IEEE Photonics Technology Letters*, vol. 17, pp. 2685-2687, 2005.

[2] **Z. Zhang**, C. Tian, M. R. Mokhtar, P. Petropoulos, D. J. Richardson, and M. Ibsen, "Rapidly reconfigurable optical phase encoder-decoders based on fiber Bragg gratings," *IEEE Photonics Technology Letters*, vol. 18, pp. 1216-1218, 2006.

[3] C. Tian, **Z. Zhang**, M. Ibsen, P. Petropoulos, and D. J. Richardson, "A reconfigurable optical header recognition system for optical packet routing applications," *IEEE Photonics Technology Letters*, vol.18, pp. 2395-2397, 2006.

[4] **Z. Zhang**, C. Tian, P. Petropoulos, D. J. Richardson, and M. Ibsen, "Distributed-phase OCDMA encoder-decoders based on fiber Bragg gratings," *IEEE Photonics Technology Letters*, vol.19, pp. 574-576, 2007.

[5] C. Tian, **Z. Zhang**, M. Ibsen, P. Petropoulos, and D. J. Richardson, "A 16-channel OCDMA/DWDM system using continuous phase-shift SSFBGs and reconfigurable grating," *IEEE Journal of Selected Topics in Quantum Electronics* (submitted).

Conference Presentations

[1] **Z. Zhang**, C. Tian, M. A. F. Roelens, M. R. Mokhtar, P. Petropoulos, D. J. Richardson, and M. Ibsen, "Direct accurate determination of the spatial refractive index profile in Bragg gratings," *BGPP/ACOFT 2005,* Sydney, 4-8 Jul 2005, pp.75-77.

[2] C. Tian, **Z. Zhang**, M. A. F. Roelens, P. Petropoulos, , M. Ibsen, and D. J. Richardson, "Full characterisation of the temporal response of phase-shifted SSFBGs using electro-absorption modulator based frequency resolved optical gating," *BGPP/ACOFT 2005,* Sydney, 4-8 Jul 2005.

[3] P. Petropoulos, C. Tian, **Z. Zhang**, M. Ibsen, M. A. F. Roelens, P. C. Teh, and D. J. Richardson, "Applications of superstructured fibre Bragg gratings in OCDMA systems," *NOC 2005*, London, 5-7 Jul 2005 (Invited).

[4] C. Tian, **Z. Zhang**, M. A. F. Roelens, M. Ibsen, P. Petropoulos, and D. J. Richardson, "Reconfigurable all-optical header recognition for packet switched networks," *e-Photon /ONE Summer School* Pisa & Cesenatico, 30 Aug - 2 Sep 2005.

[5] M. A. F. Roelens, C. Tian, **Z. Zhang**, P. Petropoulos, M. Ibsen, and D. J. Richardson, "Full characterisation of the temporal response of complex phase shifted Bragg gratings for OCDMA using frequency resolved optical gating," *ECOC 2005*, Glasgow, 25-29 Sep 2005, Tu.4.6.5.

[6] **Z. Zhang**, C. Tian, M.R.Mokhtar, P.Petropoulos, D.J.Richardson, and M.Ibsen, "Rapidly reconfigurable phase code generation and recognition using fiber Bragg gratings," *OFC 2006*, Anaheim, 5-10 Mar 2006, OFF1.

[7] C. Tian, **Z. Zhang**, M. Ibsen, M.R.Mokhtar, P. Petropoulos, and D. J. Richardson, "Reconfigurable all-optical packet switching based on fiber Bragg gratings," *OFC 2006* Anaheim, 5-10 Mar 2006, OFJ4.

[8] **Z. Zhang**, C. Tian, P. Petropoulos, D. J. Richardson, and M. Ibsen, "Fibre Bragg grating based continuous-phase encoder-decoders for OCDMA networks," *ECOC 2006*, Cannes, 24-28 Sep 2006, We.3.P.38.

[9] C. Tian, **Z. Zhang**, M. Ibsen, P. Petropoulos, and D. J. Richardson, "Demonstration of a 16-channel code-reconfigurable OCDMA/DWDM system," *OFC 2007*, Anaheim, 25-29 Mar 2007, OMO2.

[10] T.T. Ng, F. Parmigiani, M. Ibsen, **Z. Zhang**, P. Petropoulos and D.J. Richardson, "Linear-distortion compensation using XPM with parabolic pulses," *OFC 2007*, Anaheim, 25-29 Mar 2007, JWA58.

Bibliography

[1] R. Kashyap, *Fibre Bragg Gratings*, Academic Press, 1999.

[2] A. Othonos, and K. Kalli, *Fibre Bragg Gratings: Fundamental and Applications in Telecommunications and sensing*, Artech House Inc., 1999.

[3] C. R. Giles, "Lightwave applications of fibre Bragg gratings," *Journal of Lightwave Technology*, vol. 15, pp. 1391-1404, 1997.

[4] J. L. Archambault and S. G. Grubb, "Fibre gratings in lasers and amplifiers," *Journal of Lightwave Technology*, vol. 15, pp. 1378-1390, 1997.

[5] A. D. Kersey, M. A. Davis, H. J. Patrick, M. LeBlanc, K. P. Koo, C. G. Askins, M. A. Putnam, and E. J. Friebele, "Fibre grating sensors," *Journal of Lightwave Technology*, vol. 15, pp. 1442-1463, 1997.

[6] P. C. Teh, P. Petropoulos, M. Ibsen, and D. J. Richardson, "A comparative study of the performance of seven-and 63-chip optical code-division multiple-access encoders and decoders based on superstructured fibre Bragg gratings," *Journal of Lightwave Technology*, vol.19, pp.1352-1365, 2001.

[7] L. E. Nelson, "Challenges of 40 Gb/s WDM transmission," *OFC 2001* Anaheim, CA, Mar. 17-22, 2001 ThF1.

[8] R. Ludwig, U. Feiste, C. Schmidt C. Schubert, J. Berger, E. Hilliger, M. Kroh, T. Yamamoto, C. M. Weinert and H. G. Weber, , "Enabling transmission at 160 Gbit/s," *OFC 2002* Anaheim, CA, Mar. 17-22, 2002 TuA1.

[9] M. R. Mokhtar, M. Ibsen, P. C. Teh, and D. J. Richardson, "Reconfigurable multilevel phase-shift keying encoder-decoder for all-optical networks," *IEEE Photonics Technology Letters*, vol. 15, pp. 431-433, 2003.

[10] T. Imai, T. Komukai, and M. Nakazawa, "Dispersion tuning of a linearly chirped fibre Bragg grating without a center wavelength shift by applying a strain gradient," *IEEE Photonics Technology Letters*, vol. 10, pp. 845-847, 1998

[11] C.Dorrer and I. Kang, "Real-time implementation of linear spectrograms for the characterization of high bit-rate optical pulse trains," *IEEE Photonics Technology Letters*, vol. 16, pp. 858-860, 2004.

[12] M. Born and E. Wolf, *Principles of Optics*, Cambridge University Press, Cambridge, 1999.

[13] T. Erdogan, "Fibre grating spectra," *Journal of Lightwave Technology*, vol. 15, pp. 1277-1294, 1997.

[14] H. Kogelnik, "Theory of Optical Waveguides," in *Guided-Wave Optoelectronics*, T. Tamir, Ed. New York: Springer-Verlag, 1990.

[15] D. Marcuse, *Theory of Dielectric Optical Waveguides*, Academic Press, New York, 1984

[16] L. Poladian, "Resonance mode expansions and exact solutions for nonuniform gratings," *Physical Review E*, vol. 54, pp. 2963-2975, 1996.

[17] P. St. J. Russell, "Bloch wave analysis of dispersion and pulse propagation in pure distributed feedback structures," *Journal of Modern Optics*, vol. 38, pp.1599-1619, 1991.

[18] W. H. Press, S. A. Teukolsky, W. T. Veterling, and B. P. Flannery, *Numerical Recipes, the Art of Scientific Computing*, 2nd ed. Cambridge U. Press, New York, 1992.

[19] M. Yamada and K. Sakuda, "Analysis of almost-periodic distributed feedback slab waveguides via a fundamental matrix approach," *Applied Optics*, vol. 26, pp.3474-3478, 1987.

[20] H. Kogelnik, "Filter response of nonuniform almost-periodic structures," *Bell System Technical Journal*, vol. 55, pp. 109-126, 1976.

[21] L. Poladian, "Simple grating synthesis algorithm," *Optics Letters*, vol.25, pp. 787-789, 2000.

[22] R. Feced, M. N. Zervas and M. A. Muriel, " An efficient inverse scattering algorithm for the design of nonuniform fibre Bragg gratings," *IEEE Journal of Quantum Electronics*, vol. 35, pp. 1105-1115, 1999.

[23] J. Skaar, L. G. Wang, and T. Erdogan, "On the synthesis of fibre Bragg gratings by layer peeling," *IEEE Journal of Quantum Electronics*, vol. 37, pp.165-173, 2001.

[24] J. Skaar and O. H. Waagaard, "Design and characterization of finite-length fibre gratings," *IEEE Journal of Quantum Electronics*, vol. 39, pp. 1238-1245, 2003.

[25] A. Rosenthal and M. Horowitz, "Inverse scattering algorithm for reconstructing strongly reflecting fiber Bragg gratings," *IEEE Journal of Quantum Electronics*, vol. 39, pp. 1018-1026, 2003.

[26] P. J. Lemaire, R. M. Atkins, V. Mizrahi, and W. A. Reed, "High-pressure H_2 loading as a technique for achieving ultrahigh UV photosensitivity and thermal sensitivity in GeO_2 doped optical fibers," *Electronics Letters*, vol. 29, pp. 1191-1193, 1993.

[27] R. M. Atkins, P. J. Lemaire, T. Erdogan, and V. Mizrahi, "Mechanisms of enhanced UV photosensitivity via hydrogen loading in germanosilicate glasses," *Electronics Letters*, vol. 29, pp. 1234-1235, 1993.

[28] K. O. Hill, Y. Fujii, D. C. Johnson, and B. S. Kawasaki, "Photosensitivity in optical fiber waveguides-application to reflection filter fabrication," *Applied Physics Letters*, vol. 32, pp. 647-649, 1978.

[29] G. Meltz, W. W. Morey, and W. H. Glenn, "Formation of Bragg gratings in optical fibers by a transverse holographic method," *Optics Letters*, vol. 14, pp. 823-825, 1989.

[30] K. O. Hill, B. Malo, F. Bilodeau, D. C. Johnson, and J. Albert, "Bragg gratings fabricated in monomode photosensitive optical fiber by UV exposure through a phase mask," *Applied Physics Letters*, vol. 62, pp. 1035-1037, 1993.

[31] K. O. Hill and G. Meltz, "Fiber Bragg grating technology fundamentals and overview," *Journal Of Lightwave Technology*, vol. 15, pp. 1263-1276, 1997.

[32] M. J. Cole, W. H. Loh, R.I.Laming, M.N.Zervas, and S.Barcelos, "Moving fibre/phase mask-scanning beam technique for enhanced flexibility in producing fibre gratings with a uniform phase mask," *Electronics Letters,* Vol.31, pp.1488-1489, 1995.

[33] W. H. Loh, M. J. Cole, M.N.Zervas, S.Barcelos, and R.I.Laming, "Complex grating structures with uniform phase masks based on the moving fibre-scanning beam technique," *Optics Letters,* Vol.20(20) pp.2051-2053, 1995

[34] A. Asseh, H. Storoy, B. E. Sahlgren, S. Sandgren, and R. A. H. Stubbe, "A writing technique for long fiber Bragg gratings with complex reflectivity profiles," *Journal Of Lightwave Technology*, vol. 15, pp. 1419-1423, 1997.

[35] H. Storoy, H. E. Engan, B. Sahlgren, and R. Stubbe, "Position weighting of fiber Bragg gratings for bandpass filtering," *Optics Letters*, vol. 22, pp. 784-786, 1997.

[36] M.Ibsen, M.Durkin, M.J.Cole, M.N.Zervas, and R.I.Laming, "Recent advances in long dispersion compensating fibre Bragg gratings," *IEE Colloquium on Optical Fibre Gratings*, Birmingham, 6/1-6/7, 1999.

[37] I. Petermann, B. Sahlgren, S. Helmfrid, A. T. Friberg, and P. Y. Fonjallaz, "Fabrication of advanced fiber Bragg gratings by use of sequential writing with a continuous-wave ultraviolet laser source," *Applied Optics*, vol. 41, pp. 1051-1056, 2002.

[38] Y. S. Liu, L. Dong, J. J. Pan, and C. Gu, "Strong phase-controlled fiber Bragg gratings for dispersion compensation," *Optics Letters*, vol. 28, pp. 786-788, 2003

[39] Y. Liu, J. J. Pan, and C. Gu, "Novel fiber Bragg grating fabrication method with high-precision phase control," *Optical Engineering*, vol. 43, pp. 1916-1922, 2004.

[40] J. F. Brennan, "Broadband fibre Bragg gratings for dispersion management," *Journal of Optical and Fiber Communications Reports*, vol. 2, pp. 397-434, 2005.

[41] U. Eriksson, P. Blixt, and J. A. Tellefsen, "Design of fiber gratings for total dispersion compensation," *Optics Letters*, vol. 19, pp. 1028-1030, 1994.

[42] J. Skaar and R. Feced, "Reconstruction of gratings from noisy reflection data," *Journal of the Optical Society of America A,* vol. 19, pp. 2229-2237, 2002.

[43] L. Poladian, B. Ashton, W. E. Padden, A. Michie, and C. Marra, "Characterisation of phase-shifts in gratings fabricated by over-dithering and simple displacement," *Optical Fiber Technology*, vol. 9, pp. 173-188, 2003.

[44] S. E. Mechels, J. B. Schlager, and D. L. Franzen, "Accurate measurements of the zero-dispersion wavelength in optical fibers," *Journal of Research of the National Institute of Standards and Technology*, vol. 102, pp. 333-347, 1997.

[45] M. Lacerda-Rocha and R. Kashyap, "Repeatibility in the characterization of chirped Bragg gratings," in Proc. Optical Fibers Measurements Conference, OFMC'98, (1998)

[46] S. Barcelos, M.N. Zervas, R. I. Laming and D. N. Payne, "Interferometric fibre grating characterization," IEE Colloquium on Optical Fibre Gratings and their Applications, pp.5/1-5/7, 1995.

[47] P. Lambelet, P. Y. Fonjallaz, H. G. Limberger, R. P. Salathe, C. Zimmer, and H. H. Gilgen, "Bragg Grating Characterization by Optical Low-Coherence Reflectometry," *IEEE Photonics Technology Letters*, vol. 5, pp. 565-567, 1993.

[48] A. Kohlhaas, C. Fromchen, and E. Brinkmeyer, "High-resolution OCDR for testing integrated-optical wave-guides - dispersion-corrupted experimental-data corrected by a numerical algorithm," *Journal of Lightwave Technology*, vol. 9, pp. 1493-1502, 1991.

[49] D. Leduc, X. Chapeleau, C. Lupi, R. Le Ny, and C. Boisrobert, "Accurate low-coherence interferometric relative group delay and reflectance measurements: characterization of a free-space optics multiplexer/demultiplexer," *Journal Of Optics A-Pure And Applied Optics*, vol. 5, pp. S124-S128, 2003.

[50] U. Wiedmann, P. Gallion, and G. H. Duan, "A generalized approach to optical low-coherence reflectometry including spectral filtering effects," *Journal Of Lightwave Technology*, vol. 16, pp. 1343-1347, 1998.

[51] E. I. Petermann, J. Skaar, B. E. Sahlgren, R. A. H. Stubbe, and A. T. Friberg, "Characterization of fibre Bragg gratings by use of optical coherence-domain reflectometry," *Journal of Lightwave Technology*, vol. 17, pp. 2371-2378, 1999.

[52] E. I. Petermann, B. E. Sahlgren, J. Skaar, P. Fonjallaz, and R. A. H. Stubbe, "Phase distribution measurement of fibre Bragg gratings with white light interferometry," *ECOC'98*, paper WdA09, 1998, pp. 399-400.

[53] S. D. Dyer, K. B. Rochford, and A. H. Rose, "Fast and accurate low-coherence interferometric measurements of fiber Bragg grating dispersion and reflectance," *Optics Express*, vol. 5, pp. 262-266, 1999.

[54] E. Brinkmeyer, "Simple algorithm for reconstructing fiber gratings from reflectometric data," *Optics Letters*, vol. 20, pp. 810-812, 1995.

[55] D. W. Huang and C. C. Yang, "Reconstruction of fiber grating refractive-index profiles from complex Bragg reflection spectra," *Applied Optics*, vol. 38, pp. 4494-4499, 1999.

[56] P. Giaccari, H. G. Limberger, and R. P. Salathe, "Local coupling-coefficient characterization in fiber Bragg gratings," *Optics Letters*, vol. 28, pp. 598-600, 2003.

[57] S. Keren, A. Rosenthal, and M. Horowitz, "Measuring the structure of highly reflecting fiber Bragg gratings," *IEEE Photonics Technology Letters*, vol. 15, pp. 575-577, 2003.

[58] X. Chapeleau, D. Leduc, C. Lupi, F. Lopez-Gejo, M. Douay, R. Le Ny, and C. Boisrobert, "Local characterization of fiber-Bragg gratings through combined use of low-coherence interferometry and a layer-peeling algorithm," *Applied Optics*, vol. 45, pp. 728-735, 2006.

[59] P. A. Krug, R. Stolte, and R. Ulrich, "Measurement of index modulation along an optical-fiber Bragg grating," *Optics Letters*, vol. 20, pp. 1767-1769, 1995.

[60] F. El-Diasty, A. Heaney, and T. Erdogan, "Analysis of fiber Bragg gratings by a side-diffraction interference technique," *Applied Optics*, vol. 40, pp. 890-896, 2001.

[61] I. Petermann, S. Helmfrid, and A. T. Friberg, "Limitations of the interferometric side diffraction technique for fibre Bragg grating characterization," *Optics Communications*, vol. 201, pp. 301-308, 2002.

[62] L. M. Baskin, M. Sumetsky, P. S. Westbrook, P. I. Reyes, and B. J. Eggleton, "Accurate characterization of fiber Bragg grating index modulation by side-diffraction technique," *IEEE Photonics Technology Letters*, vol. 15, pp. 449-451, 2003.

[63] M. Aslund, J. Canning, and L. Poladian, "Novel characterization technique with 0.5 ppm spatial accuracy of fringe period in Bragg gratings," *Optics Express*, vol. 11, pp. 838-842, 2003.

[64] W. Margulis, I. C. S. Carvalho, P. M. P. Gouvea, and B. Lesche, "Heat scan - a simple technique to study gratings in fibers," *Optics Letters*, vol. 18, pp. 1016-1018, 1993.

[65] E. Ronnekleiv, M. Ibsen, M. N. Zervas, and R. I. Laming, "Characterization of fiber distributed-feedback lasers with an index-perturbation method," *Applied Optics*, vol. 38, pp. 4558-4565, 1999.

[66] J. P. vonderWeid, R. Passy, G. Mussi, and N. Gisin, "On the characterization of optical fiber network components with optical frequency domain reflectometry," *Journal Of Lightwave Technology*, vol. 15, pp. 1131-1141, 1997.

[67] O. H. Waagaard, "Spatial characterization of strong fiber Bragg gratings using thermal chirp and optical-frequency-domain reflectometry," *Journal Of Lightwave Technology*, vol. 23, pp. 909-914, 2005.

[68] N. M. Litchinitser, B. J. Eggleton, and G. P. Agrawal, "Dispersion of cascaded fiber gratings in WDM lightwave systems," *Journal Of Lightwave Technology*, vol. 16, pp. 1523-1529, 1998.

[69] C. Spiegelberg, J. H. Geng, Y. D. Hu, Y. Kaneda, S. B. Jiang, and N. Peyghambarian, "Low-noise narrow-linewidth fiber laser at 1550 nm (June 2003)," *Journal Of Lightwave Technology*, vol. 22, pp. 57-62, 2004.

[70] J. H. Geng, C. Spiegelberg, and S. B. Jiang, "Narrow linewidth fiber laser for 100-km optical frequency domain reflectometry," *IEEE Photonics Technology Letters*, vol. 17, pp. 1827-1829, 2005.

[71] F. Ouellette, "Dispersion cancellation using linearly chirped Bragg grating filters in optical wave-guides," *Optics Letters*, vol. 12, pp. 847-849, 1987.

[72] A. Galvanauskas, M. E. Fermann, D. Harter, K. Sugden, and I. Bennion, "All-fiber femtosecond pulse amplification circuit using chirped Bragg gratings," *Applied Physics Letters*, vol. 66, pp. 1053-1055, 1995.

[73] K. Kim, S. Lee, and P. J. Delfyett, "1.4kW high peak power generation from an all semiconductor mode-locked master oscillator power amplifier system based on eXtreme Chirped Pulse Amplification(X-CPA)," *Optics Express*, vol. 13, pp. 4600-4606, 2005.

[74] W. H. Loh, and R. I. Laming, "1.55um phase-shifted distributed feedback lasers," *Electronics Letters*, vol. 31, pp. 1440-1442, 1995.

[75] M. Ibsen, R. Feced, J.A.J.Fells, and W.S.Lee, "40Gbit/s high performance filtering for DWDM networks employing dispersion-free fibre Bragg gratings," *ECOC 2001* Amsterdam 30 Sep-4 Oct 2001 Th.B.2.1.

[76] M. Ibsen, and R. Feced, "Fibre Bragg gratings for pure dispersion-slope compensation," *Optics Letters*, Vol.28, pp.980-982, 2003.

[77] P. Petropoulos, M. Ibsen, A. D. Ellis, and D. J. Richardson, "Rectangular pulse generation based on pulse reshaping using a superstructured fiber Bragg grating," *Journal of Lightwave Technology*, vol. 19, pp. 746-752, 2001.

[78] P. Petropoulos, M. Ibsen, M. N. Zervas, and D. J. Richardson, "Generation of a 40-GHz pulse stream by pulse multiplication with a sampled fiber Bragg grating," *Optics Letters*, vol. 25, pp. 521-523, 2000.

[79] J. B. Khurgin, "Light slowing down in Moire fiber gratings and its implications for nonlinear optics," *Physical Review A*, vol. 62, 013821, 2000.

[80] D. Janner, G. Galzerano, G. Della Valle, P. Laporta, S. Longhi, and M. Belmonte, "Slow light in periodic superstructure Bragg gratings," *Physical Review E*, vol. 72, 056605, 2005.

[81] S. Longhi, D. Janner, G. Galzerano, G. Della Valle, D. Gatti, and P. Laporta, "Optical buffering in phase-shifted fibre gratings," *Electronics Letters*, vol. 41, pp. 1075-1077, 2005.

[82] S. M. Wang, H. Erlig, H. R. Fetterman, E. Yablonovitch, V. Grubsky, D. S. Starodubov, and J. Feinberg, "Group velocity dispersion cancellation and additive group delays by cascaded fiber Bragg gratings in transmission," *IEEE Microwave And Guided Wave Letters*, vol. 8, pp. 327-329, 1998.

[83] J. F. Brennan, and D. L. LaBrake, "Realization of >10m-long chirped fibre Bragg gratings," *Proc. OSA BGPP*, Washington, DC, 1999, pp35-37.

[84] J. F. Brennan, M. R. Matthews, W. V. Dower, D. J. Treadwell, W. Wang, J. Porque, and X. D. Fan, "Dispersion correction with a robust fibre grating over the full C-band at 10-Gb/s rates with < 0.3-dB power penalties," *IEEE Photonics Technology Letters*, vol. 15, pp. 1722-1724, 2003.

[85] Y. Painchaud, H. Chotard, A. Mailloux, and Y. Vasseur, "Superposition of chirped fibre Bragg grating for third-order dispersion compensation over 32 WDM channels," *Electronics Letters*, vol. 38, pp. 1572-1573, 2002.

[86] R. Lachance, S. Lelievre and Y. Painchaud, "50 and 100GHz multi-channel tunable chromatic dispersion slope compensator," *OFC 2003* Atlanta, 23 – 28 Mar, 2003 TuD3

[87] A. Doyle, C. Juignet, Y. Painchaud, M. Brown, N. Chummun-Courbet, E. Pelletier, and M. Guy, "FBG-based multi-channel low dispersion WDM filters," *Electronics Letters*, vol. 38, pp. 1561-1563, 2002.

[88] S. Legoubin, M. Douay, P. Bernage, P. Niay, S. Boj, and E. Delevaque, "Free spectral range variations of grating-based Fabry-Perot filters photowritten in optical fibers," *Journal of the Optical Society of America A-Optics Image Science and Vision*, vol. 12, pp. 1687-1694, 1995.

[89] G. E. Town, K. Sugden, J. A. R. Williams, W. I. Bennion, and S. B. Poole, "Wide-band Fabry-Perot-like filters in optical-fiber," *IEEE Photonics Technology Letters*, vol. 7, pp. 78-80, 1995.

[90] S. Doucet, R. Slavik, and S. LaRochelle, "High-finesse large band Fabry-Perot fibre filter with superimposed chirped Bragg gratings," *Electronics Letters*, vol. 38, pp. 402-403, 2002.

[91] R. Slavik, S. Doucet, and S. LaRochelle, "High-performahce all-fiber Fabry-Perot filters with superimposed chirped Bragg gratings," *Journal Of Lightwave Technology*, vol. 21, pp. 1059-1065, 2003.

[92] L. A. Everall, K. Sugden, J. A. R. Williams, I. Bennion, X. Liu, J. S. Aitchison, S. Thoms, and K. M. DelaRue, "Fabrication of multipassband moire resonators in fibers by the dual-phase-mask exposure method," *Optics Letters*, vol. 22, pp. 1473-1475, 1997.

[93] R. Slavik and S. LaRochelle, "Large-band periodic filters for DWDM using multiple-superimposed fiber Bragg gratings," *IEEE Photonics Technology Letters*, vol. 14, pp. 1704-1706, 2002.

[94] S. Doucet, R. Slavik, and S. LaRochelle, "Tunable dispersion, and dispersion slope compensator using novel Gires-Tournois Bragg grating coupled-cavities," *IEEE Photonics Technology Letters*, vol. 16, pp. 2529-2531, 2004.

[95] R. Slavik and S. LaRochelle, "All-fiber periodic filters for DWDM using a cascade of FIR and IIR lattice filters," *IEEE Photonics Technology Letters*, vol. 16, pp. 497-499, 2004.

[96] B. B. Dingel and M. Izutsu, "Multifunction optical filter with a Michelson-Gires-Tournois interferometer for wavelength-division-multiplexed network system applications," *Optics Letters*, vol. 23, pp. 1099-1101, 1998.

[97] X. W. Shu, K. Sugden, and I. Bennion, "Novel multipassband optical filter using all-fiber Michelson-Gires-Tournois structure," *IEEE Photonics Technology Letters*, vol. 17, pp. 384-386, 2005.

[98] Q. J. J. Wang, Y. Zhang, and Y. C. Soh, "Efficient structure for optical interleavers using superimposed chirped fiber Bragg gratings," *IEEE Photonics Technology Letters*, vol. 17, pp. 387-389, 2005.

[99] X. W. Shu, K. Sugden, and K. Byron, "Bragg-grating-based all-fibre distributed Gires-Tournois etalons," *Optics Letters*, vol. 28, pp. 881-883, 2003.

[100] X. W. Shu, K. Sugden, P. Rhead, J. Mitchell, I. Felmeri, G. Lloyd, K. Byron, Z. J. Huang, I. Khrushchev, and I. Bennion, "Tunable dispersion compensator based on distributed Gires- Tournois etalons," *IEEE Photonics Technology Letters*, vol. 15, pp. 1111-1113, 2003.

[101] X. W. Shu, K. Chisholm, and K. Sugden, "Design and realization of dispersion slope compensators using distributed Gires-Tournois etalons," *IEEE Photonics Technology Letters*, vol. 16, pp.1092-1094, 2004.

[102] X. W. Shu, I. Bennion, J. Mitchell, and K. Sugden, "Tailored Gires-Tournois etalons as tunable dispersion slope compensators," *Optics Letters*, vol. 29, pp. 1814-1814, 2004.

[103] V. Jayaraman, Z. M. Chuang, and L. A. Coldren, "Theory, design, and performance of extended tuning range semiconductor-lasers with sampled gratings," *IEEE Journal Of Quantum Electronics*, vol. 29, pp. 1824-1834, 1993.

[104] H. Ishii, H. Tanobe, F. Kano, Y. Tohmori, Y. Kondo, and Y. Yoshikuni, "Quasicontinuous wavelength tuning in super-structure-grating (SSG) DBR lasers," *IEEE Journal Of Quantum Electronics*, vol. 32, pp. 433-441, 1996.

[105] B. J. Eggleton, P. A. Krug, L. Poladian, and F. Ouellette, "Long periodic superstructure Bragg gratings in optical fibers," *Electronics Letters*, vol. 30, pp. 1620-1622, 1994.

[106] F. Ouellette, P. A. Krug, T. Stephens, G. Dhosi, and B. Eggleton, "Broad-band and WDM dispersion compensation using chirped sampled fiber Bragg gratings," *Electronics Letters*, vol. 31, pp. 899-901, 1995.

[107] M. Ibsen, M. K. Durkin, M. J. Cole, and R. I. Laming, "Sinc-sampled fiber Bragg gratings for identical multiple wavelength operation," *IEEE Photonics Technology Letters*, vol. 10, pp. 842-844, 1998.

[108] J. E. Rothenberg, H. Li, Y. Li, J. Popelek, Y. Sheng, Y. Wang, R. B. Wilcox, and J. Zweiback, "Dammann fiber Bragg gratings and phase-only sampling for high channel counts," *IEEE Photonics Technology Letters*, vol. 14, pp. 1309-1311, 2002.

[109] J. E. Rothenberg, F. Babian, Z. Brodzeli, P.Chou, H. Li, Y. Li, J. Popelek, R. Wilcox, "Phase-only sampling for fabrication and design of high-channel-count fibre Bragg gratings," *OFC 2003* Atlanta, 23 – 28 Mar, 2003 ThL3.

[110] A. V. Buryak, K. Y. Kolossovski, and D. Y. Stepanov, "Optimization of refractive index sampling for multichannel fiber Bragg gratings," *IEEE Journal Of Quantum Electronics*, vol. 39, pp. 91-98, 2003.

[111] H. P. Li, Y. L. Sheng, Y. Li, and J. E. Rothenberg, "Phased-only sampled fiber Bragg gratings for high-channel-count chromatic dispersion compensation," *Journal Of Lightwave Technology*, vol. 21, pp. 2074-2083, 2003.

[112] H. Lee and G. P. Agrawal, "Add-drop multiplexers and interleavers with broad-band chromatic dispersion compensation based on purely phase-sampled fiber gratings," *IEEE Photonics Technology Letters*, vol. 16, pp. 635-637, 2004.

[113] K. Y. Kolossovski, R. A. Sammut, A. V. Buryak, and D. Y. Stepanov, "Three-step design optimization for multi-channel fibre Bragg gratings," *Optics Express*, vol. 11, pp. 1029-1038, 2003.

[114] W. H. Loh, F. Q. Zhou, and J. J. Pan, "Novel designs for sampled grating-based multiplexers-demultiplexers," *Optics Letters*, vol. 24, pp. 1457-1459, 1999.

[115] W. H. Loh, F. Q. Zhou, and J. J. Pan, "Sampled fiber grating based-dispersion slope compensator," *IEEE Photonics Technology Letters*, vol. 11, pp. 1280-1282, 1999.

[116] H. Lee and G. P. Agrawal, "Purely phase-sampled fiber Bragg gratings for broad-band dispersion and dispersion slope compensation," *IEEE Photonics Technology Letters*, vol. 15, pp. 1091-1093, 2003.

[117] C. H. Wang, L. R. Chen, and P. W. E. Smith, "Analysis of chirped-sampled and sampled-chirped fiber Bragg gratings," *Applied Optics*, vol. 41, pp. 1654-1660, 2002.

[118] G. A. Ball and W. W. Morey, "Compression-tuned single-frequency Bragg grating fiber laser," *Optics Letters*, vol. 19, pp. 1979-1981, 1994.

[119] M. R. Mokhtar, C. S. Goh, S. A. Butler, S. Y. Set, K. Kikuchi, D. J. Richardson, and M. Ibsen, "Fibre Bragg grating compression-tuned over 110 nm," *Electronics Letters*, vol. 39, pp. 509-511, 2003.

[120] M.A.F.Roelens, B. C. Thomsen, and D.J.Richardson, "High quality 5ps pulse generation at 10 Gbit/s using a fibre Bragg grating compensated gain-switched laser diode," *OECC 2004*, Yokohama, 12-16 Jul 2004, 16D1-4.

[121] R. Trebino , Kenneth W. DeLong, David N. Fittinghoff, John N. Sweetser, Marco A. Krumbügel, and Bruce A. Richman, "Measuring ultrashort laser pulses in the time-frequency domain using frequency-resolved optical gating," *Review of Scientific Instruments*, vol. 68, pp. 3277-3295, 1997.

[122] K. W. Delong, D. N. Fittinghoff, R. Trebino, B. Kohler, and K. Wilson, "Pulse retrieval in frequency-resolved optical gating based on the method of generalized projections," *Optics Letters*, vol. 19, pp. 2152-2154, 1994.

[123] K. W. Delong and R. Trebino, "Improved ultrashort pulse-retrieval algorithm for frequency-resolved optical gating," *Journal of the Optical Society of America A-Optics Image Science and Vision*, vol. 11, pp. 2429-2437, 1994.

[124] C. Dorrer and I. Kang, "Simultaneous temporal characterization of telecommunication optical pulses and modulators by use of spectrograms," *Optics Letters*, vol. 27, pp. 1315-1317, 2002.

[125] M.A.F.Roelens, "Precise intensity and phase characterisation of optical tele-communication signals," PhD thesis, Optoelectronics Research Centre, University of Southampton, July 2006.

[126] M.A.F.Roelens, C.Tian, Z.Zhang, P.Petropoulos, M.Ibsen, and D.J.Richardson, "Full characterisation of the temporal response of complex phase shifted Bragg gratings for OCDMA using frequency resolved optical gating," *ECOC 2005* Glasgow 25-29 Sep 2005, paper Tu.4.6.5.

[127] L. R. Chen, S. D. Benjamin, and P. W. E. Smith, "Ultrashort pulse reflection from fiber gratings: a numerical investigation," *Journal of Lightwave Technology*, vol. 15, pp. 1503-1512, 1997.

[128] M. Ibsen, and R. I. Laming, "Fiber non-uniformity caused Bragg grating imperfections," *OFC'99*, San Diego, Feb 21-26, 1999, Paper FA1.

[129] P. R. Prucnal and M. A. Santoro, "Spread spectrum fiberoptic local area network using optical-processing," *Journal of Lightwave Technology*, vol. 4, pp. 547-554, 1986.

[130] J. Shah, "Optical CDMA," *Optics & Photonics News*, vol. 14, pp. 42-47, 2003.

[131] J. G. Proakis, *Digital Communications*, 4th Edition, McGraw-Hill, 2001.

[132] M. E. Marhic, "Coherent Optical CDMA Networks," *Journal of Lightwave Technology*, vol. 11, pp. 854-864, 1993.

[133] N. Wada and K. Kitayama, "A 10 Gb/s optical code division multiplexing using 8-chip optical bipolar code and coherent detection," *Journal of Lightwave Technology*, vol. 17, pp. 1758-1765, 1999.

[134] D. Zaccarin and M. Kavehrad, "An optical CDMA system based on spectral encoding of LED," *IEEE Photonics Technology Letters*, vol. 5, pp. 479-482, 1993.

[135] H. P. Sardesai, C. C. Chang, and A. M. Weiner, "A femtosecond code-division multiple-access communication system test bed," *Journal of Lightwave Technology*, vol. 16, pp. 1953-1964, 1998.

[136] K. Li, W. Cong, V.J. Hernandez, R.P. Scott, J. Cao, Y. Du, J. P. Heritage, B. H. Kolner, and S. J. B. Yoo, "10 Gbit/s optical OCDMA encoder-decoder BER performance using HNLF thresholder," *OFC 2004* 24-26 Feb 2004 MF87.

[137] H. Fathallah and L. A. Rusch, "Robust optical FFH-CDMA communications: Coding in place of frequency and temperature controls," *Journal of Lightwave Technology*, vol. 17, pp. 1284-1293, 1999.

[138] H. Fathallah, L. A. Rusch, and S. LaRochelle, "Passive optical fast frequency-hop CDMA communications system," *Journal of Lightwave Technology*, vol. 17, pp. 397-405, 1999.

[139] L. R. Chen, S. D. Benjamin, P. W. E. Smith, and J. E. Sipe, "Applications of ultrashort pulse propagation in Bragg gratings for wavelength-division multiplexing and code-division multiple recess," *IEEE Journal of Quantum Electronics*, vol. 34, pp. 2117-2129, 1998.

[140] H. B. Jaafar, S. LaRochelle, P. Y. Cortes, and H. Fathallah, "1.25 Gbit/s transmission of optical FFH-OCDMA signals over 80 km with 16 users," *OFC 2001*, 17-22 Mar, 2001 TuV3.

[141] H. Geiger, A. Fu, P. Petropoulos, M. Ibsen, D. J. Richardson and R. I. Laming, "Demonstration of simple CDMA transmitter and receiver using sampled fiber gratings," *ECOC'98*, vol.1, 1998, pp. 337-338.

[142] P. C. Teh, P. Petropoulos, M. Ibsen, and D. J. Richardson, "Phase encoding and decoding of short pulses at 10 Gb/s using superstructured fiber Bragg gratings," *IEEE Photonics Technology Letters*, vol. 13, pp. 154-156, 2001.

[143] P. Petropoulos, N. Wada, P. C. Teh, M. Ibsen, W. Chujo, K. I. Kitayama, and D. J. Richardson, "Demonstration of a 64-chip OCDMA system using superstructured fiber gratings and time-gating detection," *IEEE Photonics Technology Letters*, vol. 13, pp. 1239-1241, 2001

[144] P. C. Teh, M. Ibsen, J. H. Lee, P. Petropoulos, and D. J. Richardson, "Demonstration of a four-channel WDM/OCDMA system using 255-chip 320-Gchip/s quarternary phase coding gratings," *IEEE Photonics Technology Letters*, vol. 14, pp. 227-229, 2002.

[145] S. Kutsuzawa, S. Oshiba, A. Nishiki, S. Kobayashi, and H. Iwamura, "Phase-coding OCDMA using fiber-Bragg-grating with enlarged signal pulse width," *OFC 2003*, 23-28 Mar, 2003 MF109.

[146] X. Wang, K. Matsushima, K. I. Kitayama, A. Nishiki, and S. Oshiba, "Demonstration of the improvement of apodized 127-chip SSFBG in coherent time-spreading OCDMA network," *OFC 2004* 24-26 Feb 2004 MF74.

[147] X. Wang, K. Matsushima, A. Nishiki, N. Wada, and K. I. Kitayama, "High reflectivity superstructured FBG for coherent optical code generation and recognition," *Optics Express* 12, 5457-5468 (2004)

[148] X. Wang, and K, Kitayama, "Analysis of beat noise in coherent and incoherent time-spreading OCDMA," *Journal of Lightwave Technology*, vol.22, pp.2226-2235, 2004.

[149] X. Wang, N. Wada, T. Hamanaka, and K, Kitayama, "10-user, truly-asynchronous OCDMA experiment with 511-chip SSFBG en/decoder and SC-based optical thresholder," *OFC 2005*, PDP33.

[150] X. Wang, K. Matsushima, K. -i. Kitayama, A. Nishiki, N. Wada, and F. Kubota, "High-performance optical code generation and recognition by use of a 511-chip, 640-Gchip/s phase-shifted superstructured fiber Bragg grating," *Optics Letters*, 30, 355-357 (2005)

[151] E. H. Dinan and B. Jabbari, "Spreading codes for direct sequence CDMA and wideband CDMA cellular networks," *IEEE Communications Magazine*, vol. 36, pp. 48-54, 1998.

[152] S. Boztas, R. Hammons and P. V. Kumar, "4-phase sequences with near optimum correlation properties,"*IEEE Transactions on Information Theory*, vol. 38, pp. 1101-1113, 1992.

[153] M. R. Mokhtar, "Bragg grating filters for optical networks," PhD thesis, Optoelectronics Research Centre, University of Southampton, Jan 2005.

[154] C. Tian, Z. Zhang, M. Ibsen, M. R. Mokhtar, P. Petropoulos, and D. J. Richardson, "Reconfigurable all-optical packet switching based on fiber Bragg gratings," *OFC 2006* Anaheim, 5-10 Mar 2006, OFJ4.

[155] C. Tian, Z. Zhang, M. Ibsen, M. R. Mokhtar, P. Petropoulos, and D. J. Richardson, "A reconfigurable optical header recognition system for optical packet routing applications," *IEEE Photonics Technology Letters*, vol.18, pp.2395-2397, 2006.

[156] C. Tian, Z. Zhang, M. Ibsen, M. R. Mokhtar, P. Petropoulos, and D. J. Richardson, "Demonstration of a 16-channel code-reconfigurable OCDMA/DWDM system," *OFC 2007*, Anaheim, 25-29 Mar 2007, OMO2.

[157] P. C. Teh, M. Ibsen, L. B. Fu, J. H. Lee, Z. Yusoff, and D. J. Richardson, "A 16-channel OCDMA system based on 16-chip, 20 Gchip/s superstructure fibre Bragg gratings and DFB fibre laser transmitters," *OFC 2002* Anaheim 17-22 Mar 2002 ThEE1.

[158] J. Lauzon, S. Thibault, J. Martin, and F. Ouellette, "Implementation and characterization of fiber Bragg gratings linearly chirped by a temperature gradient," *Optics Letters*, vol. 19, pp. 2027-2029, 1994.

[159] T. Imai, T. Komukai, and M. Nakazawa, "Dispersion tuning of a linearly chirped fibre Bragg grating without a center wavelength shift by applying a strain gradient," *IEEE Photonics Technology Letters*, vol. 10, pp. 845-847, 1998.

[160] M. Born and E. Wolf, *Principles of Optics*, New York: Pergamon, 1987.

[161] J. M. Senior, *Optical Fibre Communications: Principles and Practice*, Cambridge, UK: Cambridge University Press, 1992.

[162] G. P. Agrawal, *Nonlinear Fibre Optics*. New York: Academic Press, 2001.

[163] S. N. Knudsen, "Design and manufacture of dispersion compensating fibres and their performance in systems," *OFC 2002* Anaheim 17-22 Mar 2002 WU3.

[164] L. E. Nelson, "Challenges of 40 Gb/s WDM transmission," *OFC 2001* Anaheim, CA, Mar. 17-22, 2001 ThF1.

[165] C. D. Poole, J. M. Wiesenfeld, D. J. DiGiovanni, and A. M. Vengsarkar, "Optical fibre-based dispersion compensation using higher order modes near cutoff," *Journal of Lightwave Technology*, vol. 12, pp. 1746-1758, 1994.

[166] S. Ramachandran, S. Ghalmi, S. Chandrasekhar, I. Ryazansky, M. F. Yan, F. V. Dimarcello, W. A. Reed, and P. Wisk, "Tunable dispersion compensators utilizing higher order mode fibres," *IEEE Photonics Technology Letters*, vol. 15, pp. 727-729, 2003.

[167] M. Shirasaki, "Chromatic-dispersion compensator using virtually imaged phased array," *IEEE Photonics Technology Letters*, vol. 9, pp. 1598-1600, 1997.

[168] H. Ooi, K. Nakamura, Y. Akiyama, T. Takahara, J. Kumasako, J. C. Rasmussen, T. Terahara, Y. Kawahata, H. Isono, G. Ishikawa, an N. Yamaguchi, "3.5-Tbit/s (43-Gbit/sX88ch) transmission over 600km NZDSF with VIPA variable dispersion compensation," *OFC 2002* Anaheim 17-22 Mar 2002 ThX3.

[169] K. Jinguji and M. Kawachi, "Synthesis of coherent 2-port lattice-form optical delay-line circuit," *Journal of Lightwave Technology*, vol. 13, pp. 73-82, 1995.

[170] K. Takiguchi, S. Kawanishi, H. Takara, A. Himeno, and K. Hattori, "Dispersion slope equalizer for dispersion shifted fibre using a lattice-form programmable optical filter on a planar lightwave circuit," *Journal of Lightwave Technology*, vol. 16, pp. 1647-1656, 1998

[171] C. R. Doerr, S. Chandrasekhar, P. J. Winzer, A. R. Chraplyvy, A. H. Gnauck, L. W. Stulz, R. Pafchek, and E. Burrows, "Simple multichannel optical equalizer mitigatina intersymbol interference for 40-Gb/s nonreturn-to-zero signals," *Journal of Lightwave Technology*, vol. 22, pp. 249-256, 2004.

[172] G.Lenz and C. K. Madsen, "General optical all-pass filter structures for dispersion control in WDM systems," *Journal of Lightwave Technology*, vol.17, pp.1248-1254, 1999.

[173] C. K. Madsen, G. Lenz, A.J. Bruce, M.A. Cappuzzo, L. T. Gomez and R. E. Scotti, "Integrated all-pass filters for tunable dispersion and dispersion slope compensation," *IEEE Photonics Technology Letters*, vol. 11, pp. 1623-1625, 1999.

[174] H. Takahashi, R. Inohara, T. Hisamitsu, M. Hattori, K. Nishimura, and m. Usami, "Expansion of passband of tunable chromatic dispersion compensator based on ring resonators using negative group delay peak," *OFC 2004* Anaheim 6-11 Mar 2004 WK2.

[175] D. J. Moss, L. M. Lunardi, M. Lamont, G. Randall, P. Colbourne, S. Chandrasekhar, L. Buhl and C. A. Hulse, "Tunable dispersion compensation at 10Gb/s and 40Gb/s using all-pass multicavity etalons," *OFC 2003* Atlanta, 23-28 Mar, 2003 TuD1.

[176] D. Yang, C. Lin, W. Chen, and G. Barbarossa, "Fibre dispersion and dispersion slope compensation in a 40- channel 10-Gb/s 3200-km transmission experiment using cascaded

single-cavity Gires-Tournois etalons," *IEEE Photonics Technology Letters*, vol. 16, pp. 299-301, 2004.

[177] T. Komukai, T. Inui, and M. Nakazawa, "The design of dispersion equalizers using chirped fibre Bragg gratings," *IEEE Journal of Quantum Electronics*, vol. 36, pp. 409-417, 2000.

[178] B. J. Eggleton, A. Ahuja, P. S. Westbrook, J. A. Rogers, P. Kuo, T. N. Nielsen, and B. Mikkelsen, "Integrated tunable fibre gratings for dispersion management in high-bit rate systems," *Journal of Lightwave Technology*, vol. 18, pp. 1418-1432, 2000.

[179] A. Walter, and G. Schaefer, "Chromatic dispersion variations in ultra-long-haul transmission systems arising from seasonal soll temperature variations," *OFC 2002* Anaheim 17-22 Mar 2002 WU4.

[180] A. E. Willner, K. M. Feng, J. Cai, S.Lee, J. Peng, and H. Sun, "Tunable compensation of channel degrading effects using nonlinearly chirped passive fibre Bragg gratings," *IEEE Journal of Selected Topics in Quantum Electronics*, vol. 5, pp. 1298-1311, 1999.

[181] M. M. Ohn, A. T. Alavie, R. Maaskant, and M. G. Xu, "Dispersion variable fibre Bragg grating using a piezoelectric stack," *Electronics Letters*, vol. 32, pp. 2000-2001, 1996.

[182] Y. W. Song, D. Starodubov, Z. Pan, Y. Xie, A. E. Willner, and J. Feinberg, "Tunable WDM dispersion compensation with fixed bandwidth and fixed passband center wavelength using a uniform FBG," *IEEE Photonics Technology Letters*, vol. 14, pp. 1193-1195, 2002.

[183] J. A. Rogers, B. J. Eggleton, R. J. Jackman, G. R. Kowach, and T. A. Strasser, "Dual on-fibre thin-film heaters for fibre gratings with independently adjustable chirp and wavelength," *Optics Letters*, vol. 24, pp. 1328-1330, 1999.

[184] Y. W. Song, D. Starodubov, Z. Pan, Y. Xie, A. E. Willner, and J. Feinberg, "Tunable WDM dispersion compensation with fixed bandwidth and fixed passband center wavelength using a uniform FBG," *IEEE Photonics Technology Letters*, vol. 14, pp. 1193-1195, 2002.

[185] N. Q. Ngo, S. Y. Li, R. T. Zheng, S. C. Tjin, and P. Shum, "Electrically tunable dispersion compensator with fixed center wavelength using fibre Bragg grating," *Journal of Lightwave Technology*, vol. 21, pp. 1568-1575, 2003.

[186] Y. W. Song, Z. Pan, S. Nezam, C. Yu, Y. Wang, D. Starodubov, V. Grubsky, J. E. Rothenberg, J. Popelek, H. Li, Y. Li, R. Caldwell, R. Wilcox, and A. E. Willner, "Tunable dispersion slope compensation for 40-Gb/s WDM systems using broadband nonchannelized third-order chirped fibre Bragg gratings," *Journal of Lightwave Technology*, vol. 20, pp. 2259-2266, 2002.

[187] Y. W. Song, S. Nezam, D. Starodubov, J. E. Rothenberg, Z. Pan, H. Li, R. Wilcox, J. Popelek, R. Caldwell, V. Grubsky, and A. E. Willner, "Tunable interchannel broad-band

dispersion-slope for compensation for 10-Gb/s WDM systems using a nonchannelized third-order chirped FBG," *IEEE Photonics Technology Letters*, vol. 15, pp. 144-146, 2003.

[188] C. S. Goh, S. Y. Set, K. Taira, S. K. Khijwania, and K. Kikuchi, "Nonlinearly strain-chirped fibre Bragg grating with an adjustable dispersion slope," *IEEE Photonics Technology Letters*, vol. 14, pp. 663-665, 2002.

[189] C. S. Goh, S. Y. Set, and K. Kikuchi, "Design and fabrication of a tunable dispersion-slope compensating module based on strain-chirped fibre Bragg gratings," *IEEE Photonics Technology Letters*, vol. 16, pp. 524-526, 2004.

[190] S. Matsumoto, T. Ohira, M. Takabayashi, K. Yoshiara, T. Sugihara, T. Hashimoto, K. Matsuoka, T. Miyazaki and F. Kubota, "Tunable dispersion slope compensator with a chirped fibre grating for 160-Gb/s RZ transmission," *OFC 2003* Atlanta, 23 – 28 Mar, 2003 TuD4.

[191] S. Matsumoto, M. Takabayashi, K. Yoshiara, T. Sugihara, T. Miyazaki, and F. Kubota, "Tunable dispersion slope compensator with a chirped fibre grating and a divided thin-film heater for 160-Gb/s RZ transmissions," *IEEE Photonics Technology Letters*, vol. 16, pp. 1095-1097, 2004.

[192] S. Wakabayashi, A. Baba, H. Moriya, X. Wang, T. Hasegawa and A. Suzuki, "Tunable dispersion slope compensator based on chirped FBGs with temperature distributed for 160Gbit/s ," *OFC 2003* Atlanta, 23 – 28 Mar, 2003 MF27.

[193] P. I. Reyes, N. Litchinitser, M. Sumetsky, P.S. Westbrook, "160-Gb/s tunable dispersion slope compensator using a chirped fibre grating and a quadratic heater," *IEEE Photonics Technology Letters*, vol. 17, pp. 831-833, 2005.

[194] P. P. Benham, R. J. Crawford and C. G. Armstrong, *Mechanics of Engineering materials*, 2nd, Singapore: Prentice Hall,1996.

[195] A. Mugnier, E. Goyat, P. Lesueur and D. Pureur, "Wide tuning range and low insertion loss variation dispersion compensator," *Electronics Letters*, vol. 40, pp. 1506-1508, 2004.

[196] R. Ludwig, U. Feiste, C. Schmidt, C. Schubert, J, Berger, E. Hilliger, M. Kroh, T. Yamamoto, C. M. Weinert, and H. G. Weber, "Enabling transmission at 160 Gbit/s," *OFC 2002* Anaheim 17-22 Mar 2002 TuA1.

[197] T. Inui, T. Komukai, M. Nakazawa, K. Suzuki, K. R. Tamura, K. Uchiyama and T. Morioka, " Adaptive dispersion slope equalizer using a nonlinearly chirped fibre Bragg grating pair with a novel dispersion detection technique," *IEEE Photonics Technology Letters*, vol. 14, pp. 549-551, 2002.

[198] T. Inui, T. Komukai and M. Nakazawa, "A wavelength-tunable dispersion equalizer using a nonlinearly chirped fibre Bragg grating pair mounted on multilayer piezoelectric transducers," *IEEE Photonics Technology Letters*, vol. 12, pp. 1668-1670, 2000.

[199] U. Keller, K. J. Weingarten, F. X. Kartner, D. Kopf, B. Braun, I. D. Jung, R. Fluck, C. Honninger, N. Matuschek, and J. A. derAu, "Semiconductor saturable absorber mirrors (SESAM's) for femtosecond to nanosecond pulse generation in solid-state lasers," *IEEE Journal Of Selected Topics In Quantum Electronics*, vol. 2, pp. 435-453, 1996.

[200] M. Hofer, M. H. Ober, R. Hofer, M. E. Fermann, G. Sucha, D. Harter, K. Sugden, I. Bennion, C. A. C. Mendonca, and T. H. Chiu, "High-power neodymium soliton fiber laser that uses a chirped fiber grating," *Optics Letters*, vol. 20, pp. 1701-1703, 1995.

[201] M. E. Fermann, K. Sugden, and I. Bennion, "Generation of 10nj picosecond pulses from a modelocked fiber laser," *Electronics Letters*, vol. 31, pp. 194-195, 1995.

[202] M. H. Ober, M. Hofer, U. Keller, and T. H. Chiu, "Self-starting diode-pumped femtosecond Nd fiber laser," *Optics Letters*, vol. 18, pp. 1532-1534, 1993.

[203] M. E. Fermann, A. Galvanauskas, G. Sucha and D. Harter, "Fiber-lasers for ultrafast optics," *Applied Physics B-Lasers and Optics*, vol. 65, pp. 259-275, 1997.

[204] L. E. Nelson, D. J. Jones, K. Tamura, H. A. Haus, and E. P. Ippen, "Ultrashort-pulse fiber ring lasers," *Applied Physics B-Lasers and Optics*, vol. 65, pp. 277-294, 1997.

[205] S. Matsumoto, T. Ohira, M. Takabayashi, K. Yoshiara, and T. Sugihara, "Tunable dispersion equalizer with a divided thin-film heater for 40-Gb/s RZ transmitter," *IEEE Photonics Technology Letters*, vol. 13, pp. 827-829, 2001.

[206] C. Wu, and M. G. Raymer, "Efficient picosecond pulse shaping by programmable Bragg gratings," *IEEE Journal of Quantum Electronics*, vol. 42, pp. 873-883, 2006.

[207] M. Ibsen, M. K. Durkin, M. N. Zervas, A. B. Grudinin, and R. I. Laming, " Custom design of long chirped Bragg gratings: application to gain-flattening filter with incorporated dispersion compensation," *IEEE Photonics Technology Letters*, vol. 12, pp. 498-500, 2000.